Max-Planck-Institut für Festkörperforschung
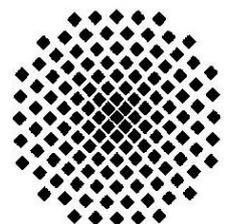
Stuttgart

Ab initio study of point defects in the bulk and on surfaces of an SrTiO$_3$ crystal

Vitaly Alexandrov

Ab initio study of point defects in the bulk and on surfaces of an SrTiO$_3$ crystal

Von der Fakultät Chemie der Universität Stuttgart
zur Erlangung der Würde eines
Doktors der Naturwissenschaften (Dr. rer. nat.)
genehmigte Abhandlung

Vorgelegt von

Vitaly Alexandrov

aus Inta, Russland

Hauptberichter: **Prof. Dr. Joachim Maier**

Mitberichter: **Prof. Dr. Hermann Stoll**

Prüfungsvorsitzender: **Prof. Dr. Thomas Schleid**

Tag der mündlichen Prüfung: 22.06.2009

Max-Planck-Institut für Festkörperforschung, Stuttgart
Universität Stuttgart
2009

What can be completely controlled is never completely real;

what is real can never be completely controlled.

Vladimir Nabokov, "Look at the Harlequins"

Acknowledgements

First and foremost, it is my great pleasure to acknowledge my supervisors – Prof. Dr. Joachim Maier, the director of the Max-Planck Institute for Solid State Research, and Prof. Robert Evarestov, the head of Quantum Chemistry Department at the Saint-Petersburg State University – who patiently guided me throughout my PhD work. Their sage advice, support and constant encouragement have been invaluable contributions to my work both from experimental and theoretical chemistry standpoints which allowed me to gain much insight into the compelling area of computational chemistry of advanced materials.

I am very indebted to Prof. Eugene Kotomin who has always been open to expert and generous discussion giving many profound guidelines. My particular acknowledgement is due to Dr. Rortraut Merkle for readiness to share her comprehensive experimental vision and to link experiment and theory. Special thanks to Uwe Traub and Armin Schuhmacher for efficiently organized computer environment and Sofia Weiglein for the help in administrative issues.

I am also thankful to Dr. Eugene Heifets, Prof. Lev Kantorovich, Prof. Yuri Zhukovskii, Dr. Sergey Piskunov for many fruitful discussions. I am very grateful to my friends Dr. Denis Gryaznov, Dr. Yuri Mastrikov and Linas Vilčiauskas for continual scientific communication and beyond.

Many thanks to all my colleagues at the Maier's department for providing a good rapport, nice atmosphere and having fun out of work.

My deepest gratitude goes above all to my wife Lena for her understanding, support and inexhaustible love.

Contents

Chapter 1

Introduction and objectives

ABO$_3$-type perovskites represent a broad family of transition metal ternary oxides; about 90% of metallic elements in the Periodic Table may form stable perovskite-structured crystals. The diversity of chemical compositions can be broadened due to the aptitude to tolerate different kinds of point defects, e.g., forming multicomponent solid solutions by partial substitution of cations in positions A and B or by creating cation and oxygen vacancies. Of course, a great deal of practically appealing properties hinge on the presence of point defects. Consequently, the comprehensive knowledge of the role that defects play is vital to unravel many phenomena and to tailor desirable material properties.

The cubic SrTiO$_3$ crystal (P$m\bar{3}m$ space group, see Figure 1.1) deserves attention as an archetypical model ABO$_3$ perovskite that has been a focal point for numerous investigations over many years. It has a simple structure, high thermal stability (T$_{melt}$ = 2100°C) and an excellent chemical resistance to many solvents. Owing to the ability to readily form high quality interfaces with other crystals, it is often used as a substrate material for epitaxial growth of high-T$_c$ superconductors (1; 2) and other oxide-based multilayered systems (3; 4). A very large dielectric permittivity ($\epsilon \approx 300$ at room temperature) is of importance for use in high-voltage capacitors and dynamic random access memory (DRAM)
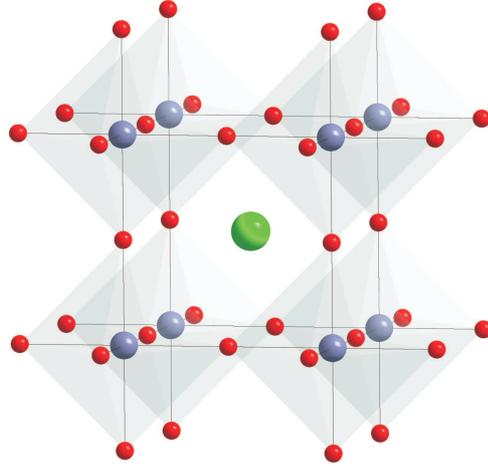
Figure 1.1: $SrTiO_3$ cubic structure: $Pm\bar{3}m$ space group with a $= 3.90$ Å, Wyckoff positions: Sr - $1a$ (0,0,0); Ti - $1b$ (0.5,0.5,0.5); O - $3c$ (0.5, 0.5, 0). Oxygen polyhedra around titanium ions are also shown.

devices ([5]; [6]). Some applications are related to ferroelectric surface properties, although bulk $SrTiO_3$ itself does not boast ferroelectricity below and above the temperature of transition to tetragonal phase ($\sim$104 K). Especially when doped, $SrTiO_3$ is widely used in photocatalysis, e.g., it can decompose water without external bias ([7]). $SrTiO_3$ may even serve as a gemstone being a diamond simulant because of their high and similar refractive indexes ($\sim$2.4) ([8]).

A core set of properties of perfect $SrTiO_3$ crystal appears to be well elucidated both experimentally and theoretically. Regarding the first-principles modeling, great progress has been recently made in understanding a wide range of bulk electron and phonon properties ([9]; [10]; [11]), the structure of perfect surfaces, their reactivity, chemical bonding, adsorption behavior, etc. ([12]; [13]). Importantly, there is an agreement between experiments and theory that the (001) surface is the most energetically favorable, both the SrO and the TiO_2-terminated surfaces showing similar thermodynamic stability ([14]). It is known that the highly ionic

SrO surface has a basic nature – it readily reacts with H_2O and CO_2 (15). The TiO_2-terminated surface reveals a marked energy gap reduction and a considerable degree of the Ti–O bond covalency, even larger than in the bulk (12).

Unlike perfect $SrTiO_3$, bulk and especially *surface properties* in the presence of defects are far less understood because even for the (001) surface a variety of reconstructions, morphologies and chemical compositions may exist, while most of *ab initio* simulations were restricted to stoichiometric models for a simplest 1×1 termination. However, some experiments suggest that it is the change in stoichiometry that drives the surface to evolve into different structural configurations (16). Some surface reconstruction models were based upon oxygen vacancies (17) while others point to a supplementary role of surface Sr adatoms (18). The presence of defects certainly modifies not only atomic but also electronic properties of surfaces, e.g., the formation of surface oxygen vacancies leads to a conducting state of TiO_2 facet in $SrTiO_3$ crystal (19).

The oxygen vacancy V_O (also called the F center) is likely the most abundant defect in transition metal oxides and accounts for a rich variety of phenomena. To shed light on this pivotal defect, it is instructive to view it from different angles.

Firstly, V_O may be considered from the electronic point of view as an electron or a hole trap/donor. In this respect, the position (shallow or deep) of vacancy's one-electron energy levels with respect to the conduction band is crucial for the electronic behavior and the optical properties of an oxygen nonstoichiometric material. The oxygen vacancies are believed to be largely responsible for leakage current (20), electrical breakdown (21) or degradation of transition metal oxide-based microelectronic devices (22; 23). Also, the V_O are often implicated in deteriorating the performance of high-k gate oxides such as ZrO_2, HfO_2, trapping electrons and thereby reducing carrier mobility (23; 24). Thus, the understanding of the V_O electronic properties and energetics of its formation in different charge

states is of great practical importance.

As to the $SrTiO_3$ crystal in particular, oxygen vacancies are known to be a source of electron doping, thus making it n-type conductor. The change of oxygen concentration by only 10 ppm can change the conductivity of $SrTiO_3$ from a good n-type to a poor p-type. Furthermore, $SrTiO_3$ may even become superconducting in strongly oxygen-reduced atmosphere at T $\leq$ 0.35 K. An appropriate tuning of the oxygen content also enables to switch the conductivity from the electronic to ionic type (see (25) and references therein).

First-principles simulations of V_O in $SrTiO_3$ bulk were performed in both the DFT plane wave and LCAO approaches (26; 27; 28), however, the detailed understanding of oxygen-deficient material properties is still scarce. Among important questions about the electronic properties is the position of the V_O energy levels in the optical bandgap for different defect charge states, which is particularly unclear for *defective surfaces*. Nevertheless, some experimental studies suggested a more shallow defect level on the surface than in bulk.

Secondly, at elevated temperatures the V_O is a crucial ionic mobile carrier whose transport properties are of substantial practical relevance to solid oxide fuel cells, permeation membranes, oxygen gas sensors, etc. (29; 30; 31; 32). For instance, the *migration of oxygen vacancies* in perovskite ferroelectric materials and pinning of the domain walls has shown to affect the switching process and stimulate polarization fatigue (22). The dynamics of oxygen species is of primary concern in investigating transport properties and the overall kinetics of oxygen transport, thus playing decisive role in performance of the aforementioned (electro)chemical systems (25). The comprehensive study of solid state kinetics in oxygen-deficient material at ambient conditions should comprise the exploration of a number of individual transport processes. This includes *adsorption of oxygen species* and possible chemical transformations at the surface (e.g., molecular to atomic oxygen), the subsequent diffusion of oxygen through the top surface

layer into the bulk due to the presence of oxygen vacancies and diffusion within the surface layer, bulk diffusion and, in polycrystalline materials, charge/mass transfer across the grain boundaries.

Recent experimental efforts shed much light on the kinetics of stoichiometry change on the example of $SrTiO_3$ electroceramic (25), however, *ab initio* calculations are expected to complement the experiments in the exploration of kinetic mechanisms. Recently, activation barriers for the V_O self-diffusion in bulk and along the TiO_2 surface of $SrTiO_3$ have been evaluated using the DFT plane wave modeling, expectedly showing several times lower energy barrier for the surface diffusion (33). However, the questions of the vacancy diffusion from the topmost surface (SrO or TiO_2) to the second layer (subsurface diffusion), as well as diffusion of adsorbed oxygen species along the surface have not yet been addressed. Furthermore, oxygen vacancies are significant not only for the ionic transport but also for the electronic properties, being ultimately coupled with electronic charge concentration (25).

Another way of modifying native perovskite properties is to incorporate dopants in substitutional positions in the lattice. Thus, **Fe-doped SrTiO$_3$ crystal** is of special interest since iron substituting Ti^{4+} primarily exhibits the oxidation states of 3+ and 4+ and hence act as a redox center. Clearly, there is a noticeable difference between these two states as Fe^{3+} has a stable half-filled *d*-shell and also requires a positive charge compensation. As a result, Fe-doped $SrTiO_3$ crystal (with a fraction of Fe^{3+} substituting Ti^{4+}) may serve as an example of acceptor doping because of producing excess positive charge carriers relative to the perfect lattice (predominantly doubly-charge oxygen vacancies $V_O^{\cdot\cdot}$ and a small amount of holes in the valence band) (25).

In principle, two cases could be distinguished depending on the iron content. The first case is a dilute solid solution in which Fe ions do not interact ("*electron-poor*" materials). On this basis, the ideal mass-action law has been

applied showing that the Fe^{3+}/Fe^{4+} ratio increases with lowering oxygen partial pressure and increasing temperature (25). Recent study by means of EXAFS and vibrational spectroscopy (34) has proven the existence of the Jahn-Teller distortion around a single Fe^{4+} impurity in fully oxidized material, as previously was predicted in the Hartree-Fock calculations (35).

However, already 3% iron doping marks the transition to the nondilute regime when iron ions form a broadened defect band (observed in XPS spectra) indicative of "*electron-rich*" materials. Therefore, oxygen nonstoichiometric samples, sufficiently doped by iron to exhibit both ionic and electronic conductivities, are an important example of an advanced electroceramic mixed conductor (25).

$SrFe_xTi_{1-x}O_{3-\delta}$ solid solution has recently been subject of many experimental investigations with a particular emphasis on atomic and electronic structure (34; 36), defect chemistry (37; 38) and transport properties (25; 39; 40). Quite many advances have been made in identifying defect species and quantifying their presence under ambient conditions (37; 41; 42). Using in situ electron paramagnetic resonance (EPR) spectroscopy (37), it has been shown that Fe^{3+}-$V_O^{\cdot}$ defect pairs are readily formed even at iron concentration below 0.1 at.% and are most relevant at low temperatures while being completely dissociated above 300°C. The presence of higher-order complexes such as Fe^{3+}-$V_O^{\cdot\cdot}$-Fe^{3+} has not been determined in this study. The experimental study (43) has proved the leakage current caused by V_O to be diminished in Fe-doped $SrTiO_3$, also hinting at the presence of bound iron-vacancy species. The estimate of *binding energies* for different types of such associates can provide important information on their relevance and on the temperature range of their stability.

The truly enormous interest in *nanoscale materials* has emerged over the past two decades due to discovery of numerous novel phenomena in which dimensionality highlights appealing size-tunable properties promising for manifold applications of technological relevance. The striking examples of semiconducting

nanotubes, quantum dots or nanomagnets, among many others, have made the field of low-dimensional systems rapidly growing and attracted vast scientific attention. In the context of mixed electronic-ionic conductors, such as $SrTiO_{3-\delta}$, the interest in size-dependent properties arise. A large density of interfaces, such as grain boundaries in nanoceramics or surfaces in thin films, leads to such a close spacing that the interface boundary zones (*space charge layers*) begin to overlap and specific bulk transport properties die off (6; 44; 45). Here we enter into the exciting area of nanoionics.

The term **Nanoionics** has been first introduced in 1992 (46) [1] in order to highlight the paramount importance of ionic properties at nanometer length scales and immense potential of the field for future technology (44; 45). Conceptually analogous to nanoelectronics, it deals with systems where ionic transport plays a major role, although the properties become different from the bulk properties as nanosize effects start to hold sway. Some recent works have paved the way towards devices which elegantly combine transport properties of both electrons and oxygen vacancies at nanoscale. For instance, a sandwich-like material consisting of $TiO_{2-\delta}$ layer placed between two metallic electrodes has shown to work as a 'memristive' (memory resistor) switch (49). This is because the barrier width at the metal/oxide interface can be tuned by applying an electric field to move the positively charged V_O in the oxide layer away from or closer to the interface, thereby changing the electron transport properties through the interface.

One of the key issues for applications of nanoceramics (including Fe-doped $SrTiO_3$) is the altered ionic conductivity at *grain boundaries* (25). The grain boundary core serves as a sink and source for mobile charge carriers and impurities, and therefore is usually charged with respect to the bulk of the grains. As a consequence, the carriers with the same/opposite charge should deplete/accumulate

---

[1]The paper "A step towards nanoionics" by Despotuli A. and Nikolaichik V. was destined as a timely recognition of the new field but definitely was not the first study of nanoionic effects; some earlier works are noteworthy (47; 48)
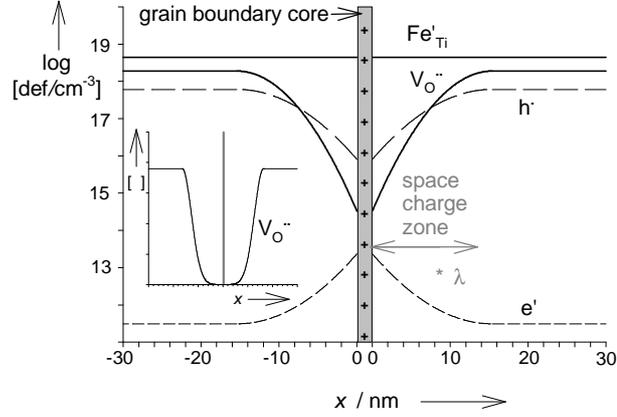
Figure 1.2: Charge-carrier concentration profiles at a blocking grain boundary in Fe-doped SrTiO$_3$ ([Fe]$_{total}$=0.1 mol%, T=700 °C, pO$_2$=1 bar, $\Delta\phi$=0.4 V). Note the logarithmic concentration scaling in the main plot and linear scaling in the inset.

nearby the grain boundary core constituting space charge zones (see Figure 1.2). Change in the carrier concentration greatly affects the conductivity. In principle, two scenarios can be recognized: accelerated and impeded ion transport through the grain boundaries compared with the bulk conductivity. It is observed that many acceptor-doped wide-gap oxides exhibit impeded transport or even blocking effects at the interface that facilitates their use as varistors (50) but hinders fast ion transport applications (51). Hence, the origin of the excess charge at the grain boundary core is the nub of the conductivity problem. This raised the problem of the V$_O$ *segregation effect* toward the SrTiO$_3$ surfaces.

Following the work on heterostructures of fluorite conductors (52) many efforts have been undertaken to increase the ion conductivity in oxidic systems, owing to the comparatively low mobility of the oxygen vacancy without great success. Only recently huge conductivity in ZrO$_2$:Y$_2$O$_3$/SrTiO$_3$ heterostructures (53) has been reported, the validity of which, however, has to be confirmed.

One of the special concerns of nanoionics should be also the properties of individual ions or defects under confined conditions unlike the collective ionic behavior. This can be particularly interesting and practically important for such common species as oxygen vacancies in different chemical compounds (covalent or ionic) with rather delocalized wavefunctions. This problem has not been tackled so far. It can include both static and dynamic ion properties such as the electron density distribution at the vacancy site, the position of energy level in the bandgap, the formation energies and diffusion, etc.

Overall, the area of nanoionics has vigorously developed over the last few decades since many emerging properties are of a great promise for fuel cells, batteries, storage and switching devices, chemical sensors and filters, electrochromic windows, etc. Most of these issues have been attacked by experimental means, but theoretical investigations may greatly assist in elucidating important aspects.

First principles quantum chemical methods have recently become highly efficient tools to portray physico-chemical phenomena at the atomic scale ([54]; [55]) being both a vital adjunct to experiments and an important source of prediction. In this study, we aim to apply such first-principles calculations based upon the density functional theory (DFT) methodology, in order to gain more insight into the properties of *point defects in bulk and on surfaces of SrTiO₃ crystal*.

After the preceding brief overview of some challenges associated with the defective $SrTiO_3$ material, we may now delineate **our key matters of interest in the present study**. We hasten to point out from the outset that we pursue rather modest objectives leaving aside many important issues. Thus, we do not consider any extended defects such as dislocations although these are known to play significant role in $SrTiO_3$. Even focusing on point defects, we confine ourselves to the analysis of atomic and electronic structure, basic magnetic properties and some energetic quantities (defect formation energies, cluster binding energies, diffusion activation barriers). The point defects of our interest are the

oxygen vacancies in neutral and single-charged states (F and F^+ centers), iron impurities substituting Ti^{4+} ion and defect complexes combining these two point defects. Point defects as interstitials or Frenkel pairs are also not touched here.

Prior to examining defects in $SrTiO_3$ crystal, we first study perfect $SrTiO_3$ and $SrFeO_3$ parent compounds which are the limiting cases of the $SrTi_xFe_{1-x}O_3$ solid solution (Chapter 3). Using several computational schemes, we wish to explore a number of properties and demonstrate the relevance of the hybrid HF-DFT LCAO framework chosen as a tool for the principal investigation. Also, we study both orthorhombic and monoclinic phases of $CaFeO_3$ crystal which have remarkably different properties from $SrTiO_3$ and $SrFeO_3$ being induced by just a small lattice distortion (reproduced theoretically).

As a next step, we focus in Chapter 4 on the modeling of Fe-doped $SrTiO_3$ bulk crystal considering several iron concentrations in the $SrTi_xFe_{1-x}O_3$ solid solution series. Emphasis will be laid on the energetics of iron incorporation, the induced *Jahn-Teller lattice distortion* and the electronic properties pertaining to the transition from the wide-gap semiconducting $SrTiO_3$ to the metallic $SrFeO_3$ crystal.

The electronic properties of oxygen vacancies in the $SrTiO_3$ bulk will be addressed by removing oxygen atoms but retaining the "ghost" wave functions at the vacancy site. At this stage, we are seeking to treat the neutral and single-charged oxygen vacancies with two and one electrons at the vacancy position (F and F^+ centers), respectively. We estimate *the position of one-electron energy levels* within the band gap and *the formation energies* for both types of defects. Activation barriers for the oxygen vacancy *self-diffusion* are also evaluated through a minimum energy path method.

Then, we concentrate on the Fe-doped $SrTiO_3$ crystal with oxygen vacancies present and able to form *defect complexes*, the binding energies of which we will estimate. The changes in the electronic structure properties as compared with

the single defects are also taken up.

From the study of bulk defects we then turn in Chapter 5 to defective $SrTiO_3$ (001) surfaces. Based upon the defect formation energies, we consider *the defect segregation energies* from the bulk to the surface for all defects under consideration. This should help discern which defects are expected to be accumulated on the surface (grain boundary) and what the nature of the space charge layer in $SrFe_xTi_{1-x}O_{3-\delta}$ material could be. We look into the structural, electronic and chemical properties of the defective surfaces compared with the native surfaces. We analyze atomic *oxygen adsorption energies* for different possible adsorption sites on the surfaces in order to shed more light on the overall oxygen kinetics of $SrTiO_3$ crystal including the prediction of the rate-determining step in oxygen reduction. We also estimate activation barriers for different *oxygen vacancy diffusion* channels (in-plane at the surface, a drop of the adsorbed oxygen atom into the vacancy nearby).

Finally, Chapter 6 deals with *the confinement effects* on the oxygen vacancies in order to comprehend how basic atomic and electronic properties are modified when a vacancy is confined in a specific dimension, for example, being placed in an ultra-thin film. This issue is of interest owing to the important role that oxygen vacancies play in materials with ionic conductivity in the nano-scale regime. It is worth noting that confinement effects on excitations such as electrons, excitons, phonons, magnons are being widely investigated and these effects give rise to some remarkable changes in host material properties. In the present study, we are mainly concerned with *the electronic properties* and the formation energy changes for the representative ionic defects, namely, neutral and charged oxygen vacancies.

Chapter 2

Theoretical and computational background

This section recapitulates the key points of quantum chemical methods and simulation models applied in the study. The focus is placed on the hybrid HF-DFT approach within the LCAO approximation as a primary tool in our computational framework, while a plain DFT formalism combined with the plane wave expansion is briefly outlined. The periodic supercell approach used for the modeling of defects in 3D and 2D cases and the Jahn-Teller effect theory are shortly described.

2.1 Hartree-Fock-Roothaan method and the CRYSTAL-2006 code

2.1.1 Main framework

Within the one-determinant approximation an N-electron wavefunction $\Psi(1, 2, ..., N)$ is represented as an antisymmetrized product of spin-orbitals $\psi(i)$ (Slater determinant):

$$\Psi(1, 2, ..., N) = \frac{1}{\sqrt{N!}} \sum_P (-1)^P \psi_1(1) \psi_2(2)...\psi_N(N) \tag{2.1}$$

where P is a permutation number (even or odd). The best spin-orbitals to use are eigenfunctions of an one-electron eigenvalue equation

$$\hat{F}\psi = \varepsilon\psi \tag{2.2}$$

where the Fock operator $\hat{F}$ is the Hamiltonian for a single electron in an effective field of the remaining electrons and the nuclei (56). In the linear combination of atomic orbitals (LCAO) approximation, proposed independently by Roothaan (57) and Hall (58), spin-orbitals ψ are expanded over atomic-like basis functions χ_a ($a = 1, ..., M$)

$$\psi_k(i) = \sum_{a=1}^{M} c_{ak} \chi_a(i) \tag{2.3}$$

Variation of the orbital coefficients c_{ak} leads to the "best" set of c_{ak} when the corresponding Slater determinant minimizes the averaged ground state energy. Fulfilling the orthonormality condition $\boldsymbol{CSC}^\dagger = \boldsymbol{I}$, the orbitals ψ are determined by equation

$$\langle \delta\psi_i | \hat{F} | \psi_i \rangle - \sum_j \langle \delta\psi_i | \psi_j \rangle \varepsilon_{ji} = 0, \tag{2.4}$$

where ε_{ji} are Lagrangian multipliers and $\delta\psi_i = \sum_a \delta c_{ai} \chi_a$ are independent variations of $\psi(i)$. It leads to a set of equations

$$\langle \chi_a | \hat{F} | \psi_i \rangle - \sum_j \langle \chi_a | \psi_j \rangle \varepsilon_{ji} = 0, \tag{2.5}$$

with $i = 1, ..., N$; $a = 1, ..., M$.

Using matrix notation, we can write that

$$\langle\chi_a|F|\psi_i\rangle = \sum_b\langle\chi_a|F|\chi_b c_{bi}\rangle = \sum_b F_{ab}c_{bi} = (FC)_{ai}, \qquad (2.6)$$

$$\sum_j\langle\delta\psi_i|\psi_j\rangle\varepsilon_{ji} = \sum_{j,b}\langle\chi_a|\chi_b\rangle c_{bj}\varepsilon_{ji} = \sum_j(\sum_b S_{ab}c_{bj})\varepsilon_{ji} = \sum_j(SC)_{aj}\varepsilon_{ji} = (SCE)_{ai}$$
$$(2.7)$$

and thus the matrix form of the Hartree-Fock-Roothaan (HFR) equation reads as

$$\boldsymbol{FC} = \boldsymbol{SCE} \qquad (2.8)$$

Group theory provides the way to exploit symmetry properties of a system through the construction of symmetry-adapted basis sets (e.g., by applying the Wigner operators to the initial set) which transform according to the irreducible representations (irreps) $\boldsymbol{\Gamma}$ of a given symmetry group. One of the consequences of the Wigner-Eckart theorem (59; 60) is that the HFR equations split into several sets of equations with smaller dimensionalities $\boldsymbol{F_\Gamma C_\Gamma} = \boldsymbol{S_\Gamma C_\Gamma E_\Gamma}$, each belonging to different irreps. Such a factorization permits to largely reduce the computational cost.

The exploitation of symmetry in the CRYSTAL-2006 code is rigorous and includes the use of both translational invariance and point symmetry (61; 62). The use of translational symmetry allows us to rewrite the expansion of one-electron eigenfunctions $\psi_k(i)$ (Crystalline Orbitals, COs) as a linear combination of Bloch functions (BFs) $\phi_\mu(\boldsymbol{r};\boldsymbol{k})$:

$$\psi_i(\boldsymbol{r};\boldsymbol{k}) = \sum_\mu^M c_{\mu i}(\boldsymbol{k})\phi_\mu(\boldsymbol{r};\boldsymbol{k}) = \sum_\mu^M c_{\mu i}(\boldsymbol{k})\sum_{\boldsymbol{g}}^L e^{i\boldsymbol{k}\boldsymbol{g}}\chi_\mu(\boldsymbol{r}-\boldsymbol{r}_\mu-\boldsymbol{g}), \qquad (2.9)$$

where the wave vector $\boldsymbol{k}$ in the first Brilluoin zone (BZ) classifies the irreps of the translational group; M is the number of atomic orbitals in a cell and L – the

number of primitive cells in the main region of real space. Note that AOs $\chi_\mu(\boldsymbol{r})$ can be represented by both analytical functions (gaussians, Slater-type orbitals) and numerical orbitals on a grid (54).

At this point, the HFR equation can be solved for each $\boldsymbol{k}$ vector in the BZ in order to find the matrix of expansion coefficients $\boldsymbol{C}(\boldsymbol{k})$ and the diagonal energy matrix $\boldsymbol{E}(\boldsymbol{k})$:

$$\boldsymbol{F}(\boldsymbol{k})\boldsymbol{C}(\boldsymbol{k}) = \boldsymbol{S}(\boldsymbol{k})\boldsymbol{C}(\boldsymbol{k})\boldsymbol{E}(\boldsymbol{k}), \tag{2.10}$$

where $\boldsymbol{S}(\boldsymbol{k})$ is the overlap matrix between the BFs and $\boldsymbol{F}(\boldsymbol{k})$ is the Fock matrix in $\boldsymbol{k}$-space. Representations of these matrices in reciprocal and real space are connected by the Fourier transformation:

$$\boldsymbol{S}(\boldsymbol{k}) = \sum_{\boldsymbol{g}} e^{i\boldsymbol{k}\boldsymbol{g}}\boldsymbol{S}^{\boldsymbol{g}}, \boldsymbol{F}(\boldsymbol{k}) = \sum_{\boldsymbol{g}} e^{i\boldsymbol{k}\boldsymbol{g}}\boldsymbol{F}^{\boldsymbol{g}} \tag{2.11}$$

with elements $S_{\mu\nu}^{\boldsymbol{g}} = \langle\chi_\mu^{\boldsymbol{0}}|\chi_\mu^{\boldsymbol{g}}\rangle$ and $F_{\mu\nu}^{\boldsymbol{g}} = \langle\chi_\mu^{\boldsymbol{0}}|\hat{F}|\chi_\mu^{\boldsymbol{g}}\rangle$. Thus, in the basis of BFs, the Fock matrix consists of diagonal blocks each of which corresponds to an individual $\boldsymbol{k}$ vector.

Furthermore, point symmetry of a crystal can be used to greatly reduce the number of $\boldsymbol{k}$ vectors in which calculations are performed. More precisely, a set of nonequivalent vectors $\{\boldsymbol{k}_1,...,\boldsymbol{k}_m\}$, where $\boldsymbol{k}_j=R_j\boldsymbol{k}$ and R_j are point symmetry operations from the crystal space group, is called m-ray star of a wavevector $\boldsymbol{k}$ (63). Since all vectors from one star are related by symmetry operations, we can reduce our consideration to a representative vector from the set and analyze the so-called irreducible Brillouin zone (IBZ) in which each star is represented by one ray. For instance, in the most favorable case of cubic crystals with 48 symmetry operations the IBZ is 1/48 the total BZ. In turn, to sample the IBZ, we will define a grid of special points to consider a large enough but finite number of $\boldsymbol{k}$ points and use the theorem that energy is a smooth function of $\boldsymbol{k}$ to apply an interpolation scheme (54).

Moreover, the use of point symmetry of each $\boldsymbol{k}$ vector in the IBZ (so-called little co-group of $\boldsymbol{k}$) (63) allows one to make the Fock matrix even more sparse by factorizing each $\boldsymbol{k}$ block into sub-blocks corresponding to different irreps of $\boldsymbol{k}$ little co-group.

In practical calculations, the Hartree-Fock (HF) and Kohn-Sham (DFT) theories differ in the way how the Fockian operator is constructed in order to solve Equation 2.10:

$$F_{HF} = T + Z + J + X \tag{2.12}$$

and

$$F_{KS} = T + Z + J + X_i(\rho) + C_j(\rho), \tag{2.13}$$

which include kinetic energy contribution (T), electron-nuclear attraction (Z), electron-electron Coulomb (J) and HF exchange (X) operators; exchange (X_i) and correlation (C_j) functionals. Within the HF theory, we may write down the elements of the Fock matrix in direct space ($\chi_\mu^{\boldsymbol{0}}$ denotes AO in $\boldsymbol{0}$-cell):

$$F_{\mu\nu}^{\boldsymbol{g}} = T_{\mu\nu}^{\boldsymbol{g}} + Z_{\mu\nu}^{\boldsymbol{g}} + J_{\mu\nu}^{\boldsymbol{g}} + X_{\mu\nu}^{\boldsymbol{g}} \tag{2.14}$$

with one-electron

$$T_{\mu\nu}^{\boldsymbol{g}} + Z_{\mu\nu}^{\boldsymbol{g}} = \langle \chi_\mu^{\boldsymbol{0}} | \hat{T} | \chi_\nu^{\boldsymbol{g}} \rangle + \langle \chi_\mu^{\boldsymbol{0}} | \hat{Z} | \chi_\nu^{\boldsymbol{g}} \rangle \tag{2.15}$$

and two-electron

$$C_{\mu\nu}^{\boldsymbol{g}} + X_{\mu\nu}^{\boldsymbol{g}} = \sum_{\alpha\beta}^{m} \sum_{n}^{\infty} P_{\alpha\beta}^{\boldsymbol{n}} \sum_{h}^{\infty} [(\chi_\mu^{\boldsymbol{0}} \chi_\nu^{\boldsymbol{g}} | \chi_\alpha^{\boldsymbol{h}} \chi_\beta^{\boldsymbol{h+n}}) - \frac{1}{2} (\chi_\mu^{\boldsymbol{0}} \chi_\alpha^{\boldsymbol{h}} | \chi_\nu^{\boldsymbol{g}} \chi_\beta^{\boldsymbol{h+n}})] \tag{2.16}$$

contributions. The elements of the density matrix $\boldsymbol{P^n}$ in direct space are determined as

$$P_{\alpha\beta}^{\boldsymbol{n}} = \frac{2}{\Omega_{BZ}} \int_{BZ} e^{-i\boldsymbol{kn}} \sum_j C_{\alpha j}(\boldsymbol{k}) C_{\beta j}^*(\boldsymbol{k}) \Theta[E_{Fermi} - E_j(\boldsymbol{k})] d\boldsymbol{k} \tag{2.17}$$

It is clear that the calculation procedure must be iterative since knowledge of the matrix $\boldsymbol{C}(\boldsymbol{k})$ is needed for the calculation of the density matrix $\boldsymbol{P^n}$ but should be obtained from the main Equation 2.10.

From the preceding consideration, the main steps of the LCAO-based program like CRYSTAL-2006 may be summarized as follows:

1. Representation of the Fockian in the basis of the AOs and calculation of its $(M^2 \times L)$ elements: $\boldsymbol{F^g_{\mu\nu}}$

2. Representation of $\boldsymbol{F}$ and $\boldsymbol{S}$ matrices in the basis of BFs at every $\boldsymbol{k}$ point of the BZ (a Fourier transform from direct to reciprocal space): $\boldsymbol{F}_{\mu\nu}(\boldsymbol{k}) = \sum_{\boldsymbol{g}}^{L} exp(i\boldsymbol{kg})\boldsymbol{F^g_{\mu\nu}}$

3. The HFR equation 2.10 is solved at every $\boldsymbol{k}$ point to obtain the coefficient $\boldsymbol{C}(\boldsymbol{k})$ and energy $\boldsymbol{E}(\boldsymbol{k})$ matrices.

4. Determination of the Fermi energy E_{Fermi}

5. Calculation of the density matrix $\boldsymbol{P}$ in reciprocal space and its Fourier anti-transform to direct space:

$$P_{\alpha\beta}(\boldsymbol{k}) = 2 \sum_{j(occupied)} C_{\alpha j}(\boldsymbol{k}) C^*_{\beta j}(\boldsymbol{k}); \qquad (2.18)$$

$$P^{\boldsymbol{n}}_{\alpha\beta} = \frac{1}{N} \sum_{\boldsymbol{k}} e^{-i\boldsymbol{kn}} P_{\alpha\beta}(\boldsymbol{k}) \qquad (2.19)$$

2.1.2 Exchange-correlation functionals

The HF and the KS approaches differ mostly in the way of constructing the Fockian and the Kohn-Sham Hamiltonian used in solving independent-particle equations in a self-consistent manner. In the HF method the Fockian does not include correlation, while the DFT-based techniques rest upon approximate exchange-correlation energy functional of the electron density in accordance with the Kohn-Sham *ansatz* (64). The fact that the exact KS exchange-correlation functional is

not known has led to a variety of parameterizations within different approximations. Some important formulations involve local density approximation (LDA), generalized gradient approximation (GGA), orbital-dependent functionals such as LDA+U and optimized effective potentials (OEP), hybrid HF-DFT functionals (that include a part of the Hartree-Fock exchange) (54; 55).

The CRYSTAL-2006 code we used embraces a range of LDA and GGA exchange and correlation functionals, as well as some standard hybrid ones such as B3LYP and B3PW (65). The idea of the latter arises from the fact that pure DFT methods overestimate delocalization of the electron density due to non-exact cancelation of the electron self-interaction and underestimate the band gaps of insulators whereas the pure HF greatly overestimates gaps. The hybrid HF-DFT functionals take into account an explicit orbital dependence of the energy through non-local part of the exchange (66).

The exchange-correlation energy for the widely-used B3LYP functional reads as

$$E_{xc} = aE_x^{HF} + (1-a)(E_x^{LDA} + bE_x^{Becke}) + cE_c^{LYP} + (1-c)E_c^{VWN} \qquad (2.20)$$

thus combining 20% HF, 8% Slater (LDA), 72% Becke exchange, and 19% local functional Vosko-Wilk-Nusair (VWN), 81% gradient corrected functional Lee-Yang-Parr (LYP). In case of the B3PW functional, the correlation part is Perdew-Wang (PW) functional instead of LYP.

The application of hybrid functionals in recent years has been particularly successful in quantum chemistry of molecules and solids for the quantitative description of atomic structure, magnetic properties, vibrational frequencies, electronic properties including optical band gap, and others (66). Such hybrid methodology has been commonly used in conjunction with the LCAO basis set, however, as it was recently demonstrated in (67), it may be also combined with the plane wave basis. When Thesis was close to completion, the new version (VASP 5) with the hybrid methodology implemented was released (68; 69; 70).

2.1.3   Basis set and pseudopotentials

In practical implementations of both the HF and the KS methods, every canonical spin-orbital ψ_i is expanded into a set of basis functions. For periodic systems, a spin-orbital is usually represented as a linear combination of atomic orbitals (the HFR method outlined above) or as a combination of PWs (widely used in the DFT methods, see below).

In the LCAO-based CRYSTAL-2006 package, each AO is expressed as a linear combination of n_G normalized Gaussian-type functions with constant coefficients d_j and exponents α_j:

$$\chi_\mu(\boldsymbol{r} - \boldsymbol{r}_\mu - \boldsymbol{g}) = \sum_j^{n_G} d_j G(\alpha_j; \boldsymbol{r} - \boldsymbol{r}_\mu - \boldsymbol{g}) \qquad (2.21)$$

In turn, $G(\alpha; r)$ is the radial part $R_{nl}(r)$ of the full AO $\chi_{nlm}(\boldsymbol{r}) = R_{nl}(r)S_{lm}(\theta,\varphi)$ (where $S_{lm}(\theta,\varphi)$ is a spherical harmonic function):

$$G(\alpha; r) = R_{nl}(r) = \frac{2^{n+1}\alpha^{(2n+1)/4}}{(2\pi)^{1/4}[(2n-1)!!]^{1/2}} r^{n-1} e^{-\alpha r^2}, \qquad (2.22)$$

with one fitting parameter α. The great virtue of this representation led to its wide use is that a product of two functions centered at $\boldsymbol{R}_A$ and $\boldsymbol{R}_B$ can be always considered as a single Gaussian

$$e^{-\alpha|\boldsymbol{r}-\boldsymbol{R}_A|^2} e^{-\beta|\boldsymbol{r}-\boldsymbol{R}_B|^2} = C_{AB} e^{-(\alpha+\beta)|\boldsymbol{r}-\boldsymbol{R}_C|^2}, \qquad (2.23)$$

which is centered at the intermediate point

$$\boldsymbol{R}_C = \frac{\alpha\boldsymbol{R}_A + \beta\boldsymbol{R}_B}{\alpha + \beta} \qquad (2.24)$$

This results in a simple analytical calculation of all integrals in the Fock matrix.

The α parameters are in general non-transferable as an atom usually has distinct properties in different environments. The crucial point here is that the

parameter α should be well fitted to minimize the total energy of a particular system. In practical calculations of solids, it is quite difficult to achieve a variational minimum due to the possibility of basis-set linear dependence problem leading to "numerical catastrophes" when decreasing exponent. As a result, an adequate compromise between the exponent values and accuracy must be reached.

When the number of electrons on atoms increases, so does the number of basis functions necessary for their description leading to a high concomitant computational cost. However, the core electrons have deep energy levels and their atomic orbitals do not participate significantly in the chemical bonding. Thus, the partition of core electrons represented by one-particle effective potential (pseudopotential) and valence electrons leads to the efficient concept of Effective Core Potentials (ECP). What electrons should be cast as valence must be decided for each concrete system, and large or small core approximations may be regarded.

There exist a number of the ECP parametrizations for the LCAO calculations such as Durand-Barthelat (71), Hay-Wadt (72) and Stuttgart-Dresden (73) pseudopotentials (PPs). Hay-Wadt PPs are constructed in both large and small core approximations, and the latter is necessary for a proper description of compounds with d- and f-elements. In small core approximation, all states with $n \in \{N-1, N\}$ (n is a principal quantum number; N is a period in the Periodic Table) are explicitly cast as valence, the states belonging to $(N-1)$ are called semicore states.

2.1.4 Evaluation of integrals

The total electronic energy per unit cell may be written as

$$E_e = \frac{1}{2} \sum_{\mu\nu} \sum_{\boldsymbol{g}} P_{\mu\nu}^{\boldsymbol{g}} (H_{\mu\nu}^{\boldsymbol{g}} + G_{\mu\nu}^{\boldsymbol{g}}), \qquad (2.25)$$

which includes the sum of one- (H) and two-electron (G) terms. For instance, the Coulomb and exchange contributions to the total energy can be written as

following:

$$E_e^{coul} = \frac{1}{2} \sum_{\mu\nu} \sum_{\boldsymbol{g}} P_{\mu\nu}^{\boldsymbol{g}} \sum_{\alpha\beta} \sum_{\boldsymbol{n}} P_{\alpha\beta}^{\boldsymbol{n}} \sum_{\boldsymbol{h}} (\chi_\mu^{\boldsymbol{0}} \chi_\nu^{\boldsymbol{g}} | \chi_\alpha^{\boldsymbol{h}} \chi_\beta^{\boldsymbol{h+n}}) \qquad (2.26)$$

$$E_e^{exch} = -\frac{1}{4} \sum_{\mu\nu} \sum_{\boldsymbol{g}} P_{\mu\nu}^{\boldsymbol{g}} \sum_{\alpha\beta} \sum_{\boldsymbol{n}} P_{\alpha\beta}^{\boldsymbol{n}} \sum_{\boldsymbol{h}} (\chi_\mu^{\boldsymbol{0}} \chi_\alpha^{\boldsymbol{h}} | \chi_\nu^{\boldsymbol{g}} \chi_\beta^{\boldsymbol{h+n}}) \qquad (2.27)$$

In the CRYSTAL code five integral tolerances (ITOL1-5) control the accuracy of the calculation of bielectronic Coulomb and exchange series. Selection is based upon overlap-like criteria: when the overlap between two AOs is smaller than 10^{-ITOL}, the corresponding integral is discarded or evaluated in a less precise way (see CRYSTAL manual).

2.1.5   Reciprocal space integration

The exploitation of translational invariance results in solving the HFR equation at points of the BZ. A proper $\boldsymbol{k}$-point sampling is needed for integration in reciprocal space in order to adequately represent the electronic density and to evaluate the Fermi energy during the self-consistent procedure, as well as for calculations of properties when the one-electron density matrix is obtained (density of electronic states, band structure, etc.). The important theorem is that the energy $E(\boldsymbol{k})$ is a smooth function of $\boldsymbol{k}$ with a period of the reciprocal lattice basic translations (74). It allows one to make calculations at the finite number of $\boldsymbol{k}$ points, to apply an interpolation scheme and then to integrate over the BZ.

There are various approaches to choose the special points in the BZ (75; 76; 77). However, the Monkhorst-Pack scheme is the most widely used (76). A set of points is defined by the following relation and determines an equally spaced mesh in the BZ:

$$\boldsymbol{k}_{n_1, n_2, n_3} = \sum_i^3 \frac{2n_i - N_i - 1}{2N_i} \boldsymbol{b}_i \qquad (2.28)$$

where te $\boldsymbol{b}_i$ denote the reciprocal lattice vectors and N_i the shrinking factors for each direction.

For conducting solids where energy bands are not completely occupied, a second mesh, Gilat net (78), is used in the CRYSTAL code for the calculation of the density matrix and the determination of Fermi energy.

2.2 DFT plane wave formalism and the VASP code

2.2.1 General remarks

The use of plane wave basis set is an alternative approach to the LCAO expansion of one-electron eigenfunctions $\psi_{\boldsymbol{k}+\boldsymbol{q}}$:

$$\psi_{\boldsymbol{k}+\boldsymbol{q}}(\boldsymbol{r}) = \frac{1}{\sqrt{V}} \sum_{\boldsymbol{q}} c_{\boldsymbol{q}} e^{i(\boldsymbol{k}+\boldsymbol{q})\boldsymbol{r}}, \qquad (2.29)$$

where $\boldsymbol{k}$, $\boldsymbol{q}$ are reciprocal vectors and $c_{\boldsymbol{q}}$ are the expansion coefficients.

The method has proved to be very efficient in solid state physics since the 1970s due to a number of advantages mainly related to the simplicity of operations with exponents: (i) the calculation of matrix elements can be performed either in the reciprocal or direct space, and efficient algorithms such as the Fast Fourier Transforms (FFT) are applied to reduce the scaling of the computation with respect to the number of PWs used; (ii) the only parameter of the cut-off energy E_{cut} is required to control the quality of the basis set ($E_{cut} = \frac{\hbar^2 q_{max}^2}{2m}$, and all PWs with $|\boldsymbol{q}| \leq q_{max}$ are included in the eigenfunction expansion 2.29); (iii) PWs are independent of atomic positions and the forces on atoms can be calculated much easier. One of the main disadvantages of PWs, however, is that a huge number of PWs is needed to correctly describe atomic core regions, which leads to the additional difficulties in the small core potentials construction.

Recently, several approaches have been developed to construct pseudopotentials from first principles. The main idea is to use a pseudofunction that should be smooth inside the atomic core regions (core radius r_c) but identical to the actual wavefunction outside r_c. The idea of "hard" (*norm-conserving*) PPs ([79]) is that the pseudofunction inside r_c is normalized to the value corresponding to the atomic wavefunction of the all-electron problem. The normalization condition leads to the correct one-electron atomic energies ϵ and to a better PP transferability. However, a rich set of PWs are required to ensure the normalization. The approach of *ultrasoft* PPs suggested by Vanderbilt ([80]) does not require normalization, nevertheless resulting in a good description even with a smaller cut-off energy E_{cut} due to a more complicated KS scheme with several cut-off radii for the PP construction.

The *projected augmented-wave* (PAW) method proposed by Blöchl ([81]) provides the way of exact partitioning of the electron wavefunctions. The great advantages are that the all-electron solutions can be obtained and the approach can be effectively combined with the ultrasoft PPs technique.

2.2.2 The nudged elastic band method for transition state search

The problem of the search for a transition state corresponding to the saddle point on the potential energy surface is of central importance for finding mechanisms of chemical reactions or any other rearrangements of a group of atoms and estimating activation barriers for different possible process channels ([82]). The *nudged elastic band* (NEB) method belongs to a class of chain-of-states methods in which a number of images are generated to trace out a path, and the chain can be defined mathematically analogous to a Feynman path integral ([83; 84; 85]).

In the NEB method, an elastic band is a set of $(n + 1)$ images $\{\boldsymbol{R_0}, \boldsymbol{R_1}, ..., \boldsymbol{R_n}\}$ where $(n - 1)$ intermediate images are obtained by an interpolation of geometry

between the two endpoints $\boldsymbol{R_0}$ and $\boldsymbol{R_n}$. The force acting on the ith image can be determined as a sum of the true force and spring force:

$$\vec{F}_i = -\nabla V(\vec{R}_i) + \vec{F}_i^{spring} \qquad (2.30)$$

where

$$\vec{F}_i^{spring} \equiv k_{i+1}(\vec{R}_{i+1} - \vec{R}_i) - k_i(\vec{R}_i - \vec{R}_{i-1}) \qquad (2.31)$$

with some spring constants k. A useful modification of the method is to consider only the parallel component of the true force and the perpendicular component of the spring force (such projection is called 'nudging'). This provides a better convergence to the minimum energy path (MEP) because $(-\nabla\ V(\vec{R}_i)|_\perp)$ leads to the cutting of corners and an overestimate of the saddle point energy, while $\vec{F}_i^{spring}|_\parallel$ tends to pull the images off the MEP. The force defined is then minimized during the optimization process to provide the MEP and an estimate of the activation barrier over the path.

2.3   Periodic supercell model

In the periodic supercell approach an extended unit cell (supercell) is defined by a linear transformation connecting the basic translation vectors of the perfect crystal $\boldsymbol{a}_i$ with the translation vectors $\boldsymbol{A}_j$ of the supercell chosen:

$$\boldsymbol{A}_j = \sum_{i=1}^{3} l_{ij}\boldsymbol{a}_i, |\ det\ l\ | = L \qquad (2.32)$$

while a defect is enclosed in the supercell and periodically repeated throughout space. It is worth anticipating that the supercell must be chosen sufficiently large for the modeling of a single point defect in order to avoid spurious interaction between periodic replicas of a defect. The quantitative measure of such a defect interaction may be the dispersion of the one-electron defect level within the BZ

in the calculated band structure. The dispersion should approach zero for the completely isolated defect corresponding to the infinitely large supercell. It may be also noted that the supercell approach is the most widely used as it is easy to implement in all first-principles codes with periodic boundary conditions and it circumvents the problems with boundary conditions arising in the molecular cluster approach.

2.4 The Jahn-Teller effect

The Jahn-Teller theorem (60; 86; 87) provides criteria for the stability of symmetrical configurations of molecules or metal complexes. In a nutshell, it states that any non-linear molecule with a degenerate electronic ground state will undergo a geometrical distortion that removes that degeneracy, what in turn leads to lowering of the total energy of a system[1].

Let us consider a small distortion $\Delta \boldsymbol{R}_i$ from the equilibrium geometry $\boldsymbol{R}^0$ such that $\boldsymbol{R}^0 + \Delta \boldsymbol{R}_i = \boldsymbol{R}^1$ and try to find the equilibrium geometry using the first order perturbation theory. We can write down the Schrödinger equation as

$$[-\frac{\hbar^2}{2m}\Delta_r + V(\boldsymbol{r}, \boldsymbol{R}^1) + P(\boldsymbol{r})]\psi(\boldsymbol{r}) = E\psi(\boldsymbol{r}) \qquad (2.33)$$

where the perturbation potential

$$P(\boldsymbol{r}) = V(\boldsymbol{r}, \boldsymbol{R}^0) - V(\boldsymbol{r}, \boldsymbol{R}^1) = \sum_i \left(\frac{\partial V(\boldsymbol{r}, \boldsymbol{R})}{\partial \boldsymbol{R}_i} \right)_{\boldsymbol{R}^1} \Delta \boldsymbol{R}_i + O(\Delta \boldsymbol{R}_i^2) \qquad (2.34)$$

Turning to the normal coordinates q_α which transform according to the irrep Γ of G (symmetry group of $\boldsymbol{R}^1$), we can rewrite the perturbation as

---

[1]As E. Teller pointed out (88), the idea of theorem is due to L. Landau who suggested it back in 1934, but it was proved by H. Jahn and E. Teller in 1937 based upon a group-theoretical analysis of all molecular point groups

$$P = \sum_\alpha \left(\frac{\partial V}{\partial q_\alpha}\right)_{q=0} q_\alpha \tag{2.35}$$

where α runs over all coordinates. We can find the energy correction caused by perturbation. If the energy is s-fold degenerate with the orthonormal set of eigenstates $\{\psi_i\}_{i=1}^s \in D$ (D is an irrep of G), then the energy correction is given by the roots of the secular equation

$$|p_{ij} - \lambda \delta_{ij}| = 0 \tag{2.36}$$

where

$$p_{ij} = \int \psi_i^*(\boldsymbol{r}) \sum_\alpha \left(\frac{\partial V}{\partial q_\alpha}\right)_0 q_\alpha \psi_j(\boldsymbol{r}) d\boldsymbol{r} \tag{2.37}$$

If the energy is negative, then the configuration $\boldsymbol{R}^0$ is unstable.

Using the Wigner-Eckart theorem of group theory (60), we can find all matrix elements $\langle i|\hat{O}|j\rangle$ for any Hermitian operator $\hat{O}$ as products of the Clebsh-Gordan coefficients (tabulated for many groups) and the overlap matrix. However, it frequently suffices to know only whether the matrix elements vanish because of symmetry. It can be proved that $\langle i|\hat{O}|j\rangle \neq 0$ if and only if $\Gamma_{\hat{O}} \in \Gamma_i^* \otimes \Gamma_j$, where $\Gamma_\alpha(\alpha = \hat{O},i,j)$ stands for the corresponding irrep.

In the context of the JT effect, we have to find the matrix elements:

$$\int \psi_i^*(\boldsymbol{r}) \left(\frac{\partial V}{\partial q_\alpha}\right)_0 \psi_j(\boldsymbol{r}) d\boldsymbol{r} \tag{2.38}$$

which are called *linear orbital vibronic constants* (87). Physically, each diagonal vibronic term represents the force with which the electron on the ith CO distorts the nuclear configuration in the direction of the symmetrized displacement q_α. It is easy to show that $\left(\frac{\partial V}{\partial q_\alpha}\right)_0$ transform like the normal coordinates q_α according to the same irrep Γ of group G. Thus, we know all the irreps needed to decide whether or not the elements (2.38) are zero.

Let us consider the example relevant to the present study, namely, the Fe impurity center in $SrTiO_3$ crystal where the JT distortion around the Fe^{4+} ion appears (89). In the crystal field produced by the oxygen ions in an octahedral FeO_6 complex (point group O_h), the d state with four ferromagnetically coupled electrons of the free Fe^{4+} ion splits into a t_{2g} and an e_g levels. Three of the electrons go into a deeper t_{2g} level, while the remaining d electron occupies the energetically higher e_g orbitals. The latter electron is more mobile and may effectively interact with the vibrations of the complex causing the JT coupling. For instance, the expansion of symmetric product of the irreps for an e_g term in the O_h octahedral environment $e_g \otimes e_g$ includes e_g which are, therefore, the JT active modes. Since e_g are 2-fold degenerate, there are two possible symmetrized displacements that can be expressed by Cartesian coordinates following (87) as $q_1 = (2z_1 - 2z_4 - x_2 + x_5 - y_3 + y_6)/2\sqrt{3}$ and $q_2 = (1/2)(x_2 - x_5 - y_3 + y_6)$. Our actual *ab initio* modeling results on the JT effect, as will be presented below, demonstrate that the resulting displacements correspond to q_1 mode (2 Fe–O bonds along the z axis lengthen and 4 Fe–O bonds in the xy plane shorten).

2.5 Computational details

In the present study, we have primarily exploited the hybrid HF-DFT methodology with the B3PW exchange-correlation functional (65) in the framework of the LCAO approximation as implemented in the CRYSTAL-2006 code (62). For a comparison, several calculations were done using a plain DFT-LCAO method within the generalized gradient approximation (GGA) with the Perdew-Becke-Erzenhof (PBE) density functional (90). Small core Hay-Wadt pseudopotentials (72) were used for the core electrons of Sr and Ti atoms while the outermost shell basis functions have been earlier optimized for $SrTiO_3$ bulk crystal (11). For oxygen atoms all-electron Gaussian basis sets of type 8-411G* were taken from the

same study. The Fe atom was represented by an all-electron basis set (91) optimized for the α-Fe_2O_3 (hematite) crystal. Our attempts of further optimization of this basis for the bulk $SrFeO_3$ decreased the total energy only insignificantly. In order to analyze properties of the oxygen vacancies, we have employed a "ghost" wave function approach meaning that the basis set of the removed oxygen atom is retained at the vacant site. For the calculation of a free oxygen atom as the reference state in computing vacancy formation energy, the atomic 6-311 basis set was used. The use of a larger basis has not changed significantly the values of ground state energy.

In all calculations we have chosen the threshold parameters as 10^{-6}, 10^{-6}, 10^{-6}, 10^{-6} and 10^{-12} for the Coulomb overlap, Coulomb penetration, exchange overlap, the first exchange pseudo-overlap and for the second exchange pseudo-overlap, respectively. In the summation over the BZ, we have adopted the Monkhorst-Pack (76) mesh of $\boldsymbol{k}$-points. In the cases of bulk $SrTiO_3$ and $SrFeO_3$ crystals we studied the convergence of energy with an increasing number of used $\boldsymbol{k}$-points and found a 8×8×8 for the semiconducting $SrTiO_3$ and a 16×16×16 for the metallic $SrFeO_3$ to be large enough for achieving a good convergence. Both orthorhombic and monoclinic phases of $CaFeO_3$ were treated with a 8×8×6 set of $\boldsymbol{k}$-points.

Performing the complete structural optimizations around the point defects, we have reduced the symmetry of a supercell under consideration from the cubic $Pm\bar{3}m$ to tetragonal $P4/mmm$ to be able to obtain less symmetrical distortions including the Jahn-Teller effect. To find the atomic equilibrium positions, we have applied the Schlegel conjugate gradient algorithm. Convergence during the geometry optimization process is tested on the root mean square (rms) and the absolute value of the largest component of both the gradients and the nuclear displacements. The default thresholds for the maximum and the rms forces and the maximum and the rms atomic displacements on all atoms were set to 0.00045,

0.00030 and 0.00180, 0.00120 a.u., respectively. Optimization is considered as completed as soon as the four conditions are simultaneously fulfilled.

The calculations of Raman and Infrared frequencies for $CaFeO_3$ at the Γ-point of the BZ were done within the harmonic approximation (92; 93). The frequencies are obtained by diagonalizing the mass-weighted Hessian matrix with the elements $W_{ij} = H_{ij}/\sqrt{M_i M_j}$, where M_i and M_j are the masses of the atoms with i and j coordinates, respectively. For the analysis of atomic contributions to the phonon modes in a given frequency range, the isotopic substitution technique was applied by changing the atomic masses (^{40}Ca to ^{42}Ca, ^{56}Fe to ^{58}Fe and ^{16}O to ^{18}O) in the mass-weighted Hessian when the latter is obtained.

As we mentioned, the DFT plane wave calculations were carried out using the VASP code (4.6 version) (68; 69; 70). We have used the generalized gradient approximation (GGA) with the Perdew-Becke-Erzenhof (PBE) density functional (90). The interaction between the valence and core electrons was described with the projected augmented wave (PAW) (81). We have used here small core PPs for all atoms: $4s^2 4p^6 5s^2$ electrons of Sr atom are explicitly treated as valence, for Ti and O - $3s^2 3p^6 4s^2 3d^2$ and $2s^2 2p^4$, respectively. We have kept a cut-off energy of 520 eV (i.e., 120 eV larger than the recommended value for the set of PPs employed) to reduce finite sampling error, while a value of 600 eV was chosen for the fast Fourier transform (FFT) grid. All calculations were performed with a complete structural optimization using a conjugate gradient technique with an iterative relaxation of the atomic positions until the forces on the atoms were less than 0.01 eV Å^{-1}. For the calculation of $SrTiO_3$ supercells with 80 and more atoms, we have used $2\times2\times2$ $\boldsymbol{k}$-point mesh for sampling the reciprocal space, while the calculations of primitive cells were performed with much denser grids (see below the bulk calculations of perfect $SrTiO_3$ and $SrFeO_3$ crystals).

In this work we considered supercells of different shapes and sizes obtained by extending the basis lattice vectors of a cubic $SrTiO_3$ and substituting the

titanium atom in the origin of a cell by an iron in order to create a defective system. The 135-atom simple cubic (sc), 80- and 270-atom face-centered (fcc) and 160-atom body-centered (bcc) cells were created by using the transformation matrices defined in Equation 2.32:

$$\begin{vmatrix} n & 0 & 0 \\ 0 & n & 0 \\ 0 & 0 & n \end{vmatrix}, \quad \begin{vmatrix} 0 & n & n \\ n & 0 & n \\ n & n & 0 \end{vmatrix} \quad \text{and} \quad \begin{vmatrix} -n & n & n \\ n & -n & n \\ n & n & -n \end{vmatrix} \tag{2.39}$$

respectively, where n is varied between 2 and 4. These transformations generate sc, fcc and bcc lattices of supercells, respectively.

Thus, the supercell with sc extension of $3\times3\times3$ contains 135 atoms and corresponds to 3.7% of iron concentration in $SrFe_xTi_{1-x}O_3$ solid solution. The supercells with fcc extensions of $\sqrt{2}\times\sqrt{2}\times\sqrt{2}$ (10 atoms), $2\sqrt{2}\times2\sqrt{2}\times2\sqrt{2}$ (80 atoms) and $3\sqrt{2}\times3\sqrt{2}\times3\sqrt{2}$ (270 atoms) are rhombohedral with an angle of 60° between the lattice vectors corresponding to 50, 6.25 and 1.85% Fe, respectively. The last considered supercell is the 160-atom rhombohedral bcc cell with an angle of 109.47° (extension $2\sqrt{3}\times2\sqrt{3}\times2\sqrt{3}$) that corresponds to 3.125% Fe.

Calculations of surfaces are carried out in a slab model framework in which surface supercell is constructed by an extension of surface basic translation vectors in xy plane (55). Results are converged to a large enough slab thickness. Note that in the PW simulations, sufficiently large vacuum gap between periodically repeated slabs in z-direction must be chosen to preclude the spurious interaction between surface replicas along z axis.

Chapter 3

Bulk properties of perfect ABO$_3$ perovskite crystals

This section reports on basic properties of non-defective crystals providing a comparison of the results on lattice constant, bulk modulus, cohesive energy and band structure obtained by several computational schemes, as well as electronic structure and vibration frequency calculations of two phases of CaFeO$_3$ crystal within the hybrid HF-DFT LCAO method.

3.1   Parent compounds SrTiO$_3$ and SrFeO$_3$

To start with, let us present simulation results on the perfect SrTiO$_3$ and SrFeO$_3$ crystals which are the two end-members in a series of SrFe$_x$Ti$_{1-x}$O$_\delta$ solid solutions. A wealth of available experimental and theoretical information about these two solids allows us to apply several computational schemes in order to demonstrate their strengths and shortcomings in studying particular properties relevant to our principal investigation.

The SrTiO$_3$ and SrFeO$_3$ crystals adopt exactly the same perovskite cubic structure (P$m\bar{3}m$ space group) while exhibiting very different properties. In fact,

SrTiO$_3$ is a semiconductor with an experimental band gap of 3.3 eV ([10]), while SrFeO$_3$ exhibits a metallic conductivity ([94]). It is also well-known from the experimental data that both these crystals do not exhibit a Jahn-Teller local lattice distortion around B cation.

A number of approaches has been earlier applied to describe the properties of these materials. One of the useful semiempirical approaches is the ligand field theory and the cluster model calculation for interpreting experimental spectra ([95]). These approaches allow one to qualitatively describe the electronic structure of the ground state by expanding its wave function in terms of single ionic configurations which can significantly contribute to the ground state of a crystal. In ([96]) this approach has been applied to the interpretation of x-ray photoemission (XPS) and ultraviolet photoemission (UPS) SrFeO$_3$ spectroscopic data. It has been clearly shown that the simulation can reproduce the experimental spectrum only if several single configurations have been included additionally to the $d^4(t_{2g}^3 e_g^1)$ configuration. By using the configuration interaction (CI) cluster model with three adjustable parameters, the authors ([96]) have found that the ground state is dominated by the $3d^5\underline{L}$ rather than the $3d^4$ configuration (where $\underline{L}$ denotes a ligand hole) and that this can suppress the JT distortion of the d^4 ion. A large contribution of the $3d^5\underline{L}$ configuration to the ground state gives rise to the presence of itinerant d electrons, thus leading to metallic conductivity in SrFeO$_3$. This semiempirical model also enables one to discuss the effects of covalency by estimating the occupancies of different configurations. Using the same approach for the interpretation of x-ray absorption spectra (XAS) of SrFeO$_3$ ([97]), the authors have obtained the following occupancies of different configurations in percentage terms: 36% $3d^4$, 58% $3d^5\underline{L}$ and 6% $3d^6\underline{L}^2$. The obtained population of the Fe $3d$ orbital is approximately 4.7 and hence larger than the pure ionic value of 4.0 reflecting significant degree of covalency in SrFeO$_3$.

The electronic properties of SrTiO$_3$ and SrFeO$_3$ crystals have also been cal-

culated by exploiting a number of *ab initio* approaches (9; 11; 98; 99). Band structure calculations of SrTiO$_3$ have confirmed the semiconducting nature of the crystal with the top of the valence band being predominantly formed by O $2p$ atomic orbitals and the bottom of the conduction band mainly consisting of Ti $3d$ states. The bond population analysis demonstrates a large overlap between O $2p$ and Ti $3d$ orbitals confirming the covalent nature of the Ti-O chemical bonding (11). The SrFeO$_3$ is much less understood. Its electronic and magnetic properties have been studied by means of the tight-binding linear muffin-tin orbital method within the atomic sphere approximation (TB LMTO-ASA)(100), the augmented spherical wave (ASW) method (101) and pseudopotential LSDA $+ U$ (102) band structure calculations. In (102; 103) the ferromagnetic (FM) and different anti-ferromagnetic (AFM) spin configurations of SrFeO$_3$ have been examined in the DFT plane wave simulations and the ferromagnetic state has found to be the most favorable among the collinear magnetic phases. The energy bands, density of electronic states and some bulk properties are calculated here.

In Table 3.1 we present the results on basic bulk properties calculated using three different approaches: the hybrid method with the B3PW functional and two plain DFT methods in LCAO and PW basis sets with exactly the same PBE-GGA (90) Hamiltonian. The hybrid approach gives very reasonable results, both for the lattice constant and atomization energy, thus promising a good description of structural and energetic properties. The bulk modulus in the hybrid method is overestimated because the HF Hamiltonian tends to overestimate the second derivative of the energy. Also, as well known from literature, the hybrid Hamiltonian provides the best agreement with experimental optical band gap whereas the DFT methods underestimate this quantity considerably (55). Note, however, that all approaches used give largely the same qualitative picture of the energy bands in the BZ as clearly seen from the calculated band structures in Figure 3.1.

Table 3.1: Experimental and calculated lattice constant a_0, bulk modulus B, atomization energy E_{at} and energy bandgap E_{gap} of SrTiO$_3$

	a_0, Å	B, GPa	E_{at}, eV	E_{gap}, eV
LCAO-B3PW	3.892	193	31.4	3.6
LCAO-PBE	3.921	176	33.5	2.0
PW-PBE	3.941	172	31.7	1.8
Experiment	3.905[1]	179[2]	31.7[3]	3.3[4]

[1]Ref.(104)

[2]Ref.(105)

[3]Ref.(106)

[4]Ref.(10)

Table 3.2 contains the properties calculated for the FM phase of SrFeO$_3$. In this case, both hybrid LCAO and DFT-PBE approaches give lattice constants very close to the experimental values. As expected, the DFT-PBE method based upon PW basis expansion provides a very good description for the metallic crystal.

As to the SrFeO$_3$ magnetic properties, we first performed a comparative analysis of collinear ferromagnetic (FM) and antiferromagnetic (A, C and G types) states (Figure 3.2). To carry out a consistent comparison of total energy values of the phases, we used supercells twice extended in each unit vector direction and thus composed of 8 unit cells for all AFM states, proportionally to cubic FM state reducing the $\boldsymbol{k}$-points sampling in the BZ (i.e., by factor of 2). The determined sequence of stability obtained from the B3PW calculation is FM < AFM-A < AFM-C < AFM-G, i.e., the ferromagnetic state is the most favorable. These results agree with the experimental indication that the ferromagnetic interactions in SrFeO$_3$ are significantly stronger than antiferromagnetic interactions (102). Then, for the ferromagnetic phase we considered states with different possible total spin projections and estimated the energetic sequence of spin states. From
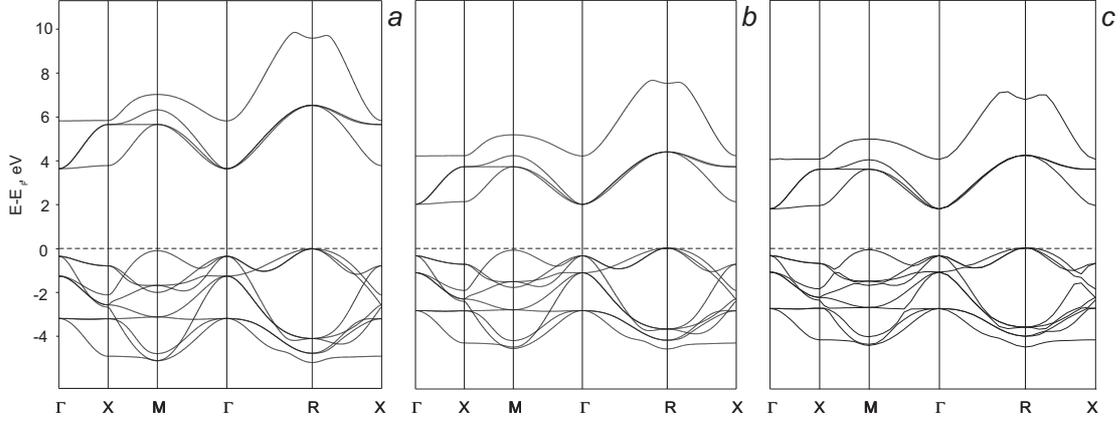
Figure 3.1: Energy bands of calculated SrTiO$_3$ by means of three methods: the hybrid HF-DFT with B3PW functional in LCAO (*a*), the DFT-PBE in LCAO (*b*) and DFT-PBE in PW (*c*). All bands are shifted at the value of Fermi energy; the dashed lines denote the top of the valence band.

Table 3.3 one can see that all methods applied yield the state with the total spin projection S$_z$ = 2 as the most favorable one.

The calculated band structure of the FM phase is displayed in Figure 3.3, while the partial density of electronic states will be shown later in Figure 4.2 and discussed in more detail in context of SrFe$_x$Ti$_{1-x}$O$_3$ solid solution members. We note here that the major contribution in the vicinity of the Fermi level originates from Fe 3d (e_g) and O 2p states, causing the metallic behavior, which is well compatible with a cluster model (CI) prediction (96) and a recent LSDA plane wave simulation (103).

3.2   CaFeO$_3$

Here we present the results of our modeling on CaFeO$_3$ crystal which has recently attracted a great deal of attention, particularly, in connection with ordering of

Table 3.2: Experimental and calculated lattice constant a_0, bulk modulus B and atomization energy E_{at} of ferromagnetic SrFeO$_3$

	a_0, Å	B, GPa	E_{at}, eV
LCAO-B3PW	3.856	-	29.7
LCAO-PBE	3.875	168	33.0
PW-PBE	3.850	169 (171[1])	-
Experiment	3.850[2]	-	-

[1]LSDA+U calculation with the VASP code from (102)

[2]Ref.(107)

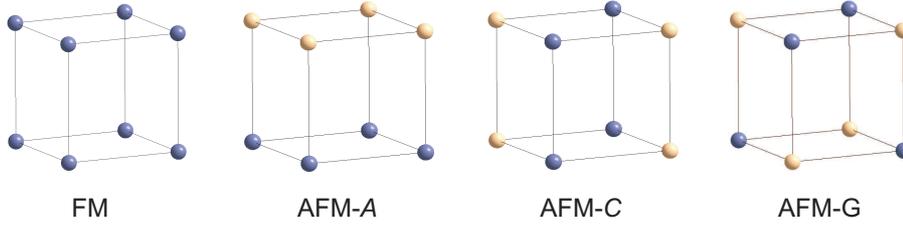FM   AFM-*A*   AFM-*C*   AFM-G

Figure 3.2: The iron sublattice of SrFeO$_3$ crystal lattice with collinear ferromagnetic (FM) and antiferromagnetic (*A*, *C* and *G*) types of ordering; two colors distinguish spin up and down electrons.

Table 3.3: Energy differences in eV between different magnetic spin states of ferromagnetic SrFeO$_3$ with respect to the state with S$_z = 2$

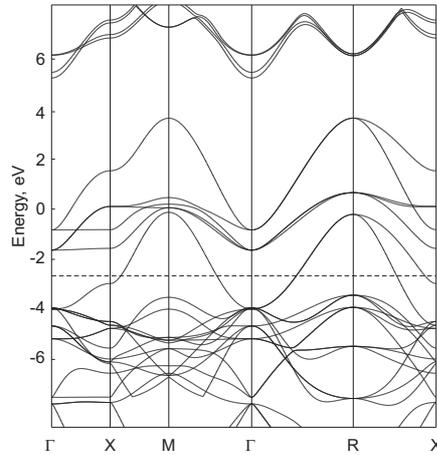|	S$_z = 0$	S$_z = 1$	S$_z = 2$	S$_z = 3$
LCAO-B3PW	3.2	1.6	0.0	1.3
LCAO-PBE	1.3	0.6	0.0	2.2
PW-PBE	1.0	0.4	0.0	1.8

Figure 3.3: Energy band structure of ferromagnetic SrFeO$_3$ crystal calculated using the LCAO-B3PW method. All bands are shifted at the value of Fermi energy; the dashed lines denote the top of the valence band.

charge, spin and orbital degrees of freedom. If SrTiO$_3$ and SrFeO$_3$ crystals are opposite cases in their metallic properties (the former is wide-gap semiconductor, the latter is metal), CaFeO$_3$ is a fascinating material in which the change from metallic to semiconducting behavior takes place in form of a phase transition from the room-temperature orthorhombic (space group *Pbnm*) to a monoclinic (space group $P2_1/n$) modification, which is stable below 290 K (Ref.(108)). It is believed that this electronic transition with opening a small gap is caused only by a slight structure distortion where two groups of Fe–O distances (differ in length by 0.1 Å) arise in the monoclinic phase and the Fe–O–Fe angles are changed. The decrease of these angles leads to a less effective overlap between Fe 3d and O 2p orbitals, thus possibly opening a gap.

In addition, such a metal-insulator transition is accompanied by a *charge disproportionation* between two inequivalent iron ions in the monoclinic phase, as revealed by Mössbauer spectroscopy (109), but the degree of this disproportionation is rather unclear. Also, recent neutron powder-diffraction experiments (108)

found out considerably different magnetic moments on the two iron sites, however, the absolute values depend largely on the model of magnetic arrangement (spiral or sinusoidal) used for the interpretation of data.

There were only a few theoretical attempts to examine properties of both CaFeO$_3$ phases. For instance, calculation of the electronic structure and magnetic properties has been performed using the LSDA $+$ U approach (110) containing two adjustable parameters. However, the arbitrariness in choosing these parameters is a crucial shortcoming of the method. Thus, the authors obtained rather large variations in the magnetic moments on the iron atoms depending on the parameter values.

Taking into account all the above mentioned, we aim to provide the results of first-principles calculations of the atomic structure, electronic and magnetic properties of CaFeO$_3$ as well as the Γ-point vibrational frequencies. To this end, we have chosen the hybrid HF-DFT method with the B3PW exchange-correlation functional (65) as implemented in the LCAO-based CRYSTAL-2006 computer package (62). Note that the application of a hybrid functional in the calculations of CaFeO$_3$ is necessary for reliable discrimination of small changes in the band gap and electronic properties (11) related to the CaFeO$_3$ phase transition as well as for analysis of the phonon modes (93). We employed the Monkhorst-Pack (76) 8×8×6 set of **k**-points for the summation in the Brillouin zone as sufficiently large to obtain a good agreement with experimental data on atomic structure and Raman frequencies. All atoms were treated at the all-electron level with the use of optimized basis sets (Ca Ref.(111), Fe Ref.(91), O Ref.(11)). For the full optimization of the CaFeO$_3$ atomic structures, we used the two-step iterative procedure, in which the lattice parameters are optimized at fixed atomic positions, then atomic coordinates are optimized at fixed cell parameters and this procedure repeated until convergence criteria for both steps are fulfilled.

In Tables 3.4 and 3.5 the calculated and experimental lattice parameters and

40

Table 3.4: Optimized and experimental (108) unit cell parameters a, b, c (Å) and angle β (°) for orthorhombic *Pbnm* and monoclinic *P2$_1$/n* phases.

Parameter	Orthorhombic			Monoclinic			
	a	b	c	a	b	c	β
Calculation	5.330	5.346	7.565	5.317	5.349	7.562	90.001
Experiment	5.326	5.353	7.540	5.312	5.348	7.521	90.065

atomic coordinates are presented. Calculations were carried out for the FM spin configuration with four unpaired electrons on each iron site which has been found to be the most favorable magnetic ordering. We found the monoclinic phase is energetically more favorable (by ∼0.25 eV/cell) than the orthorhombic one, in agreement with the experimental observation that the monoclinic phase is a low-temperature phase. Importantly, the optimization of the hypothetical cubic phase in *Pm$\bar{3}$m* space group symmetry yields an energy which is the highest among all modifications considered.

As seen from Tables 3.4 and 3.5, the orthorhombic modification is very slightly distorted from a cubic symmetry, while the monoclinic one presents a slightly distorted orthorhombic phase. It should be mentioned that the Fe–O bond lengths in the monoclinic phase fall into two groups corresponding to two inequivalent Fe ions with the averaged Fe–O distances of 1.87 Å and 1.97 Å. This indicates two types of chemically different iron sites, although in the orthorhombic phase with all equivalent iron atoms the averaged Fe–O bond lengths group around 1.92 Å.

The results of Mulliken population analysis are given in Table 3.6. It is seen that the atomic charges support the general idea of *charge ordering* in the monoclinic phase. However, the difference between Fe(1) and Fe(2) charges is very small. It should be noted that in experiments the degree of this charge disproportionation varies with temperature (112) and our results, obtained formally at 0 K, are in line with those of the LSDA + U calculations (110).

Table 3.5: Optimized and experimental (108) fractional atomic coordinates for orthorhombic *Pbnm* and monoclinic $P2_1/n$ phases.

Atom	Site	Calculation			Experiment		
		x	y	z	x	y	z
			Orthorhombic				
Ca	4c	0.995	0.033	0.250	0.995	0.033	0.250
Fe	4b	0.0	0.5	0.0	0.0	0.5	0.0
O(1)	8d	0.710	0.285	0.032	0.713	0.286	0.033
O(2)	4c	0.062	0.485	0.25	0.066	0.491	0.25
			Monoclinic				
Ca	4e	0.995	0.035	0.250	0.994	0.037	0.251
Fe(1)	2d	0.5	0.0	0.0	0.5	0.0	0.0
Fe(2)	2c	0.0	0.5	0.0	0.0	0.5	0.0
O(1)	4e	0.296	0.717	-0.032	0.300	0.720	-0.033
O(2)	4e	0.218	0.205	-0.032	0.219	0.206	-0.032
O(3)	4e	0.063	0.486	0.257	0.076	0.493	0.254

Table 3.6: Mulliken population analysis of atomic net charge ($\alpha+\beta$) and net spin ($\alpha-\beta$).

			Orthorhombic			
Density	Ca	Fe		O(1)	O(2)	
$\alpha+\beta$	1.75	2.25		-1.33	-1.34	
$\alpha-\beta$	0.01	3.71		0.10	0.09	
			Monoclinic			
Density	Ca	Fe(1)	Fe(2)	O(1)	O(2)	O(3)
$\alpha+\beta$	1.75	2.26	2.24	-1.33	-1.33	-1.34
$\alpha-\beta$	0.01	3.13	4.10	0.13	0.13	0.13
$\alpha-\beta$[1]		2.40	3.90			
$\alpha-\beta$ (exp.[108])		2.48[2]/3.40[3]	3.47/5.02			

[1]LSDA + U calculation [110] performed with the onsite Coulomb parameter U = 0.4 Ry and the intra-atomic exchange parameter $J = 0.07$ Ry

[2]Spiral model for the interpretation of the neutron diffraction experiment

[3]Sinusoidal model

In contrast to small differences in charges, we observe a considerable splitting between spin densities on the two iron sites, corroborating the existence of spin ordering in the monoclinic phase. Such a significant difference in magnetic moments qualitatively agrees with Ref.[110] and the experimental estimates from neutron diffraction data [108] as seen from the Table 3.6. The precise determination of absolute values of magnetic moments on Fe atoms from the neutron diffraction experiments [108] is difficult because, firstly, various experimental models (spiral or sinusoidal) lead to quite different results and, secondly, the obtained experimental spectra exhibit rather broadened magnetic peaks. Nevertheless, both experiment and our calculations reveal very distinct magnetic moments on the two iron sites in the monoclinic phase.

For the analysis of electronic properties of CaFeO$_3$, we calculated the band structure and projected density of electronic states (PDOS) for both structural modifications. The DOS projected onto Fe $3d$ and O $2p$ states demonstrates a strong mixing of these states in the orthorhombic phase, being responsible for a metallic behavior, while this mixing decreases in the monoclinic phase due to a larger lattice distortion and change in the Fe–O–Fe angles, thus opening a small band gap ($\sim$0.9 eV). The PDOS for spin up and spin down electrons for both CaFeO$_3$ phases are shown in Figure 3.4. Note that there are obvious similarities between orthorhombic CaFeO$_3$ and cubic SrFeO$_3$, pertaining to the magnetic structures and electronic properties. Thus, both crystals have the FM spin arrangement with close magnetic moments on Fe atoms (3.71 vs. 3.79 μ_B, respectively) and their electronic conductivity is caused by an effective mixing of the Fe $3d$ and O $2p$ orbitals in the vicinity of Fermi level.

The results of lattice dynamics simulations were obtained within the harmonic approximation as implemented in the CRYSTAL-2006 code (92; 93). The vibrational frequencies at the Γ-point of the BZ are obtained by diagonalizing the mass-weighted Hessian matrix with elements $W_{ij} = H_{ij}/\sqrt{M_i M_j}$, where M_i and M_j are the masses of the atoms with i and j coordinates, respectively. For the analysis of atomic contributions to the phonon modes in a given frequency range, the isotopic substitution technique was applied by changing the atomic masses in the mass-weighted Hessian when the latter is obtained.

As mentioned above, the CaFeO$_3$ monoclinic phase belongs to the $P2_1/n$ space group whose reducible representations at the Γ point in the basis of the Cartesian atomic coordinates in the unit cell can, in according to the C$_{2h}$ point group symmetry, be decomposed as

$$\Gamma_{total} = 12A_g + 18A_u + 12B_g + 18B_u$$

where A_g, B_g are Raman active, and A_u, B_u are infrared active modes. Three modes are acoustic (pure translations) whose calculated frequencies deviate from
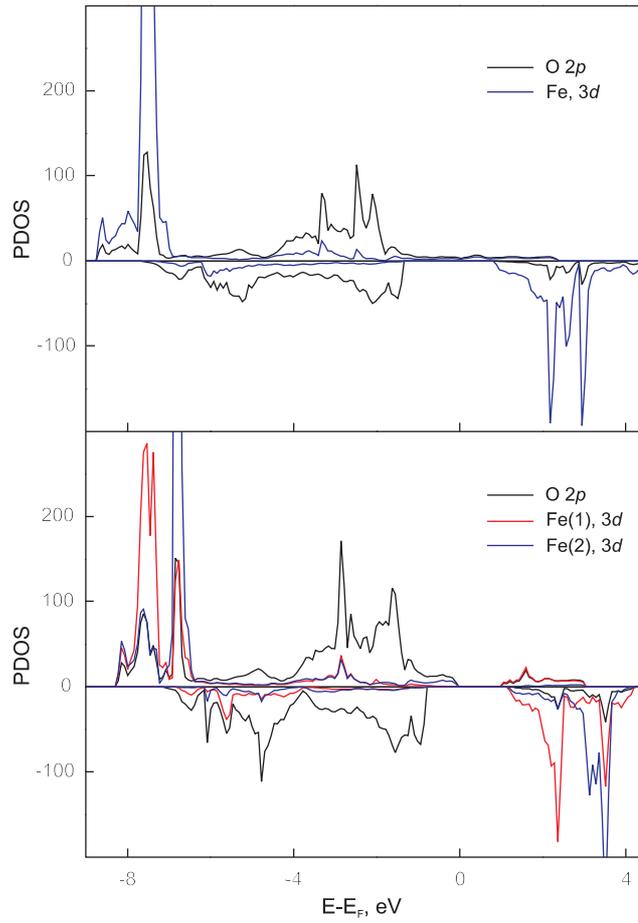
Figure 3.4: The density of electronic states projected onto Fe $3d$ and O $2p$ orbitals for orthorhombic (upper panel) and monoclinic (lower panel) phases of CaFeO₃ (projections are made onto only symmetrically inequivalent atoms).

Table 3.7: Calculated and experimentally observed at 15 K (given in the footnote, Ref.(113)) Raman active modes (cm^{-1})

A_g	146.0^1	157.8	214.8^2	244.5	266.5	298.1	352.1	374.1
	402.0	456.8	464.4	624.5				
B_g	155.6	176.6	185.0^3	231.1	247.2	317.6^4	370.1	381.5
	445.9	487.0	583.7	615.4				

[1]154

[2]219

[3]199

[4]306

Table 3.8: Calculated optical active modes (cm^{-1})

A_u	139.7	167.1	173.0	176.2	219.4	227.2	244.1	273.3	307.3
	322.1	351.7	409.1	458.3	476.4	535.7	544.7	549.1	
B_u	151.8	167.6	199.8	214.1	229.1	232.3	274.2	300.6	325.6
	381.2	411.2	411.2	452.6	524.2	557.7	565.5		

zero by only 1-2 cm^{-1}, reflecting the reasonable accuracy in the phonon calculations.

Tables 3.7 and 3.8 compile the Raman and optical vibration frequencies, respectively, of the monoclinic $CaFeO_3$ labeled by symmetry of each mode. The Raman active modes are compared with those experimentally observed in Ref.(113) at 15 K. Our analysis of the Raman normal modes results in the same vibrational patterns as revealed by using the lattice-dynamical calculations based on a semi-empirical approach (113).

It is known that the isotopic substitution is a helpful tool for the identification of the vibrational pattern of the modes. Figure 3.5 illustrates isotopic effects related to the substitution of ^{40}Ca by ^{42}Ca (a), ^{56}Fe by ^{58}Fe (b) and ^{16}O by ^{18}O (c). It is clearly seen that for the atoms of each element there is a region where
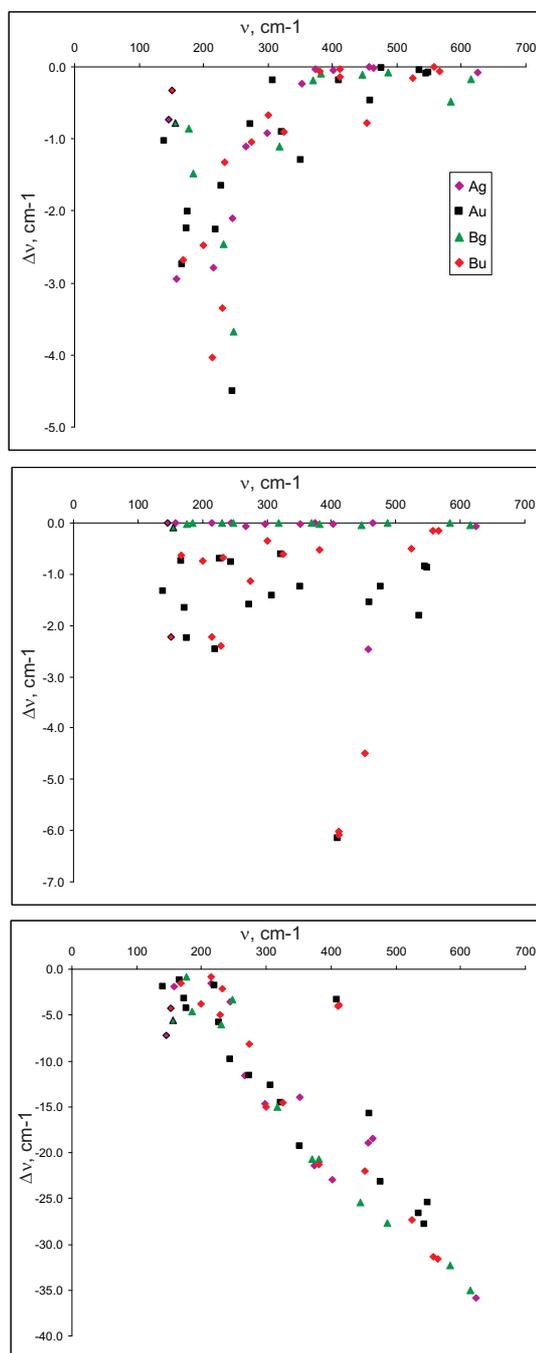
Figure 3.5: Vibration frequency isotopic shifts ($\Delta\nu$) for three types of isotopic substitutions: a) ^{42}Ca replacing ^{40}Ca; b) ^{58}Fe replacing ^{56}Fe; c) ^{18}O replacing ^{16}O. All normal modes are labeled according to the symmetry.

these atoms give a predominant contribution. Thus, one recognizes that Ca participates mainly in low-frequency modes (around 220 cm^{-1}) while Fe participates particularly in the modes with frequencies of 453 and 458 cm^{-1}. It is also observed that isotopic shifts are generally the largest for O atoms, their involvement into the vibrations steadily increasing when going to higher frequencies.

3.3 Conclusion

Summing up the results of this chapter, we have first performed a comparative analysis of a range of $SrTiO_3$ and $SrFeO_3$ properties using three DFT-based approaches. We have demonstrated that the hybrid HF-DFT LCAO method with the B3PW functional provides the best agreement with available experimental data on crystal atomization energy, atomic and electronic structure, elastic and magnetic properties. By applying this approach, we have also examined in a comparative way both orthorhombic and monoclinic phases of $CaFeO_3$. Despite small structural difference, the hybrid method agrees very well with neutron diffraction data. It also correctly reproduces the transition from a metallic orthorhombic phase to a semiconducting monoclinic one with an energy gap of 0.9 eV. In addition, we have studied the $CaFeO_3$ lattice dynamics at the Γ-point of the BZ by calculating Raman and optical vibration modes, the former frequencies being well compatible with low-temperature Raman experimental values.

Chapter 4

Point defects in SrTiO$_3$ bulk

This Chapter focuses on substitutional iron impurity and oxygen vacancy as crucial point defects in ABO$_3$-type perovskites. In Fe-doped SrTiO$_3$ crystal, we pay particular attention to the Jahn-Teller effect, electronic structure changes and the energetics of iron insertion for a whole range of iron content. Oxygen vacancies are examined in neutral and positive singly-charged states with an emphasis on atomic geometry, electronic structure, as well as diffusion process. Clustering of iron impurity and the oxygen vacancy is also studied and discussed.

4.1   Single iron impurity

Owing to the very different physico-chemical properties of the end-members, it is of great significance to study a series of SrFe$_x$Ti$_{1-x}$O$_3$ solid solutions. Whilst these compositions have been experimentally investigated within quite an intensity, even as a function of oxygen deficiency, there is still a lack of theoretical investigations.

We start with a single Fe impurity, x $\rightarrow$ 0. Fe^{4+} ion substituting a host Ti^{4+} has four valence electrons in the d-shell which are ferromagnetically aligned (Hund's rule). As described above, in the O$_h$ octahedral environment of Fe^{4+}

substitutional impurity in $SrTiO_3$ crystal, the Jahn-Teller (JT) distortion takes place. For the two-fold degenerate e_g mode, there are two symmetrized displacements one of which (q_1) should correspond to inward relaxation of four equatorial oxygen atoms in the xy plane around the iron defect and outward relaxation of the two oxygen atoms along the z axis (see Figure 4.1).

The JT distortion around the Fe^{4+} impurity in $SrTiO_3$ crystal has been quantitatively estimated in Ref.(89) by applying the unrestricted Hartree-Fock (UHF) method within the supercell approach. In that work, careful convergence analysis with the size of supercell was carried out. As a result, 160-atom supercell with one iron ion therein was considered to be large enough to model a single iron impurity, demonstrating quite a small dispersion of defect energy throughout the BZ (0.14 eV). It has been found (89) according to the pattern of the q_1 mode that four Fe–O bonds in the xy-plane shorten by 0.028 Å (inward relaxation) and two Fe–O bonds along the z-axis lengthen by 0.052 Å (outward relaxation) which yields an energy gain of about 1.42 eV with respect to the undistorted geometry. In fact, the resulting distortion is a combination of both q_1 and q_2 normal modes that correctly leads to a slightly less than two ratio of the displacement amplitudes along the z-axis and in the xy-plane. Also, it has been shown that the iron high-spin ($S_z = 2$) state rather than the zero-spin ($S_z = 0$) state is favored with an energy gain of about 5.4 eV (after lattice relaxation). The sketch of the Jahn-Teller distorted FeO_6 octahedra and the splitting of Fe $3d$ energy levels before and after the lattice relaxation are presented in Figure 4.1.

In the present work, we examined the structural and electronic properties of iron impurity for a whole range of iron concentrations x in the $SrFe_xTi_{1-x}O_3$ solid solution based upon the hybrid HF-DFT approach with the B3PW functional. For the most dilute solution under investigation with 270 atoms in supercell, corresponding to the 1.85% iron, we found almost negligible (0.01 eV) dispersion of the iron band within the band gap meaning that the defect-defect interaction
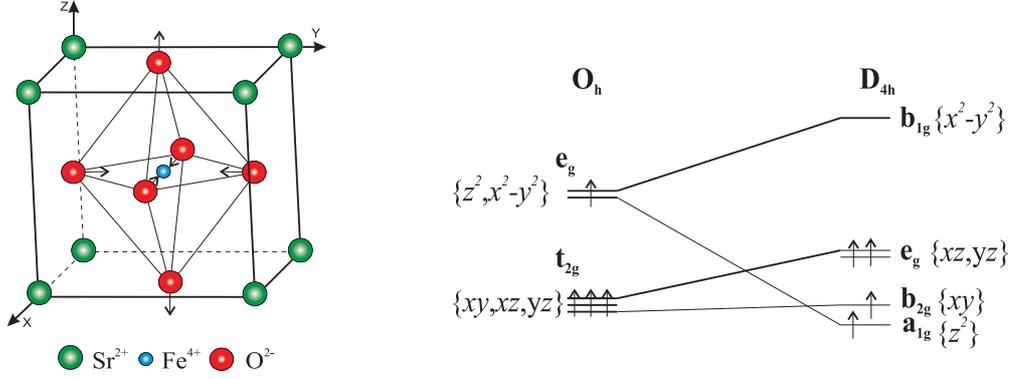
Figure 4.1: Schematic view of the relaxation of six nearest oxygen atoms around Fe^{4+} impurity and the splitting of iron energy levels in cubic (O_h) and tetragonal (D_{4h}) crystalline field symmetries.

between neighboring supercells is practically eliminated. We also demonstrated a strong covalent bonding between unpaired $3d$ electrons of iron impurity and $2p$ electrons of the four nearest oxygen atoms displaced towards the impurity. A more detailed comparative analysis of $SrFe_xTi_{1-x}O_3$ solid solutions is presented in the next section.

In the recent experimental study (34) a strong indication of the presence of the JT distortion around the Fe^{4+} impurity in Fe-doped $SrTiO_3$ crystal has been found. A non-thermal broadening in the Fe–O bond length distribution has been determined which corresponds to a splitting of the bond lengths Δr by about 0.16 Å in the dilute system (x $\rightarrow$ 0). According to the used approach (114), the static disorder component of mean square relative displacement $MSRD_{stat}$ is related to the bond length distribution Δr as follows

$$\sqrt{MSRD_{stat}} = \sqrt{\frac{m(r_m - r_0)^2 + n(r_n - r_0)^2}{m + n}} = \frac{\sqrt{mn}}{m + n}|\Delta r| \qquad (4.1)$$

where $m=4$ and $n=2$ are the numbers of changed bond lengths, r_0, r_m and r_n are the lengths of ideal and two types of distorted bonds, respectively. This

quantity is about 0.006 Å^2 as x $\rightarrow$ 0. The above defined MSRD$_{stat}$ is linked to the standard deviation for changing lengths of chemical bonds and can be used for the comparison between theoretical and experimental results.

Vibrational spectroscopy was also applied in the study of phonon modes in the solid solutions with different iron concentrations and temperatures (34). The hallmark of the measured Raman spectra is a pronounced peak at 690 cm^{-1}. Its position depends only very slightly upon the iron content whereas the intensity increases from $x = 0.003$ up to a maximum at $x = 0.03$ and then decreases. It has been supposed that this characteristic peak is caused by a vibration localized around the Fe^{4+} ion. Based on the MSRD estimates from the EXAFS experiment and on the fact that Raman peak area decreases with increasing iron content, the authors concluded that the JT distortion decreases for high iron concentrations as well. As we will see in the next section, our calculations corroborate this result.

4.2 SrFe$_x$Ti$_{1-x}$O$_3$ solid solutions

The EXAFS study (34) mentioned above has permitted a quantitative estimate of the changes in the Fe–O bond lengths for different iron concentrations in SrFe$_x$Ti$_{1-x}$O$_3$ solid solution based upon the mean square relative displacement (MSRD) approximation (114). A bond length distribution of 0.16 Å corresponding to the JT distortion has been assessed for the dilute defect limit and it has been also revealed that some of the Fe–O bonds contract while the others expand. This experimental estimate can be compared with 0.08 Å which is the sum of 0.052 Å elongation and 0.028 Å contraction obtained in the UHF method (89). It is supposed that the UHF method underestimates the oxygen displacements around the iron, nevertheless, giving the correct picture of the JT distortion and the related electronic structure changes.

Note that in a very recent first-principles plane-wave DFT (LDA and GGA)

study (115) devoted to structural and electronic properties of Fe-doped SrTiO$_3$ and BaTiO$_3$ crystals the Jahn-Teller distortion has not been taken into account in spite of the UHF prediction and the experimental evidence for Fe-doped SrTiO$_3$. As a result, the properties computed there, e.g., iron impurity formation energy, have certainly to be refined.

In this Chapter we describe our first-principles calculation of the Jahn-Teller effect for a whole range of iron content starting from a pure SrTiO$_3$ and ending with a pure SrFeO$_3$ by modeling several characteristic iron concentrations in between. We do not restrict ourselves to isolated iron defects but go beyond this dilute regime towards higher iron concentrations. In order to inspect the tendency of how the total magnitude of the distortion changes for different iron content, we considered 80-, 135-, 160-atom and 270-atom supercells in which titanium atom in the coordinate system origin is substituted by iron atom, thus corresponding to 6.25, 3.70, 3.125 and 1.85 at.% iron concentrations, respectively. In case of 50 at.% iron content we considered two alternative iron configurations with 10-atom and 40-atom supercells.

First of all, we optimized the lattice constant of the cubic SrTiO$_3$ cell which was then used in our simulations of the defective system. It has been demonstrated experimentally (34) that the deviation of the lattice constant in SrFe$_x$Ti$_{1-x}$O$_3$ from that of pure SrTiO$_3$ is expectedly rather small for low iron content. Due to this fact, for the small iron concentrations we performed relaxation of atomic positions with fixed volume using the preliminarily optimized lattice parameter a = 3.892 Å for pure SrTiO$_3$ whereas the Jahn-Teller distortion for 50% iron was calculated with the re-optimized lattice constant of 3.874 Å (for 10-atom supercell).

We carried out full optimization of atomic positions for all supercells chosen. The oxygen displacements found in the first shell of the iron defect clearly indicate that JT distortion takes place according to the D_{4h} point symmetry. In

Table 4.1 we summarize the information on the supercells used and the results for the distorted first oxygen shell around the Fe^{4+} impurity. The results correspond to the optimization using a 2×2×2 **k**-mesh for all supercells, except for 50% iron content where denser meshes were employed. The magnitude of the total geometry distortion $\Delta r = 0.16$ Å estimated from the EXAFS experiment (34) for the dilute limit is comparable with the sum of the elongation of the Fe–O bond along the x- or y-axis and the contraction along the z-axis (see Figure 4.2). For 50% iron content we considered one additional 40-atom supercell with four iron atoms in which defects are arranged in orthogonal –Fe–O–Fe– chains instead of being isolated. In this case the displacements of oxygen atoms exhibit a more complex pattern. While three of four iron atoms in the supercell have four shortened and two elongated Fe–O bonds, the distortion is inverted for the last fourth iron (four elongated and two shortened bonds). In order to compare theory and experiment, we calculated MSRD$_{stat}$ for a whole range of iron concentration according to Equatio 4.1. From the last column of Table 4.1 one can see that MSRD$_{stat}$ increases with lowering the iron content giving the correct tendency of MSRD$_{stat}$ change, known from the EXAFS data, and approaching the experimental estimate for the dilute defect limit.

We also checked the possibility for the JT distortion in pure SrFeO$_3$ in our hybrid HF-DFT computational scheme by performing a full structure optimization starting from the distorted system. The converged geometry has been very close to the perfect cubic structure indicating that JT distortion is unfavorable. This result is consistent with the experimentally observed absence of a JT distortion in pure SrFeO$_3$.

Different spin states for the 80-atom supercell after relaxation were calculated to show that the S$_z$ = 2 state is the most favorable also for the defective system as well as for pure SrFeO$_3$ (see Table 4.2).

In addition, we estimated the formation energy of substitutional iron defect

Table 4.1: The displacements of oxygen atoms in the first shell of the iron impurity for different iron concentrations. Inwards relaxation means displacement towards the iron center. 40-atom supercell with four iron atoms in the cell simulates the orthogonal –Fe–O–Fe– chains while other supercells correspond to the distributions of isolated iron atoms (see the text for explanation). d_{Fe--Fe} denotes the distance between the closest isolated iron defects.

Supercell	Extension	Iron content (%)	d_{Fe--Fe} (Å)	Oxygen displacements (Å)		MSRD$_{stat}$ *10^{-3}, Å^2
				Inward	Outward	
40-atom	$2 \times 2 \times 2$	50.0				2.60
10-atom	$\sqrt{2} \times \sqrt{2} \times \sqrt{2}$	50.0	5.48	0.0489	0.0665	2.96
80-atom	$2\sqrt{2} \times 2\sqrt{2} \times 2\sqrt{2}$	6.25	11.01	0.0545	0.0681	3.34
135-atom	$3 \times 3 \times 3$	3.70	11.68	0.0580	0.0660	3.42
160-atom	$2\sqrt{3} \times 2\sqrt{3} \times 2\sqrt{3}$	3.125	13.48	0.0570	0.0690	3.53
270-atom	$3\sqrt{2} \times 3\sqrt{2} \times 3\sqrt{2}$	1.85	16.51	0.0495	0.0795	3.70[1]

[1]The estimate of MSRD$_{stat}$ from EXAFS experiments extrapolated to the dilute defect limit yields 0.006 Å^2

Ref.((34)).

Table 4.2: Energy differences (in eV) between different magnetic spin states in 80-atom supercell after relaxation with respect to the state with S$_z$ = 2 and energy difference ΔE between unrelaxed and relaxed supercell for S$_z$ = 2.

	S$_z$ = 0	S$_z$ = 1	S$_z$ = 2	S$_z$= 3	ΔE
LCAO-B3PW	6.2	3.5	0.0	2.2	0.40
PW-PBE	0.9	0.4	0.0	1.5	0.46

for all iron concentrations

$$E_{Fe}^{form} = E(def) - E(Fe) + E(Ti) - E(per) \tag{4.2}$$

where $E(Fe)$ [-1263.360313 a.u.] and $E(Ti)$ [-57.983605 a.u.] are the ground state energies of iron and titanium atoms in a gas phase, while $E(def)$ and $E(per)$ are energies for defective and perfect crystals, respectively.

We found that the formation energy of 1.79 eV for the most dilute system under consideration is only by 0.01 eV higher than in 6.25% case. This substitution energy decreases to 1.59 eV for 50% case and to 1.57 eV for a pure SrFeO$_3$.

We also performed the electronic structure calculations for several representative levels of iron doping. Figure 4.2 shows the calculated band structures and the projected density of electronic states (PDOS) for x = 0 (*a*), 6.25 (*b*), 50 (*c*) and 100% (*d*). Figure 4.2 also shows the calculated band structure and the PDOS of a pure SrTiO$_3$. The top of the valence band mainly consists of O $2p$ states while predominantly Ti $3d$ states contribute to the bottom of conduction band. These facts are reflected in our calculation of the band structure and the PDOS in Figure 4.2*a*.

The second limiting case is SrFeO$_3$ which exhibits metallic properties due to zero band gap (Figure 4.2*d*). From the calculated magnetic moments we can conclude that the magnetization is mostly caused by the iron atom (3.79 μ_B) for the ferromagnetic ordering, while the magnetic moments of oxygen atoms induced by the Fe–O bonding are very small (0.07 μ_B). It is clearly seen from

the comparison of the PDOS for spin up and spin down electron densities that the effect of spin polarization is more pronounced for Fe $3d$ states. The PDOS also indicates that a strong mixing between Fe $3d$ and O $2p$ takes place near the Fermi level. Furthermore, the major contribution in the vicinity of the Fermi level originates from the e_g states of iron and the oxygen $2p$ states. These main features of the electronic and magnetic properties of ferromagnetic SrFeO$_3$ agree well with the recent LSDA simulation with plane wave basis set (102).

To study the change of the electronic structure between these two limiting cases of $x = 0$ and $x = 1$, we also calculated the energy bands and PDOS for two levels of iron doping in SrTiO$_3$, namely, 6.25% and 50% iron (Figures 4.2b and 4.2c). For 6.25% (as in the case of pure SrTiO$_3$) the top of valence band is mainly formed by O $2p$ orbitals, and the bottom of virtual bands predominantly consists of Ti $3d$ states. However, there is a noticeable contribution of Fe $3d_{z^2}$ and $3d_{x^2-y^2}$ to the valence band in the pre-Fermi energy region. The spin down electron densities of Fe $3d$ states form narrow sharp bands which are combined into broader peaks in the case of 50% iron (panel c). We can also notice that when going to 50 % iron the Fermi level is moving to slightly higher energy, and that $3d_{z^2}$ and $3d_{x^2-y^2}$ energy bands are merging in the Fermi energy region. These bands are further broadening, as the iron content is increased while the Fermi energy remains nearly the same in the 50%-doped system and in a pure SrFeO$_3$. The same applies to the O $2p$ states when going from 6.25% iron via 50% to a pure SrFeO$_3$. It is also seen that the Ti $3d$ orbitals, still dominating in the bottom of conducting band for the 6.25% of iron, split into two sub-bands and decrease in the 50% case.

The difference electron density map for 80-atom supercell with iron impurity at the center is displayed in Figure 4.3. This density is defined as the total density difference of defective and perfect systems plus the difference between titanium and iron atoms projected onto the (010) plane. The redistribution of the electron
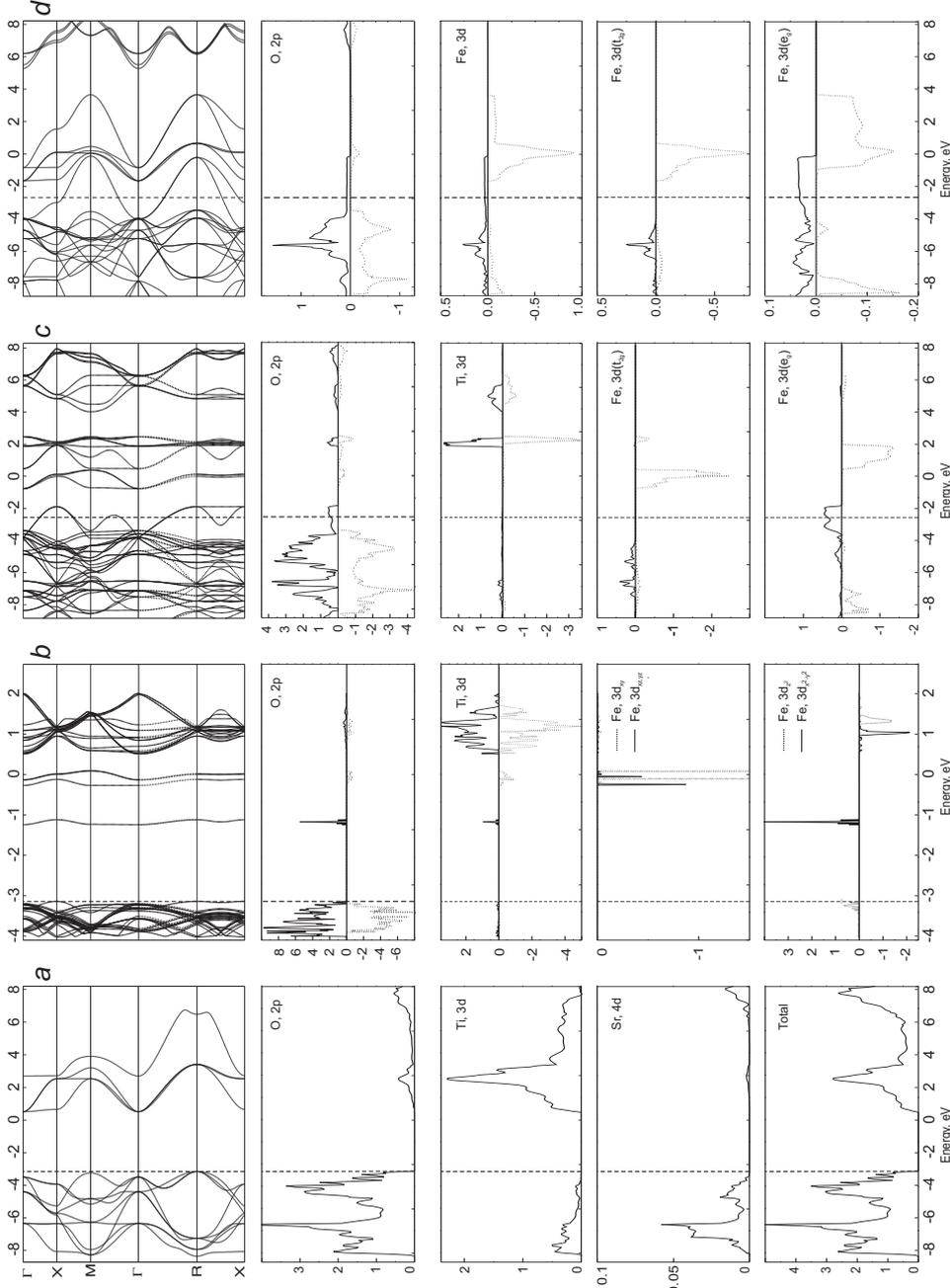
Figure 4.2: Calculated band structures and projected density of electronic states (PDOS) for a) SrTiO$_3$, b) SrFe$_{0.0625}$Ti$_{0.9375}$O$_3$, c) SrFe$_{0.5}$Ti$_{0.5}$O$_3$ and d) SrFeO$_3$. The vertical dash lines denote Fermi energy level. Solid lines are applied to spin up and dot lines to spin down electrons. The values for PDOS are in arbitrary units. In all cases only the top of valence band and the bottom of conduction band are presented.
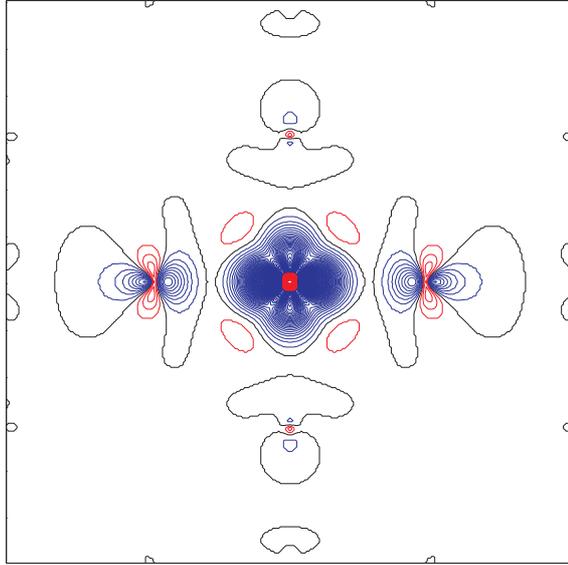
Figure 4.3: Two-dimensional difference electron density map projected onto the (010) plane for 80-atom supercell containing iron defect (at the center) and nearest ions. Black, red and blue solid isolines correspond to the zero, negative and positive values of electron density, respectively. Isodensity curves are drawn from -1.0 to 1.0 e Å^{-3} with increment of 0.01 e Å^{-3}.

Table 4.3: The Mulliken effective atomic charges q in perfect $SrTiO_3$, $SrFeO_3$ and 80-atom supercell with iron impurity. M denotes Ti or Fe atom in bulk crystals and Fe atom in the supercell.

	q(M)	q(O)	
$SrTiO_3$	2.36	-1.41	
$SrFeO_3$	2.26	-1.38	
$SrFe_{0.0625}Ti_{0.9375}O_3$	2.28	-1.39 ($O_{x,y}$)	-1.43 (O_z)

density around the iron impurity demonstrates that iron attracts more electron density than titanium at the same site. This reflects more ionic Ti–O chemical bond in bulk $SrTiO_3$ compared to the Fe–O bond in defective $SrFe_xTi_{1-x}O_3$. The computed atomic magnetic moment of the iron is 3.56 μ_B, being slightly less than in bulk $SrFeO_3$ (3.79 μ_B). These results show that the four unpaired electrons are well localized on the iron atom in bulk $SrFeO_3$.

In Table 4.3 the calculated Mulliken effective charges on atoms are listed. It is seen that the iron charge in $SrFeO_3$ is slightly less than the titanium charge in $SrTiO_3$, thus correctly reflecting slightly more covalent character of $SrFeO_3$ bulk crystal.

4.3 Neutral and charged oxygen vacancies

Properties of oxygen vacancies and their impact on the functionality of semiconductor devices have recently attracted increasing attention (24; 49; 116). This is mainly due to the assumption that oxygen vacancies, particularly in charged states, can serve as intrinsic electron trapping centers, resulting in a reduced carrier mobility, unstable threshold potential and other undesirable features of microelectronic devices.

Bulk properties of a neutral oxygen vacancy in $SrTiO_3$ crystal with two

trapped electrons at the vacancy site, known in oxides as the F center, is relatively well understood owing to a series of mostly DFT studies (26; 27; 28; 33; 117; 118). It has been demonstrated that large supercells are needed for good convergence of the results to the single defect limit. Pure DFT method provides reasonable estimate for the vacancy formation energy, however, it fails to adequately describe the defect energy level in the band gap due to an underestimate of the band gap, thus placing the defect level to the CB. The estimate obtained within the hybrid HF-DFT method for the unrelaxed structures shows that the F center level approaches the CB edge to within ~ 0.5 eV (33). This defect band is mainly composed of $3d_{z^2}$ orbitals of the two nearest Ti ions considerably mixed with the orbitals of electrons centered at the vacancy site. Nevertheless, a more precise placing of the vacancy level into the band gap requires taking into account the important lattice relaxation.

The electronic properties of charged oxygen vacancies in SrTiO$_3$ crystal have received very little attention up to now. In this section, we present a comparative analysis of properties of neutral and singly-charged V$_O$ (F and F^+ centers, respectively) taking into account complete lattice relaxation and considering large enough supercells.

For defect modeling, we exploited a periodic supercell approach (55). For the bulk calculations, we considered two different supercells with 80 and 160 atoms where the latter, as alluded to below, is large enough to substantially reduce the spurious interactions between defects in neighboring cells. Simulations of the charged F^+ center were performed maintaining the neutrality of a cell by replacing a Sr^{2+} ion by a singly charged Rb$^+$ ion close in size. To eliminate the effect of such artificial charge compensator on the calculated F^+ center properties, we placed the Rb$^+$ ion as far as 6.15 Å away from the vacancy and found that further moving it away changes the total energy by less than 0.01 eV in such a high-dielectric material.

Table 4.4: The displacements of atoms (in % of the lattice constant a_0) nearest to the neutral bulk oxygen vacancy (F center) for supercells with 6.25% (80-atom) and 3.125% (160-atom) defect concentration (atomic displacements around the F^+ are given in parentheses). N is the number of symmetrically equivalent atoms in each atomic shell around the vacancy (symmetry decrease for F^+ leads to the shell splitting). Positive sign means outward ionic displacement from a vacancy.

	Unrelaxed					Radial displacements	
Atom	distance	Unrelaxed coordinates			N	80-atom	160-atom
Ti	$a_0/2$	0	0	$a_0/2$	2	-1.21	-0.96 (2.40)
O	$a_0/\sqrt{2}$	$a_0/2$	0	$a_0/2$	8	-1.14	-1.05 (-1.59; -1.57)
		0	$a_0/2$	$a_0/2$			
Sr	$a_0/\sqrt{2}$	$a_0/2$	$a_0/2$	0	4	0.92	0.25 (0.39; 0.43; 0.52)
O	a_0	a_0	0	0	4	0.45	0.37 (0.30; 0.49)
		0	a_0	0			
O	a_0	0	0	a_0	2	0.40	0.58 (-0.36)

First of all, we have carried out a complete atomic structure optimization and determined the displacements of atoms around the two types of oxygen vacancies: neutral and positively charged (Table 4.4). It is seen for the neutral F center that atomic displacements are very small and become even smaller with decreasing oxygen vacancy concentration, thus accounting for small lattice relaxation energies in both supercells ($\sim$0.1 eV). It should be pointed out that our result is in contrast to that obtained within the pure DFT plane-wave calculations (118) where the displacements of the nearest Ti atoms were found considerably larger and in the opposite direction (outwards from a vacancy). This discrepancy is not surprising in light of the different electronic structure of the F center predicted by the two methods: The hybrid exchange-correlation functional method models the classical neutral F center with two electrons well localized inside the vacancy, whereas a pure DFT method tends to largely delocalize the electron density, thus leading to a positively charged vacancy (with energy level in the CB), which obviously has a repulsive interaction with two surrounding Ti cations. The relaxation around the F^+ center differs considerably from that of the F center (Table 4.4) and the nearest Ti atoms are displaced outwards.

The band structure calculations indicate that the incorporation of the oxygen vacancy does not significantly affect the band gap of the crystal and induces one-electron defect band within the band gap as illustrated in Figure 4.4 for the neutral F center .

The main characteristics of one-electron energy levels for both types of vacancies are summarized in Table 4.5. As one can see, defect levels of both bulk F and F^+ centers lie well below the CB bottom. One can recognize a noticeable difference in the defect level position, namely, that the singly-charged vacancy level lies $\sim$0.44 eV deeper than that of the neutral vacancy. This observation is in line with the Green function method prediction for $SrTiO_3$ (117) and the first-principles calculation results obtained for other transition metal oxides (116). The
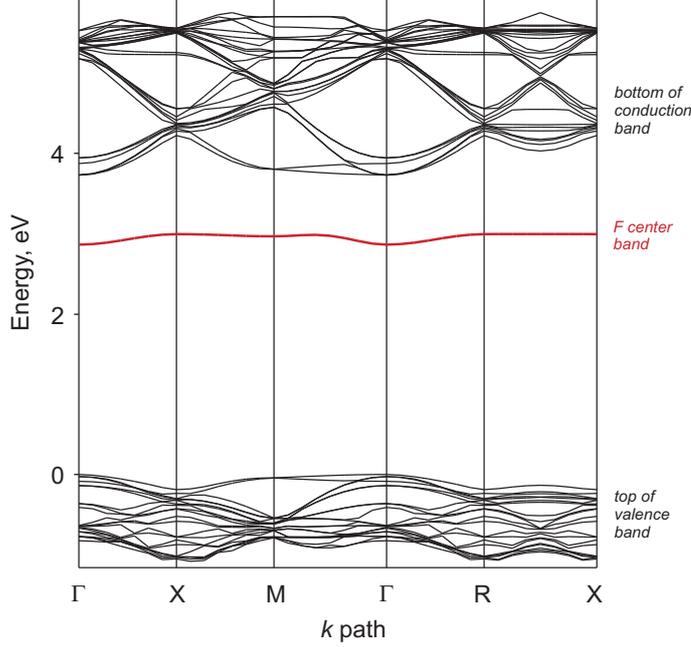
Figure 4.4: The band structure of the relaxed $SrTiO_3$ crystal with a single neutral F center enclosed in 80-atom supercell.

dispersions of the defect bands ($\delta\varepsilon_{db}$) throughout the BZ are particularly small for 160-atom cell, reflecting the fact that the corresponding wave functions are well localized within the supercell and thus yielding a weak interaction between oxygen vacancy replicas in neighboring supercells.

Regarding the defect levels, it should be pointed out here that there are two types of experimentally measurable transition levels. Optical transition between two states corresponds to the Franck-Condon-type excitation (a vertical transition). Hence, it is observed in experiments that the final excited state does not relax to its equilibrium configuration during the transition. Second type is a thermodynamical multiphonon transition (thermal ionization) that is accompanied by the atomic structure relaxation to its equilibrium configuration and can be probed by, e.g., deep-level transient spectroscopy for deep defects or temperature-dependent Hall experiments for shallow defects (119).

Table 4.5: Calculated defect energy level $\Delta\varepsilon^{\Gamma}{}_{db}$ (eV) with respect to the bottom of conduction band at the Γ point of the Brillouin zone, its dispersion $\delta\varepsilon_{db}$ (eV), the Mulliken charge q (e) of the vacancy and the formation energies E_{form} (eV) of the bulk F and F^+ centres (relative to atomic oxygen), d_{F-F} denotes the distance between periodically repeated defects (Å).

Supercell	d_{F-F}	Relaxation	$\Delta\varepsilon^{\Gamma}{}_{db}$	$\delta\varepsilon_{db}$	q	E_{form}
80-atom (F)	11.01	unrelaxed	0.84	0.13	1.28	9.17
		relaxed	0.79	0.13	1.26	9.07
160-atom (F)	13.48	unrelaxed	0.75	0.06	1.28	9.17
		relaxed	0.77	0.06	1.26	9.06
160-atom (F^+)	13.48	relaxed	1.20	0.05	0.82	8.41

The Mulliken population analysis indicates that an electron charge of about $\sim$1.3 $|e|$ is localized at the vacancy site while the residual 0.7 $|e|$ of the missing O^{2-} ion is equally distributed among the two Ti ions nearest to the neutral F center.

4.4 Diffusion of oxygen vacancy

Bulk diffusion of oxygen atoms is the most basic step in solid state transport process. To address this issue, we have applied the DFT plane wave formalism combined with the NEB method for searching transition states. For all the NEB calculations we have used a plane wave cutoff energy of 400 eV. Bulk diffusion was modeled considering 80-atom supercell with one neutral oxygen vacancy created.

Simulation of bulk diffusion in $SrTiO_3$ crystal is rather simple due to the presence of mirror plane right in the middle of diffusion path. In order to find the diffusion barrier, the energy profiles for oxygen vacancy migration were mapped out by calculating the energy of the migrating vacancy along the diffusion path
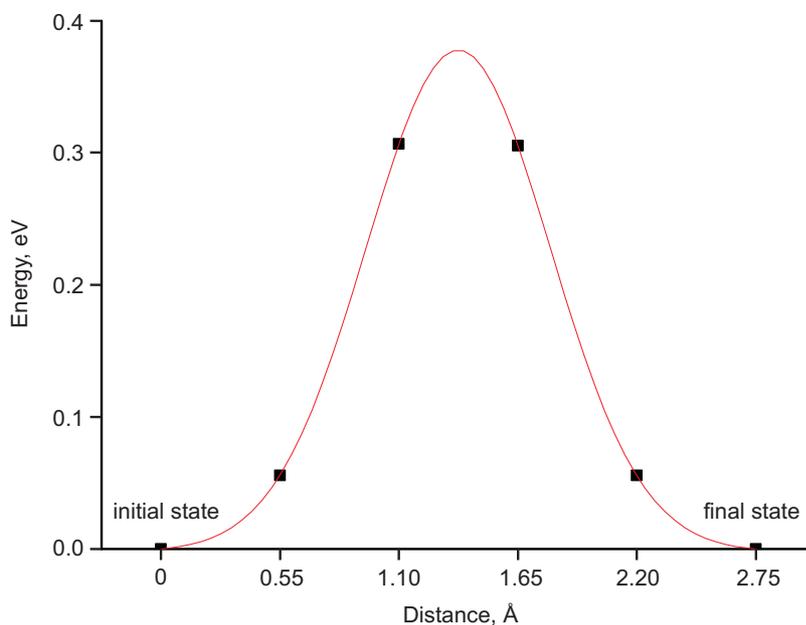
Figure 4.5: Calculated energy profile for the diffusion path of oxygen vacancy in SrTiO$_3$ bulk.

consisting of four equidistant intermediate states (images) between the initial and final state. This results in a symmetrical activation barrier with the saddle point in the middle of the path (Figure 4.5). That is why the value of activation barrier obtained with the NEB method (0.38 eV) can be in this case compared with the single-point calculation in which oxygen atom is placed at the middle-path point where its displacement during optimization is only allowed within the mirror plane.

It should be noted that the experimental estimate for the barrier of oxygen diffusion in SrTiO$_3$ is 0.86 eV (120), being twice higher than the calculated value. One of the reasons for such a discrepancy is the common underestimate of activation barrier in pure DFT method applied. Nevertheless, it is believed that the relative characteristics such as, e.g., the difference between bulk and surface oxygen diffusion barriers are reproduced correctly.

4.5 Iron impurity and oxygen vacancy clustering

The interaction between ionic point defects is of significance in understanding the defect chemistry in a material since it can lead to the formation of defect complexes, changing the effective concentration of species, and therefore it must be taken into account in the defect chemical model. In the case of oxygen deficient Fe-doped $SrTiO_3$ crystal, it has been shown by the electron paramagnetic resonance (EPR) technique that there is a perceptible attraction between iron impurity and oxygen vacancies yielding Fe^{3+}–V_O complexes even at dopant concentration below 0.1 at.%, while such defect pairs are completely dissociated at temperatures above 300°C (121). Clustering in higher-order complexes such as Fe^{3+}–V_O–Fe^{3+} has not been investigated in that study.

From the electronic point of view, the binding of iron impurity and oxygen vacancies should give rise to a modified electronic structure of the defects with respect to the noninteracting species. Thus, the properties of a single oxygen vacancy as an effective trapping center can be changed. As a matter of fact, it has been experimentally demonstrated that acceptor doping of $SrTiO_3$ crystal with Fe^{3+} or Cr^{3+} as substitutional impurities at Ti^{4+} site can be used for the control of leakage current caused by the presence of oxygen vacancies (43). It is expected that the acceptors electrically compensate donor species such as oxygen vacancies, thereby reducing the concentration of mobile carriers that contribute to electrical conductivity. By tuning dopant concentration, it is possible to achieve a high leakage resistance of the material which is, in practice, a measure of electrical "health" of integrated circuit systems including dynamic random access memory capacitors.

Recently, defect association processes in perovskite-structured ionic conductors have been addressed by means of a number of atomistic and first-principles

approaches (122; 123; 124; 125). Particular emphasis was laid on the calculation of binding energies for different possible types of defect clusters. The obtained information should assist in constructing the correct defect models to rationalize the observed conductivity data.

In this Section, we examine the neutral Fe^{3+}–V_O–Fe^{3+} defect complex with a focus on the energetics of such clustering and on its electronic structure. To this end, we have chosen the 80-atom supercell. Using the results of our previous calculations of a single iron impurity and neutral oxygen vacancy in the same supercell allowed us to estimate the binding energy for the triple-defect complex which is 0.97 eV. A previous benchmark-type atomistic simulation on the incorporation of a range of transition metal dopants into the $BaTiO_3$ crystal lattice demonstrated that the dopants prefer to substitute the Ti^{4+} ion with oxygen-vacancy compensation (122). It was also revealed that for linear clusters of the type $A^{'}$–V_O–$A^{'}$ the binding energy is additive quantity meaning that it is almost twice larger than that of the corresponding defect pair and thus no extra stabilization is provided by adding second impurity to the vacancy site. It has been found that the defect pair association energy for trivalent ions such as Fe^{3+}, Co^{3+} or Ni^{3+} with oxygen vacancy is about 0.4 eV what is consistent with our finding.

The band structure calculation (Figure 4.6) combined with the analysis of the projected density of electronic states shows that the oxygen vacancy energy level, forming quite a shallow energy band within the band gap (0.79 eV below the CB edge) in the case of an isolated vacancy, is now pinned due to the mixing with the Fe $3d_{z^2}$ orbitals and gets very far from the bottom of the CB. The Mulliken population analysis indicates that iron ions much more effectively attract the electron density from the vacancy site as compared to titanium ions, thus becoming Fe^{3+} ions and leading to the doubly charged oxygen vacancy in between two iron ions. To illustrate the spin density redistribution in the vicinity of the complex,
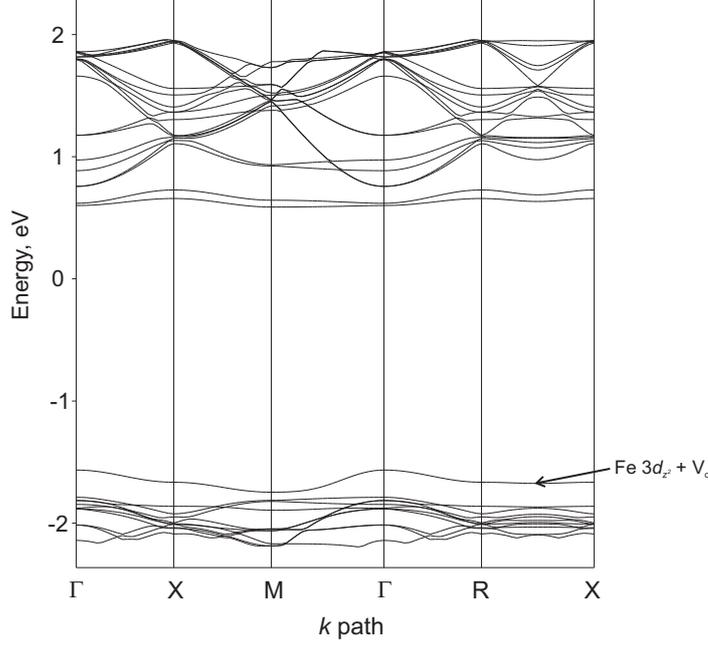
Figure 4.6: The band structure of the relaxed $SrTiO_3$ crystal containing a Fe^{3+}–V_O–Fe^{3+} defect complex in 80-atom supercell (α spin electrons).

we plotted two-dimensional spin density map (Figure 4.7) that demonstrates a strong spin localization on the both Fe atoms and only a very slight spin polarization is introduced on the closest oxygen atoms, while negligible spin density is observed at the vacancy site.

4.6 Conclusion

To summarize the results on point defects in $SrTiO_3$ bulk crystal, we have considered substitutional iron impurities and oxygen vacancies (neutral and charged) as common imperfections in ABO_3-type perovskites. Examination of iron doping in a whole range of dopant concentration has shown that the magnitude of the Jahn-Teller distortion around an Fe^{4+} center in terms of mean square relative displacement is the largest for the most dilute solution (1.85 at.%), decreases

for higher iron contents and vanishes in a pure $SrFeO_3$. These results quantitatively and qualitatively agree with the EXAFS data. The electronic structure calculations indicate that solutions with at least 50% iron are metallic, and their conductivity is caused by a strong mixing of O $2p$ and Fe $3d$ (e_g) states in the pre-Fermi energy region. The defect formation energy computed for the bulk is compared in the next Chapter with the case of surface defect to find out the segregation energy.

Regarding the oxygen vacancies, we have found that the F^+ center has a deeper energy level than the neutral F center revealing also a lower vacancy formation energy. The charged nature of the center results in a more pronounced relaxation around the defect with a repulsive interaction with neighboring titanium atoms. Simulation of the bulk diffusion process has allowed us to estimate the activation barrier and this will be compared with the dynamics of oxygen species at the surface.
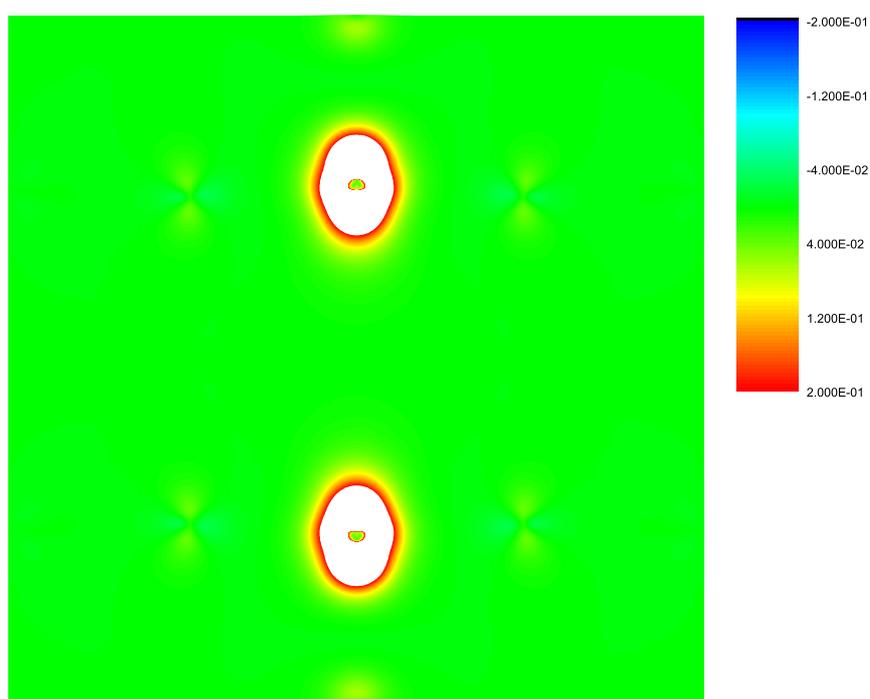
Figure 4.7: Two-dimensional spin density map projected onto the (010) plane for 80-atom supercell containing Fe^{3+}–V_O–Fe^{3+} complex (vertically shown at the plot). The density is drawn from -0.2 to 0.2 e Å^{-3}.

Chapter 5

Defects at the SrTiO$_3$ (001) surface

In this Chapter we report on modeling of iron impurity and oxygen vacancy at the SrTiO$_3$ (001) surface with different (SrO and TiO$_2$) terminations. Our emphasis is placed on the defect segregation energies, structural changes in the near-surface region, changes in the electronic properties and chemical behavior of surfaces induced by segregation of point defects. We also explore the adsorption of atomic oxygen on surfaces, diffusion of oxygen vacancy along the TiO$_2$ surface and a drop of the adsorbed oxygen atom into the nearby vacancy.

5.1   Fe^{4+} iron impurity

Segregation of point defects from the bulk to the surface is one of the most important reasons that leads to space-charge effects, changing the composition of the near-surface region and modifying the properties of pristine surfaces. Although first theoretical explanations for surface segregation date back to Gibbs in the 19th century ([126](#)), only in the past few decades experimental techniques have achieved sufficient resolution to examine this phenomenon at the atomic level

(127; 128). Over the last years, a large number of studies have addressed the influence of defect segregation on surface properties, in view of various practical applications including sensing and catalysis (36; 129; 130). In addition to advanced experimental methods, the developed computer modeling techniques become particularly fruitful to complement experimental data and provide new insight into the processes of defect segregation to surfaces (131; 132).

Also, the results obtained for defective surfaces could be used for understanding the behavior of interfaces with defects. These play an enormous role in polycrystalline electroceramics such as Fe-doped SrTiO$_3$ material (39; 133; 134; 135). Defect segregation to the grain boundaries (GB) of polycrystalline materials serves as a key constituent of space-charge effects affecting the GB properties. For instance, the potential barrier at the GB region affects both the electronic and ionic transport across the GB.

It should be pointed out that generally a number of possible contributions to the segregation driving force can play a role (136; 137). It includes different defect formation energies in the bulk and on the surfaces, elastic strain energy due to lattice distortion around a defect, the effect of ambient atmosphere, interaction between the defects and others. In our study here, we concentrate on the calculation of the difference in formation energies between bulk and surface defects for fully relaxed defective structures. We also use large enough surface cells, approaching a coverage corresponding to almost non-interacting surface defects.

Our simulations of the iron substitutional defect on the SrTiO$_3$ (001) surfaces were carried out on two slabs containing seven stacking atomic layers and terminated by either SrO or TiO$_2$ planes. These slabs are non-stoichiometric but symmetrical, thereby allowing us to benefit from the presence of mirror plane in the middle of a slab. The interaction between defects on the opposite sides of a slab is eliminated using thick enough slabs. The results obtained with eleven-layer slab do not significantly change the conslusions. In Figure 5.1 three upper

74

layers of SrO- (a) and TiO$_2$-terminated (b) iron-doped surfaces are displayed. It should be pointed out that the incorporation of the surface defect does not change the primary pattern of the atomic displacements known from the calculation of the relaxed defect-free (001) surfaces (12; 118). As has been revealed in these calculations, the most displaced atoms are surface (for SrO termination) and sub-surface (for TiO$_2$ termination) Sr atoms which relax inwards and outwards the slab center, respectively. Their displacements are by several times larger than those for other atoms. However, the incorporation of iron impurity induces also the atomic displacements not only in the vertical direction: the oxygen displacements found in the first atomic shell of the surface iron defect are listed in Table 5.1 and schematically shown in Figure 5.1.
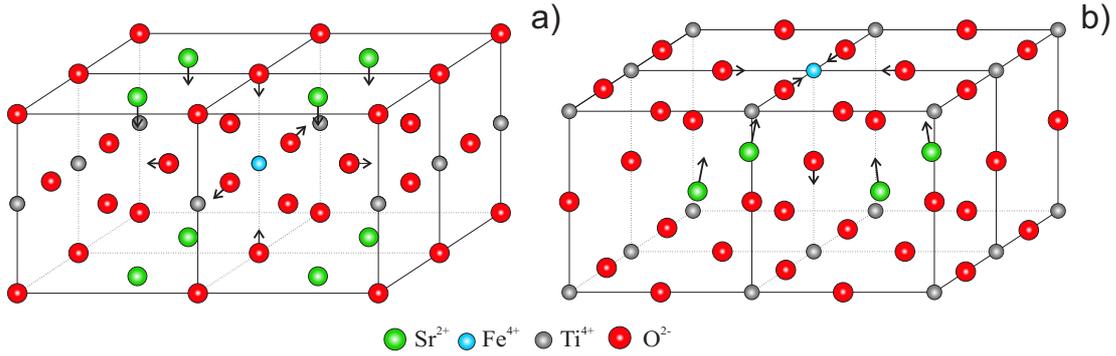

Figure 5.1: Three upper atomic layers of SrO- (a) and TiO$_2$-terminated (b) surfaces with the iron defect. Only the directions of displacements for the most relaxed strontium atoms and the nearest to the iron defects oxygen atoms are schematically indicated.

In this table we also present Fe impurity formation energies computed in the same manner as for the bulk crystal. From a comparison of bulk and surface values, one can conclude that there is a perceptible driving force for iron impurities to segregate to both SrO and TiO$_2$ surfaces, with a slight energy preference in

Table 5.1: The displacements of oxygen atoms in the first atomic shell of the Fe^{4+} impurity for different iron concentrations C_{Fe}. Inward relaxation means displacement towards the iron defect. E$_f$ is the iron formation energy (the bulk value for the iron content between 6.25 and 1.85% is 1.78 - 1.79 eV).

				Oxygen shifts (Å)		
Cell extension	Termination	C_{Fe} (%)	d (Å)	Inward	Outward	E$_f$ (eV)
2×2	SrO	25.0	7.78	0.0778[1]	0.0090	1.47
				0.0370[2]		
	TiO$_2$			0.0569	0.0188	1.40
3×3	SrO	11.1	11.68	0.0788[1]	0.0092	1.47
				0.0395[2]		
	TiO$_2$			0.0673	0.0451	1.31

[1]Oxygen atom in the upper plane.

[2]Oxygen atom in the third plane.

the latter case (0.32 and 0.48 eV, respectively).

It is interesting to compare the calculated Mulliken atomic charges for perfect and defective surfaces reported in Table 5.2. As known from the simulations of bare and water-covered nondefective SrTiO$_3$ (001) surfaces (13; 118), SrO-terminated surface reveals the more basic nature of the top oxygen atoms making the dissociative type of water adsorption on SrO-terminated surface more probable than on the TiO$_2$-terminated one. This is clearly reflected here by the oxygen charges on both surfaces being more negative for SrO plane. However, the iron substituting titanium in the second layer significantly reduces the atomic charge of the top oxygen, what, in turn, should lead to less basic properties of SrO-terminated surface in the iron-doped material.

Table 5.2: The Mulliken effective atomic charges (in e) for the undoped and doped (001) surfaces.

Termination	Plane	Doped surface		Undoped surface	
		Ion	Charge	Ion	Charge
SrO	1	Sr	1.85	Sr	1.85
		O	-1.36	O	-1.52
	2	Fe	2.28	Ti	2.37
		O	-1.47	O	-1.44
TiO$_2$	1	Fe	2.22	Ti	2.29
		O	-1.29	O	-1.30
	2	Sr	1.85	Sr	1.85
		O	-1.44	O	-1.37

5.2 Oxygen vacancies

The oxygen vacancies on SrTiO$_3$ surfaces have a great influence on a variety of properties. For instance, oxygen vacancies are often implied to be responsible for processes of surface reconstruction (17; 138). It was suggested, based upon ultraviolet photoelectron spectroscopy data, that the creation of oxygen vacancies near and on the surfaces may result in a shallow occupied defect level below the CB edge and thus assist in increasing the electronic conductivity (19; 139).

There were only few attempts to carry out a computational study of surface properties in the presence of oxygen vacancies (33; 140; 141) which either did not take into account important surface relaxation (33; 140) or used only primitive surface cells (141). Here we present the results obtained for both neutral and positively-charged surface oxygen vacancies (F and F^+ centers). We use large surface cells and the hybrid HF-DFT method suited for a correct description of the single-defect energy levels within the band gap for the fully relaxed oxygen-

Table 5.3: Displacements of atoms nearest to the surface F centre (% of a_0): N is the number of symmetrically equivalent atoms in each shell around the vacancy and M is the modulus of the displacements.

SrO termination						TiO$_2$ termination					
Atom	N	Δx	Δy	Δz	M	Atom	N	Δx	Δy	Δz	M
Ti	1	0.00	0.00	0.74	0.74	Ti	2	-0.52	-1.92	-3.24	3.80
Sr	4	0.58	0.58	-4.72	4.76	O	2	2.50	2.18	-0.28	3.33
O	4	-0.17	0.00	2.70	2.71	Sr	1	0.00	-0.03	0.62	0.62
O	4	0.00	1.87	1.12	2.18	O	2	1.06	0.34	-0.45	1.20
O	1	0.00	0.00	-0.28	0.28	Sr	1	0.00	-0.22	0.74	0.77
Ti	4	0.00	0.24	1.75	1.77	O	2	1.18	1.21	-0.47	1.75

vacancy surfaces with SrO and TiO$_2$ facets. To model the surface F center, we used symmetrical seven-layer slabs with SrO and TiO$_2$ terminations with the two oxygen vacancies on the opposite surfaces, whereas for the F^+ center we considered an asymmetrical six-layer slab in order to avoid non-negligible interactions between the charged defects on opposite slab sides.

The results of structural optimization for the neutral oxygen vacancy are summarized in Table 5.3. One can see that the atomic displacements exhibit a more complex pattern than for the bulk, due to the combination of both defect incorporation and surface relaxation. This results in a larger perturbation area which spreads over several coordination spheres. It is also seen that surface Sr ions are still the most displaced species for the SrO facet as it is for the defect-free surface. In the case of TiO$_2$ termination, the displacement of Ti atoms neighboring the vacancy become even larger than for Sr atoms. Generally, the relaxation of atoms nearby the charged oxygen vacancy is more pronounced.

The calculated defect formation energies of the surface vacancies (Table 5.4)

Table 5.4: Calculated defect energy level $\Delta\varepsilon^{\Gamma}{}_{db}$ (eV) with respect to the bottom of conduction band at the Γ point of the Brillouin zone, its dispersion $\delta\varepsilon_{db}$ (eV) and the formation energies E_{form} (eV) of the bulk F and F^+ centres relative to atomic oxygen (see explanation in the text). The distance between periodically repeated defects is 11.7 Å.

Defect	Surface	$\Delta\varepsilon^{\Gamma}{}_{db}$	$\delta\varepsilon_{db}$	E_{form}
F centre	SrO	0.27	0.02	8.04
	TiO$_2$	very shallow	-	7.62
F^+ centre	SrO	1.19	0.02	6.16
	TiO$_2$	0.81	0.002	4.87

are considerably smaller than in the bulk. It points at a strong propensity of the oxygen vacancies for a segregation from the bulk to the surfaces. This is consistent with previous DFT predictions obtained for a $\sum 3(111)[10\bar{1}]$ grain boundary in SrTiO$_3$ (142), as well as for other perovskites (22).

Regarding the electronic properties, the surface F center turns out to be a much more shallow defect than that in the bulk, however, this depends largely on the surface termination. Thus, for the TiO$_2$ surface, the defect level of the F center nearly degenerates the conduction band bottom and the surface becomes practically metallic. This is accompanied by a considerable electron density delocalization from the vacancy over the nearest ions.

The surface F^+ center is a deeper defect than the surface neutral vacancy, similarly to the situation in the bulk. Due to the known high covalency of Ti-O chemical bond, especially at the surface, the electron density of the charged vacancy is well spread over the nearest Ti atoms resulting in a mixed character of the defect band level. These results are fairly consistent with the conclusions drawn from ultraviolet-photoemission spectroscopy measurements on reduced SrTiO$_3$

(001) surfaces ([139](#)) indicating the coexistence of both quite deep (1.2 eV below the bottom of the CB) and shallow levels due to surface oxygen vacancies.

5.3 Atomic oxygen adsorption

Here we examine the atomic oxygen adsorption on SrO and TiO$_2$ facets considering different possible surface adsorption sites as illustrated in Figure [5.2](#). This part should help us in understanding the surface oxygen kinetics. Despite the use of pure DFT plane wave methodology for the study of the overall oxygen kinetics in SrTiO$_3$ crystal, in this section we critically compare our results with those obtained within the hybrid HF-DFT LCAO method with the B3PW functional ([143](#)). We should note at the outset that the main conclusions drawn from both approaches are the same.
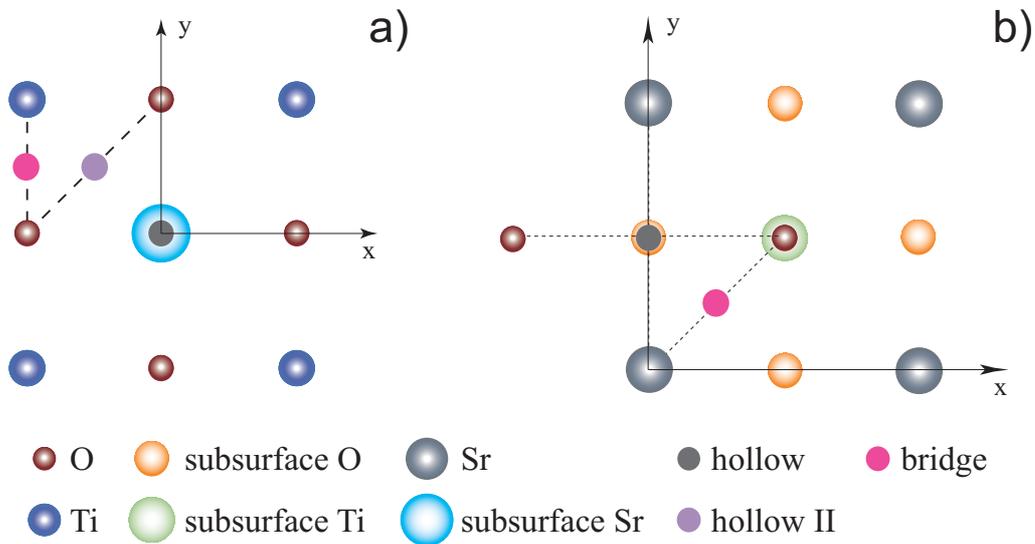

Figure 5.2: Top views of a) TiO$_2$- and b) SrO-terminated surfaces with the possible positions for oxygen adsorption.

Table 5.5: Calculated adsorption energies (in eV) in pure DFT plane wave method with the PBE functional (PW-PBE, VASP code) and in the hybrid HF-DFT LCAO method with the B3PW functional (LCAO-B3PW, CRYSTAL code) (143). The adsorbed oxygen atom at the hollow sites was considered in the triplet state as a more favorable electronic configuration.

Site	PW-PBE	LCAO-B3PW	Site	PW-PBE	LCAO-B3PW
		TiO_2 termination		SrO termination	
Ti	2.13	-	Sr	0.57	-
O	2.51	1.76	O	2.44	1.54
bridge	2.96	2.03	bridge	3.06	2.43
hollow II	0.12	0.93	hollow	1.73	1.08

Table 5.6: Distances (in Å) between the adsorbed oxygen atom and the nearest surface O and Ti (or Sr) atoms for optimized adsorption structures of $SrTiO_3$ (001) substrates.

Site	PW-PBE		LCAO-B3PW	
	O_{surf}	$Ti(Sr)_{surf}$	O_{surf}	$Ti(Sr)_{surf}$
		TiO_2 termination		
Ti	2.45	1.65	-	-
O	1.45	2.31	1.46	2.76
bridge	1.46	1.56	1.47	1.91
hollow II	2.43	3.18	2.24	2.00
		SrO termination		
Sr	3.32	2.33	-	-
O	1.47	2.85	1.47	3.24
bridge	1.49	2.09	1.50	2.45
hollow	2.62	2.47	2.48	2.53

Table 5.7: Effective atomic charges in e (Bader analysis in PW-PBE and Mulliken analysis in LCAO-B3PW) for the adsorbed oxygen atom and the nearest surface O and Ti (or Sr) atoms for optimized adsorption structures of SrTiO$_3$ (001) substrates. Atomic charges at the pristine surface layer – PW-PBE: Ti 2.03, O -0.84 (TiO$_2$ termination); Sr 1.56, O -0.72 (SrO termination); LCAO-B3PW: Ti 2.31, O -1.32; Sr 1.84, O -1.52.

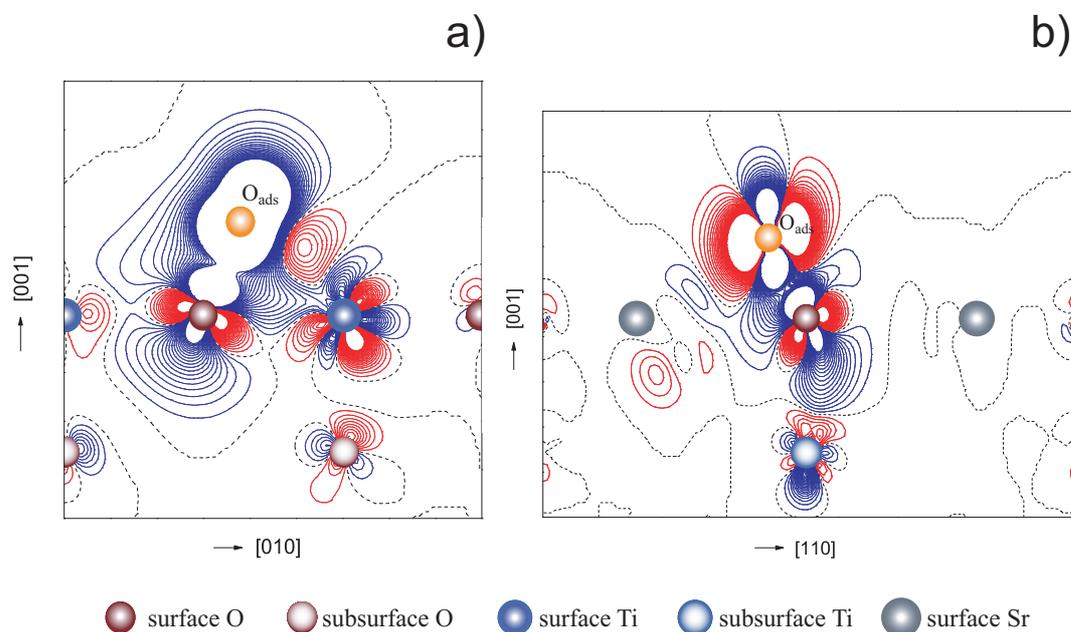| Site	PW-PBE			LCAO-B3PW		
	O_{ads}	O_{surf}	$Ti(Sr)_{surf}$	O_{ads}	O_{surf}	$Ti(Sr)_{surf}$
	TiO$_2$ termination					
Ti	-1.24	-0.89	2.03	-	-	-
O	-1.39	-1.31	2.05	-0.62	-0.77	2.29
bridge	-1.51	−1.29	2.13	-0.52	-0.79	2.28
hollow II	-1.77	-0.87	2.02	-0.29	-1.16	2.29
	SrO termination					
Sr	-1.24	-0.89	2.03	-	-	-
O	-1.24	-0.89	2.03	-0.71	-0.90	1.86
bridge	-1.29	-1.18	1.56	-0.84	-0.88	1.85
hollow	-1.28	-0.88	1.59	-0.52	-1.32	1.86

Figure 5.3: Two-dimensional difference electron density maps for O_{ads} over bridge site at a) TiO_2- and b) SrO-terminated surfaces. Black, red and blue isolines correspond to the zero, positive and negative values of electron density, respectively (143).

Table 5.5 comprises the calculated adsorption energies for all the surface sites under consideration. One can clearly see that the most favorable configurations of oxygen adsorption on both substrate surfaces are bridge position and position atop of the surface oxygen atom. The analysis of the interatomic distances (Table 5.6) indicates that for the bridge position on both facets the adatom is substantially shifted towards the nearest surface oxygen atom. A further analysis of these two most favorable adsorption structures by means of effective atomic charges (Bader and Mulliken approaches, Table 5.7) along with the electron density maps (Figure 5.3) points at the formation of pseudomolecular tilted species O_{ads}–O_{surf} for both surface terminations. The redistribution of electron density

in the vicinity of the adsorbed oxygen atom (Figure 5.3) was obtained within the hybrid HF-DFT method, while it is known that the pure DFT approach commonly overestimates the covalent contribution to the chemical bonding. This also explains generally larger adsorption energies evaluated within the pure DFT method. Nevertheless, both methods lead to the same conclusions about the atomic oxygen adsorption on the surfaces of SrTiO$_3$ crystal. Specifically, (i) there is a quite strong bonding O$_{ads}$–O$_{surf}$ with the highest adsorption energy for the bridge oxygen position; (ii) O$_{ads}$ is bound stronger on the more ionic SrO surface than on the TiO$_2$ termination; (ii) the diffusion of atomic oxygen along the surfaces is expected to have relatively high activation energies and expected to be quite anisotropic (along Ti–O–Ti chains on the TiO$_2$ facet and along Sr–O–Sr chains on the SrO facet). We should note that these predictions are also consistent with a recent DFT-based VASP study of LaMnO$_3$ (001) surfaces (144).

5.4 Diffusion of oxygen species

Using the DFT plane wave VASP calculations combined with the nudged elastic band method (NEB), we have investigated oxygen atomic adsorption and diffusion of oxygen vacancies on the SrTiO$_3$ (001) surfaces. Surface dynamics of oxygen species is of great significance as it affects transport, chemical and photochemical processes relevant for the SrTiO$_3$ applications such as solid oxide fuel cells, oxygen sensing and catalysis (25). Recently, the investigations of transport properties and diffusion barriers for surfaces of transition metal oxides on *ab initio* level become available (145).

We exploited here the symmetrical seven-layer slab model (SrO or TiO$_2$-terminated) with a large separation of 19.5 Å between periodically repeated slabs (vacuum gap). We have chosen a surface unit cell as the extended $2\sqrt{2} \times 2\sqrt{2}$ primitive unit cell which corresponds to 12.5% surface defect coverage. For the

summation in the BZ, we employed a $2\times2\times1$ Monkhorst-Pack mesh of k points.

The main focus was on activation energy barrier for the two elementary steps of surface oxygen transport. The first one is the diffusion of oxygen vacancy along the topmost TiO_2 (001) surface. This step is analogous to the bulk vacancy migration. Due to the mirror plane across the diffusion path, it should lead to a symmetrical barrier. The value of the barrier is expected to be lower than for the bulk because of decrease in the coordination number for surface atoms. Our calculations show that the barrier is indeed $\sim$0.14 eV, being almost by a factor three lower than that in the bulk (0.38 eV). Thus, we predict *highly mobile surface oxygen vacancies* as compared to the bulk.

The second diffusion step of our interest here is the penetration of the adsorbed oxygen atom into the nearby surface oxygen vacancy. First of all, we found that the adsorption energy of O atom atop the Ti ion is $\sim$2.13 eV, being much larger than, for example, for O atom atop the Sr ion (0.57 eV). Moreover, the presence of oxygen vacancy nearby the adsorbed oxygen atom gives rise to a much higher O_{ads}-Ti binding energy.

In previous section we have investigated the atomic oxygen adsorption for different possible surface sites and found high adsorption energies, in particular, for bridge position of oxygen adsorbed (2.96 eV for TiO_2 facet) and atop of surface oxygen atom (2.51 eV for TiO_2 facet). Such a strong binding leads to a stabilization of structure with surface-bound oxygen atom rather than its diffusion along the surface. Simulation of a drop of the adsorbed oxygen atom into the closest oxygen vacancy reveals a distinguishable but extremely small activation barrier, just $\sim$0.01 eV. Hence, we predict almost no-barrier soaking of the adsorbed O atom into the nearby vacancy that occurs when strongly-bound oxygen meets the very mobile surface oxygen vacancy. This is similar to the case of dynamics of oxygen species in $LaMnO_3$ (144).

5.5   Conclusion

Summing up this Chapter, we have studied Fe^{4+} impurity at the subsurface layer of SrO facet and right at the TiO_2 surface. We have found that the impurity has a driving force to surface segregation with a slight preference in the case of TiO_2 facet. Also, the presence of Fe^{4+} ion in the subsurface plane significantly reduces the charge of the nearest oxygen atom at the topmost SrO surface (compared to the substituted Ti^{4+}), thereby severely diminishing its basic properties. The covalent character of the M–O (M = Fe, Ti) bond is increased at the surfaces with respect to the bulk. These are important for the chemical behavior of defective surfaces.

A comparative analysis of the atomic, electronic and energetic properties of the F and F^+ centers on the $SrTiO_3$ (001) surfaces shows that the charged oxygen vacancy reveals a stronger local lattice relaxation, a deeper one-electron energy level and considerably stronger propensity for the surface segregation. Generally, both oxygen vacancies have far larger segregation energies than the Fe impurity. A common feature of both types of vacancies is more shallow energy levels when being on the surfaces than in bulk, particularly for the TiO_2 facet; however, the effect is less pronounced for the charged oxygen vacancy.

We have examined the adsoption of atomic oxygen on the $SrTiO_3$ surface and found: (i) there is a quite strong bonding O_{ads}–O_{surf} with the highest adsorption energy for the bridge oxygen position; (ii) O_{ads} is bound stronger on the more ionic SrO surface than on the TiO_2 termination; (ii) the diffusion of atomic oxygen along the surfaces is expected to have relatively high activation energies and to be quite anisotropic. As to diffusion of the oxygen species, we predict almost no-barrier soaking of the adsorbed O atom into the nearby vacancy that occurs when strongly-bound oxygen meets the very mobile surface oxygen vacancy.

Chapter 6

Confinement effects on oxygen vacancies

Here we aim to explore the confinement effects on the oxygen vacancies as representative ionic carriers in transition metal oxides. To this end, we study the F and F^+ centers placed into the $SrTiO_3$ ultrathin films and investigate their properties as compared to the bulk.

One of the primary issues related to nanometer-sized materials is how properties depend on a system size and whether there is a critical size for a given property. The size effect on different types of excitations such as electrons, phonons, excitons or magnons has been the focus of some recent studies (146; 147). Also, a number of material properties like electric, magnetic or thermal have been successfully examined as a function of the size. For perovskite-based materials one of the most common questions concerns the ferroic (combined ferroelectric and ferromagnetic) properties. For instance, the suppression of ferroelectricity in $PbTiO_3$ ultrathin films with the sample thickness has been analyzed in the recent synchrotron x-ray study, where no thickness limit has been observed (148). This fact has been additionally confirmed by *ab initio* calculations that demonstrated the

existence of a stable ferroelectricity in $PbTiO_3$ and $BaTiO_3$ films as thin as a few unit cells (149), in a sharp contrast to the phenomenological Landau-Ginzburg theory (150).

In view of immense interest to nanoionic systems in which ions, being significant charge carriers, rather than electrons play a considerable role (44), the investigation of confinement effects on ionic defects also represent great interest. Very recently, the properties of ionic defects have received much attention for the understanding of interfacially-controlled materials such as, for example, nanosized ionic heterostructures as has been demonstrated for the ionic conductivity in CaF_2-BaF_2 films of nanothickness (52). Here we would like to address some aspects of size-effects, namely, how the electronic and energetic properties of an ionic defect are changed when confined in an ultrathin film, which is an important example of one-dimensional confinement.

We have chosen here $SrTiO_3$ as a prototypical crystal for a wide class of ABO_3 perovskite-structured materials with partly covalent chemical bonding, and oxygen vacancy (for a comparison in the form of both neutral and positively charged species) therein as a common ionic carrier in this type of solids. Oxygen vacancies are abundant defects in non-stoichiometric ABO_3 perovskite family oxides and their behavior/properties in nano-thin films or at surface is important for a huge number of applications, including new high density electronic memories (6), high-k nano-capacitors (148; 151), magnetoresistence at the interface of non-magnetic oxides (152), spintronics (153), optoelectronics (154), etc. In the case of an oxygen vacancy in thin films the confinement effects might depend on the restricted ionic relaxation around a vacancy (elastic effect) and on an electron wave function distribution/localization (electronic effect). For the better description of electronic properties including localization of electron density and defect one-electron level position within the band gap, we have applied here the hybrid HF-DFT *ab initio* method with the B3PW exchange-correlation functional as

previously for the study of oxygen vacancies in bulk and on surfaces.

We examine an oxygen vacancy in ultrathin films exploiting a periodic two-dimensional supercell model and considering the symmetrical (001) slabs of different thickness (3-, 5-, 7- and 9-planes) with a 2×2 and a 3×3 surface cells. The results obtained for a 3×3 surface cell are qualitatively similar to those for smaller cell for the neutral vacancy. For the charge vacancy a 3×3 cell was used. One of oxygen atoms in the central plane of a slab was removed and the "ghost" wave functions were retained at the vacancy site. We studied the slabs with either SrO (I-type, Figure 6.1a) or TiO_2 (II-type, Figure 6.1a) central plane with a single oxygen vacancy V_O. These two situations correspond to the arrangement of Ti–V_O–Ti complex perpendicular or parallel to the surfaces, respectively, and allow us to compare both cases.

In order to analyze the electronic effect related to the density redistribution nearby the vacancy site under confinement conditions, we plotted (Figure 6.1) two-dimensional difference electron density maps . It is seen on the example of a neutral vacancy that the electron density redistribution is observed only in the thinnest three-layer slabs, mainly between the vacancy and the nearest Ti ions, whereas a rather strong polarization is related to the surface atoms in all slabs under consideration. To illustrate this better, we present in Tables 6.1 and 6.2 the effective Mulliken atomic charges for both unrelaxed and relaxed structures which are consistent with the density maps. The analysis for the I-type slab shows that V_O traps one electron and there is a noticeable redistribution of the electron density at the vacancy site with respect to the bulk, namely, the decrease of the charge observed only in the thinnest slab. However, the situation is quite opposite for the II-type three-layer slab. In this case, the two Ti atoms nearest to V_O lie on the slab surface and reveal larger charges that in the I-type case. This trend is independent on the structure relaxation meaning that it is mainly the electronic effect.
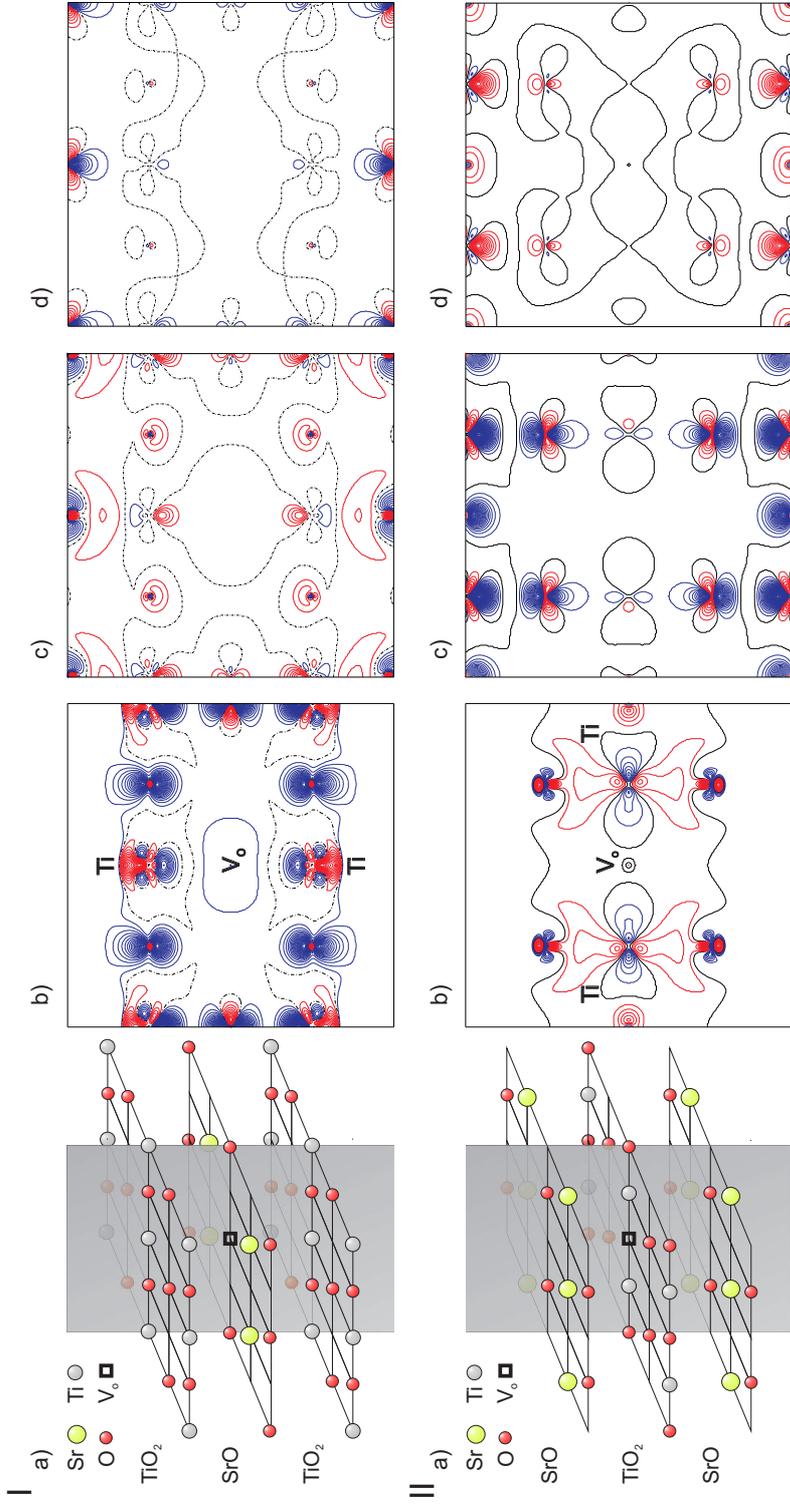
Figure 6.1: The sketches of I- and II-type slabs with the cross-section plane (a) and the difference electron density maps for the density around the neutral oxygen vacancy (at the center) in 9-plane slab minus that in 3-, 5- and 7-plane slabs (a, b, c, respectively). All plots correspond to unrelaxed structures to match geometries. Black, red and blue solid isolines correspond to the zero, negative and positive values of electron density, respectively. Isodensity curves are drawn from -0.1 to 0.1 e Å^{-3} with an increment of 0.002 e Å^{-3}.

Table 6.1: I-type slabs: Mulliken effective atomic charges q (e) and displacements of titanium atoms around the oxygen vacancy Δ (Å), negative sign corresponds to the inward relaxation; N number of planes in the slab, T slab termination.

N/T	$3/TiO_2$	$5/SrO$	$7/TiO_2$	$9/SrO$	bulk
			unrelaxed		
q (V$_O$)	1.08	1.32	1.27	1.29	1.30
q (Ti)	2.26	2.40	2.36	2.37	2.37
			relaxed		
q (V$_O$)	1.15	1.20	1.25	1.25	1.26
q (Ti)	2.27	2.36	2.36	2.37	2.37
Δ (Ti-V$_O$)	-0.19	0.08	-0.06	-0.03	-0.03

Table 6.2: The same as Table 6.1 for II-type of slabs.

N/T	$3/SrO$	$5/TiO_2$	$7/SrO$	$9/TiO_2$	bulk
			unrelaxed		
q (V$_O$)	1.35	1.28	1.29	1.29	1.30
q (Ti)	2.43	2.36	2.37	2.36	2.37
			relaxed		
q (V$_O$)	1.33	1.21	1.25	1.25	1.26
q (Ti)	2.41	2.34	2.36	2.37	2.37
Δ (Ti-V$_O$)	-0.07	-0.11	-0.06	-0.03	-0.03

Table 6.3: The V_O energy level characteristics for the I-type slabs: $\Delta\varepsilon$ (eV) is the defect level position within the bandgap with respect to the bottom of conduction band, $\delta\varepsilon$ (eV) the dispersion of the defect band over the Brillouin zone; N number of planes in the slab, T slab termination.

N/T	$3/TiO_2$	$5/SrO$	$7/TiO_2$	$9/SrO$	bulk[1]
		unrelaxed			
$\Delta\varepsilon$	1.74	0.65	0.87	0.72	0.84
$\delta\varepsilon$	0.05	0.08	0.08	0.11	0.13
		relaxed			
$\Delta\varepsilon$	1.81	0.20	0.96	0.39	0.79
$\delta\varepsilon$	0.03	0.09	0.07	0.10	0.13

[1]Periodicity of the defect is 11.01 Å.

We also calculated the band structure for all I-type slabs and found the characteristics of the vacancy band within the bandgap which are summarized in Table 6.3. One can recognize that the most pronounced effect is observed again only for the thinnest slab: the vacancy defect level becomes here a much deeper compared to the bulk, thus being more localized and demonstrating a smaller dispersion throughout the BZ. This dispersion, reflecting the interaction between neighboring periodically distributed oxygen vacancies, is very small for I-type slab but much larger ($\sim$0.9 eV) for the II-type slabs, due to the stronger interactions between the laterally arranged Ti–V_O–Ti complexes.

The calculation of formation energy for the neutral vacancy (with respect to the isolated O atom in vacuum in the ground triplet state) as a function of a slab thickness reveals a drastic drop of $\sim$1 eV in three-plane slab with a central SrO layer (I-type model). Note that no energy drop is observed for the V_O in TiO$_2$ layer for three-plane slab (II-type model). This shows that the confinement effect depends greatly on the Ti–V_O–Ti complex orientation with respect to the

surfaces. Full optimization of the slab structure changes the formation energies only slightly (by $\sim$0.1 eV). As a slab thickness increases, the energies rapidly converge to the value for the bulk vacancy. We also found the same tendency for a single positively charged vacancy.

The obtained results for both types of vacancies in a series of nanosize slabs and the bulk clearly demonstrate that the change in the electronic and, as a result, energetic properties of this defect in $SrTiO_3$ films is mainly due to the interaction between the oxygen vacancy and the two neighboring titanium atoms. This is why the effect of one-dimensional confinement is mostly restricted to the thinnest films, thus being short-range effect.

It is expected that the effect of the confinement should be different for more covalent or more ionic systems. For instance, in covalent compounds such as TiO_2 crystal, the electronic effect should be more pronounced. On the other hand, in more ionic systems, like MgO and SrO oxides, the atomic relaxation around the positively charged oxygen vacancy is quite considerable, the displacements of Sr ions around the vacancy being about 6-7% of lattice constant in the bulk crystal. Hence, the changes in electronic properties are to be mostly ascribed to the elastic effect.

Chapter 7

Summary

The main goal of the present thesis was the theoretical study of substitutional iron impurities and oxygen vacancies present in different charge states in the bulk and on the $SrTiO_3$ (001) surface by means of first-principles simulations. These two types of point defects represent very common imperfections in ABO_3-type perovskite oxides diversifying their chemistry and leading to a broad range of possible technological applications.

Our first step was to examine basic properties of perfect perovskite crystals. We found for $SrTiO_3$ and $SrFeO_3$ parent compounds that the best agreement with experimental data on lattice constant, bulk modulus, cohesive energy and optical band gap is provided by the hybrid Hartree-Fock and the density functional theory (DFT) approach in the linear combination of atomic orbitals approximation with the so-called B3PW functional which was therefore chosen as a main tool in the study. In addition, we performed simulations on both orthorhombic and monoclinic phases of $CaFeO_3$ as this material, unlike $SrTiO_3$ and $SrFeO_3$, deserves attention due to the transition from a metallic orthorhombic ($Pbnm$) to a narrow-gap semiconducting monoclinic ($P2_1/n$) phase accompanied by a charge/spin disproportionation. The hybrid method used allows us to obtain atomic, electronic and magnetic structures in very good agreement with the pow-

der neutron diffraction data. We ascribe metal-semiconductor transition (with an opening of 0.9 eV bandgap) to a larger distortion of the Fe–O–Fe bond angle in the monoclinic phase and confirmed the disproportionation between two nonequivalent iron atoms in the monoclinic phase for charges and spin densities. In addition, the calculated Brillouin zone-center phonon modes (Raman and optical) are in good agreement with available experimental data; we also analyzed the vibrational pattern of the modes applying the isotopic substitution technique. These calculations demonstrate the great predicting ability of the hybrid method applied.

In order to study $SrFe_xTi_{1-x}O_3$ solid solutions, we carried out a series of calculations for various iron contents (50, 6.25, 3.70, 3.125, and 1.85 at.%) in doped $SrTiO_3$. We found that the Jahn-Teller (JT) distortion around an Fe^{4+} ion is the largest for the most dilute solid solution, becomes less pronounced for 50% iron doping, and disappears in a pure $SrFeO_3$. This tendency in changing the magnitude of the JT distortion agrees well with the EXAFS experimenatal data extrapolated to the dilute defect limit. Also, the electronic structure calculations indicate that $SrFe_xTi_{1-x}O_3$ containing more than 50% iron is metallic, and that its conductivity is caused by a strong mixing of O $2p$ and Fe $3d$ (e_g) states in the pre-Fermi energy region. We found that the iron impurity insertion energy of 1.79 eV (1.85% iron content) is very close to that for 6.25% iron, and this energy decreases down to 1.59 eV for 50% and lastly to 1.57 eV for a pure $SrFeO_3$.

Calculations of iron impurities on the $SrTiO_3$ (001) surfaces revealed that the Fe^{4+} ion has the propensity to segregate from the bulk to both SrO and TiO_2 facets, with the segregation energies of 0.32 and 0.48 eV, respectively. The Mulliken population analysis indicates that the presence of Fe^{4+} ion in the subsurface plane significantly reduces the charge of the nearest oxygen atom at the topmost SrO surface (in a comparison to the substituted Ti^{4+}), thus severely diminishing its basic properties. Also, the covalent character of the M–O (M = Fe, Ti) chem-

ical bond is increased at the surfaces with respect to the bulk. This is important for the further studies of the solid oxide fuel cell cathodes and oxygen reduction therein, as well as defect chemistry of perovskites in general.

We also examined the neutral and positively single-charged oxygen vacancies (F and F^+ centers), both in the bulk and on the $SrTiO_3$ (001) surfaces. It was found that the neutral vacancy has an even higher tendency than Fe^{4+} ions to surface segregation, being ~ 1.0 eV for SrO and 1.4 eV for TiO_2 surfaces. The defect energy level becomes much more shallow when going from the bulk (0.77 eV below the bottom of the conduction band at the Γ-point of the BZ) to SrO (0.27 eV) and TiO_2 surfaces (very shallow level, almost degenerate with the CB within an accuracy of the method).

Our simulations of the bulk charged F^+ center show that it has a deeper energy level (1.20 eV) than the neutral defect revealing also a lower vacancy formation energy. The charged nature of the center results in a more pronounced relaxation around the defect with a repulsive interaction with neighboring titanium atoms. This relaxation becomes even stronger at the surface. Thus, a common feature of both types of vacancies is the more shallow energy levels on the surfaces compared to the bulk, particularly, for the TiO_2 facet, while the effect is less pronounced for the F^+ center.

We simulated additionally the diffusion of oxygen species by means of the density functional theory combined with the nudged elastic band (NEB) method. We have shown that the calculated activation barrier for diffusion of oxygen vacancy along the TiO_2 surface is almost by a factor of three smaller than in the bulk (0.14 vs. 0.38 eV). Adsorption energy of oxygen atom atop Ti ion for the TiO_2 facet is as large as 2.13 eV being considerably higher than that atop Sr ion on SrO facet (0.57 eV). Moreover, the creation of surface oxygen vacancy nearby the O atom adsorbed atop Ti ion leads to a significant increase in the O_{ads}-Ti binding energy. Because of such a strong adsorbate-adsorbent

bonding, penetration of the adsorbed O atom into the surface layer could occur predominantly when the very mobile surface oxygen vacancy meets adsorbed oxygen atom. Simulation of a drop of the adsorbed O atom into the oxygen vacancy nearby reveals a distinguishable but extremely small activation barrier, $\sim$0.01 eV. Thus, we predict almost no-barrier soaking of the adsorbed O atom into the surface layer, fast surface diffusion of the oxygen vacancies and a much slower diffusion in the bulk.

Considerable part of our study was devoted to the examination of oxygen vacancies (neutral and charged) as important ionic charge carriers under confinement conditions. This aspect is of paramount importance in nanoionic systems in which the boundary zones overlap and not only the density but in addition the nano-size spacing at interfaces becomes a key factor. To address this issue, we considered the one-dimensional confinement effect on oxygen vacancies in $SrTiO_3$ ultrathin films. It was revealed for the neutral vacancy that size effects are very short-ranged and restricted mostly to the thinnest (3-plane) nano-films, leading to a large decrease of the defect formation energy (by 1 eV), a much deeper defect level and a noticeable change in the electronic density redistribution at the vacancy site with respect to the bulk. The results also show that the size effects pertain to the interactions between the oxygen vacancy and two neighboring Ti atoms and orientation (parallel or perpendicular to the surface) of the Ti-V_O-Ti defect cluster.

Chapter 8

Zusammenfassung

Die vorliegende Arbeit befaßt sich mit der theoretischen Modellierung zweier typischer Punktdefekte in $SrTiO_3$ mittles first-principles Simulationen im Volumen und an Oberflächen: Fe als substitutionelle Akzeptordotierung und der Sauerstoffleerstelle. Die Variation derselben erlaubt das Durchstimmen einer ganzen Palette von High-Tech-Anwendungen.

Zunächst wurden grundlegende Eigenschaften perfekter Perowskitkristalle überprüft. Für die Ausgangsmaterialien $SrTiO_3$ und $SrFeO_3$ wurde die beste Übereinstimmung mit experimentellen Daten (Gitterkonstanten, Bulkmodulus, Kohäsionsenergie, optische Bandlücke) durch die Verwendung einer Kombination aus Hartree-Fock und Dichtefunktionaltheorie innerhalb der LCAO-Methode (Linearkombination von Atomorbitalen) mit der so genannten B3PW Funktional erhalten, die als Hauptwerkzeug für die Studie gewählt wurde. Die erwähnte Kombinationsmethode führt zu atomistischen, elektronischen und magnetischen Strukturdaten, die sehr gut mit Pulver-Neutronen-Beugungdaten übereinstimmen. Des Weiteren wurden Simulationen an der orthorhombischen und monoklinen Phase von $CaFeO_3$ durchgeführt. Im Gegensatz zu $SrTiO_3$ und $SrFeO_3$ findet in diesem Material ein Übergang von der metallischen orthorhombischen Phase ($Pbnm$) zu einer monoklinen ($P2_1/n$) Halbleiterphase statt. Der Metall-Halbleiter Übergang

(mit einer schmalen Bandlücke von 0.9 eV) wird der stärkeren Verzerrung des Fe–O–Fe Bindungswinkels in der monoklinen Phase zugeschrieben. Außerdem tritt eine Disproportionierung der Ladungs- und Spindichte für zwei nicht äquivalente Eisenatome in der monoklinen Phase auf. Die berechneten Phonon-Modi für die Brillouin-Zonen-Zentren (Raman und optisch) stimmen gut mit vorhandenen experimentellen Daten überein. Mittels der Isotopen-Substitutions-Methode wurde auch das Schwingungsmuster dieser Modi analysiert. Die Berechnungen zeigen eine sehr gute Vorhersagefähigkeit der angewendeten Kombinationsmethode.

Um feste Lösungen $SrFe_xTi_{1-x}O_3$ zu untersuchen, wurden Berechnungen für eine Reihe verschiedener Eisengehalte (50, 6.25, 3.70, 3.125 und 1.85%) in $SrTiO_3$ durchgeführt. Es zeigte sich, dass die Jahn-Teller (JT) Verzerrung um ein Fe^{4+}-Ion in der verdünntesten festen Lösungen am stärksten ist, bei 50% Eisengehalt ist sie weniger stark ausgeprägt und im Falle eines reinen $SrFeO_3$ verschwindet sie ganz. Diese Tendenz in der Änderung der Stärke der JT-Verzerrung stimmt gut mit den experimentellen EXAFS Daten überein, wenn man diese in den Bereich verdünnter Defekte extrapoliert. Die Berechnungen der elektronischen Struktur demonstrieren, dass $SrFe_xTi_{1-x}O_3$ mit mehr als 50% Eisen metallisch ist und dass seine Leitfähigkeit durch eine starke Vermischung der O $2p$ und Fe $3d$ (e_g) Zustände in der pre-Fermi Energieregion verursacht wird. Es wurde auch gezeigt, dass die Energie zum Eintrag einer Eisenverunreinigung mit 1.79 eV bei 1.85% Eisengehalt nur um 0.01 eV höher ist als bei einem Eisengehalt von 6.25%. Die Energie nimmt mit steigendem Eisengehalt weiter ab; sie sinkt auf 1.59 eV für 50% Eisengehalt und auf 1.57 eV für reines $SrFeO_3$.

Berechnungen der Eisenverunreinigung an den $SrTiO_3$ (001) Oberflächen machten deutlich, dass das Fe^{4+}-Ion zur Segregation aus dem Volumen an die beiden Oberflächen (SrO, TiO_2) neigt. Die entsprechenden Segregationsenergien sind 0.32 eV für die SrO und 0.48 eV für die TiO_2 Oberfläche. Die Mulliken Besetzungsanalyse zeigt, dass das Vorhandensein eines Fe^{4+}-Ions statt eines Ti^{4+}-Ions

in der Ebene unter der Oberfläche erheblich die Ladung des nächsten Sauerstoffatoms an der obersten SrO Fläche verringert, dies vermindert stark grundlegende Eigenschaften der SrO Oberfläche. Auch der kovalente Charakter der M–O Bindung (M = Fe, Ti) wird an den Oberflächen im Vergleich zum Volumen erhöht. Dies ist wichtig für weitere Studien an Festoxidbrennstoffzellenkathoden und der Sauerstoffreduktion darin.

Außerdem wurden die neutralen und einfach positiv geladenen Sauerstoffleerstellen (F und F^+-Zentren) untersucht, sowohl im Volumen als auch für die SrTiO$_3$ (001) Oberfläche. Die neutralen Leerstellen haben eine noch höhere Tendenz zur Oberflächensegregation als Fe^{4+}-ionen, mit 1.0 eV für SrO und 1.4 eV für TiO$_2$ Oberflächen. Das Defektenergieniveau wird sehr viel flacher beim Übergang vom Volumen (0.77 eV geringer als das untere Niveau des Leitungsbandes am Γ-point der Brillouin Zone) zu SrO (0.27 eV) und TiO$_2$ Oberflächen (sehr flach, nahezu gleich mit dem Leitungsband innerhalb der Fehlergenauigkeit der Methode). Unsere Simulationen zeigen, dass die F^+-Zentren im Volumen ein tieferes Energieniveau (1.20 eV) aufweisen als die neutralen Defekte, was auch mit einer geringeren Leerstellenbildungsenergie einhergeht. Der geladene Zustand der Zentren führt zu einer verstärkten Relaxation rund um den Defekt mit abstoßenden Wechselwirkungen gegenüber den benachbarten Titanatomen. Diese Relaxation wird noch stärker an der Oberfläche. Demzufolge sind die flacheren Energieniveaus an den Oberflächen im Vergleich zum Volumen eine gemeinsame Eigenschaft der beider Formen von Leerstellen (insbesondere für die TiO$_2$ Oberfläche), wobei dieser Effekt für die F^+-Zentren weniger stark ausgeprägt ist.

Des Weiteren wurde die Diffusion der Sauerstoffspezies mittels der Nudge-Elastic-Band (NEB) Methode in Kombination mit der Dichte-Funktional-Theorie simuliert. Es wurde gezeigt, dass die berechnete Aktivierungsschwelle für die Diffusion von Sauerstoffleerstellen entlang der TiO$_2$ Oberfläche fast dreimal kleiner ist als für das Volumen (0.14 eV vs. 0.38 eV). Die Adsorptionsenergie für ein

Sauerstoffatom oberhalb eines Ti-Atoms in der TiO$_2$ Oberfläche ist mit 2.13 eV merklich größer als für die Adsorption oberhalb eines Sr-Atoms in der SrO Oberfläche (0.57 eV). Darüber hinaus führt die Bildung einer Oberflächensauerstoffleerstelle in der Nähe des oberhalb eines Ti-Atoms adsorbierten O zu einem deutlichen Anstieg der O$_{ads}$–Ti-Bindungsenergie. Aufgrund der starken Adsorbat-Adsorber-Bindung ist die Diffusion des adsorbierten O-Atoms entlang der Oberfläche gehemmt. Tritt jedoch eine sehr mobile Oberflächensauerstoffleerstelle hinzu, könnte das adsorbierte O-Atom in die Oberflächenschicht eindringen. Die Simulation des Eintretens des adsorbierten O-Atoms in die nahegelegene Sauerstoffleerstelle ergibt eine erkennbare aber extrem niedrige Aktivierungsschwelle, 0.01 eV. Demzufolge sagen wir ein nahezu ungehindertes Eindringen des O-Atoms in die Oberflächenschicht voraus sowie eine schnelle Oberflächendiffusion der Sauerstoffleerstellen und eine deutlich geringere Diffusion im Volumen voraus.

Ein großer Teil unserer Studien ist der Untersuchung von Sauerstoffleerstellen (neutral und geladen) als wichtige ionische Ladungsträger unter eingeschränkten Bedingungen gewidmet. Dieser Aspekt ist von höchster Wichtigkeit in nano-ionischen Systemen in denen Grenzzonen überlappen und nicht nur die Dichte, sondern auch die Abstände der Grenzschichten zu einem Schlüsselfaktor werden. Um diesen Punkt zu untersuchen wurde die eindimensionale Beschränkung für Sauerstoffleerstellen in ultradünnen SrTiO$_3$-Filmen angewendet. Für neutrale Leerstellen hat sich ergeben, dass Größeneffekte eher von geringerer Reichweite und auf die dünnsten (3 Ebenen) Nanofilme beschränkt sind. Dies führt zu einem großen Abfall der Defektbildungsenergie (um 1 eV), einem deutlich tieferen Defektenergieniveau und einem merklichen Unterschied in der Elektronendichteverteilung an der Leerstellenseite im Vergleich zum Volumen. Die Resultate zeigen, dass Größeneffekte vor allem die Wechselwirkungen zwischen Sauerstoffleerstellen und benachbarten Ti-Atomen und die Orientierung (parallel oder senkrecht zur Oberfläche) des Ti–V$_O$–Ti Defektclusters betreffen.

References

[1] J. M. Qiao and C. Y. Yang, Materials Science & Engineering R-Reports **14**, 157 (1995). 1

[2] S. Soltan, J. Albrecht, and H. U. Habermeier, Physical Review B **70**, 144517 (2004). 1

[3] O. Nakagawara et al., Applied Physics Letters **77**, 3257 (2000). 1

[4] J. Choi, C. B. Eom, G. Rijnders, H. Rogalla, and D. H. A. Blank, Applied Physics Letters **79**, 1447 (2001). 1

[5] A. A. Sirenko et al., Nature **404**, 373 (2000). 2

[6] R. Waser and M. Aono, Nature Materials **6**, 833 (2007). 2, 7, 88

[7] M. S. Wrighton et al., Journal of the American Chemical Society **98**, 2774 (1976). 2

[8] M. O'Donoghue, *Synthetic, imitation and treated gemstones*, Elsevier Butterworth-Heinemann, Great Britain, 2002. 2

[9] W. Zhong, R. D. Kingsmith, and D. Vanderbilt, Physical Review Letters **72**, 3618 (1994). 2, 35

[10] K. van Benthem, C. Elsasser, and R. H. French, Journal of Applied Physics **90**, 6156 (2001). 2, 34, 36

[11] S. Piskunov, E. Heifets, R. I. Eglitis, and G. Borstel, Computational Materials Science **29**, 165 (2004). 2, 28, 35, 40

[12] S. Piskunov et al., Surface Science **575**, 75 (2005). 2, 3, 75

[13] R. A. Evarestov, A. V. Bandura, and V. E. Alexandrov, Surface Science **601**, 1844 (2007). 2, 76

[14] B. Meyer, J. Padilla, and D. Vanderbilt, Faraday Discussions **114**, 395 (1999). 2

[15] G. Koster, G. Rijnders, D. H. A. Blank, and H. Rogalla, Physica C-Superconductivity and Its Applications **339**, 215 (2000). 3

[16] Q. D. Jiang and J. Zegenhagen, Surface Science **425**, 343 (1999). 3

[17] M. R. Castell, Surface Science **505**, 1 (2002). 3, 77

[18] T. Kubo and H. Nozoye, Physical Review Letters **86**, 1801 (2001). 3

[19] R. Courths, B. Cord, and H. Saalfeld, Solid State Communications **70**, 1047 (1989). 3, 77

[20] P. E. Blöchl and J. H. Stathis, Physical Review Letters **83**, 372 (1999). 3

[21] J. W. McPherson and H. C. Mogul, Journal of Applied Physics **84**, 1513 (1998). 3

[22] L. X. He and D. Vanderbilt, Physical Review B **68**, 134103 (2003). 3, 4, 79

[23] J. Robertson, Reports on Progress in Physics **69**, 327 (2006). 3

[24] A. S. Foster, F. L. Gejo, A. L. Shluger, and R. M. Nieminen, Physical Review B **65**, 174117 (2002). 3, 60

[25] R. Merkle and J. Maier, Angewandte Chemie-International Edition **47**, 3874 (2008). 4, 5, 6, 7, 84

[26] R. Astala and P. D. Bristowe, Modelling and Simulation in Materials Science and Engineering **9**, 415 (2001). 4, 61

[27] J. P. Buban, H. Iddir, and S. Öğüt, Physical Review B **69**, 180102 (2004). 4, 61

[28] Y. F. Zhukovskii, E. A. Kotomin, R. A. Evarestov, and D. E. Ellis, International Journal of Quantum Chemistry **107**, 2956 (2007). 4, 61

[29] P. J. Gellings and H. J. M. Bouwmeester, Catalysis Today **58**, 1 (2000). 4

[30] M. A. Pena and J. L. G. Fierro, Chemical Reviews **101**, 1981 (2001). 4

[31] N. Izu, W. Shin, N. Murayarna, and S. Kanzaki, Sensors and Actuators B-Chemical **87**, 95 (2002). 4

[32] G. I. Panov, K. A. Dubkov, and E. V. Starokon, Catalysis Today **117**, 148 (2006). 4

[33] J. Carrasco et al., Physical Review B **73**, 064106 (2006). 5, 61, 77

[34] M. Vračar et al., Physical Review B **76**, 174107 (2007). 6, 51, 52, 53, 54, 55

[35] R. A. Evarestov, S. Piskunov, E. A. Kotomin, and G. Borstel, Physical Review B **67**, 064101 (2003). 6

[36] A. Rothschild et al., Sensors and Actuators B-Chemical **108**, 223 (2005). 6, 74

[37] R. Merkle and J. Maier, Physical Chemistry Chemical Physics **4**, 4140 (2002). 6

[38] R. A. De Souza, J. Fleig, R. Merkle, and J. Maier, Zeitschrift für Metallkunde **94**, 218 (2003). 6

[39] R. A. De Souza et al., Journal of the American Ceramic Society **86**, 922 (2003). 6, 74

[40] J. Maier, Journal of the European Ceramic Society **24**, 1251 (2004). 6

[41] E. S. Kirkpatrick, R. S. Rubins, and K. A. Müller, Physical Review A-General Physics **135**, A86 (1964). 6

[42] O. F. Schirmer, W. Berlinger, and K. A. Müller, Solid State Communications **16**, 1289 (1975). 6

[43] S. H. Paek et al., Journal of Materials Science **33**, 1239 (1998). 6, 67

[44] J. Maier, Nature Materials **4**, 805 (2005). 7, 88

[45] A. V. Chadwick and S. L. P. Savin, Solid State Ionics **177**, 3001 (2006). 7

[46] A. L. Despotuli and V. I. Nikolaichik, Solid State Ionics **60**, 275 (1993). 7

[47] A. A. Volkov, G. V. Kozlov, G. I. Mirzoev, and V. G. Gofman, JETP Letters **38**, 213 (1983). 7

[48] J. Maier, Berichte Der Bunsen-Gesellschaft-Physical Chemistry Chemical Physics **88**, 1057 (1984). 7

[49] D. B. Strukov, G. S. Snider, D. R. Stewart, and R. S. Williams, Nature **453**, 80 (2008). 7, 60

[50] M. Fujimoto, Y. M. Chiang, A. Roshko, and W. D. Kingery, Journal of the American Ceramic Society **68**, C300 (1985). 8

[51] M. Leonhardt, J. Jamnik, and J. Maier, Electrochemical and Solid State Letters **2**, 333 (1999). 8

[52] N. Sata, K. Eberman, K. Eberl, and J. Maier, Nature **408**, 946 (2000). 8, 88

[53] Garcia-Barriocanal et al., Science **321**, 676 (2008). 8

[54] R. M. Martin, *Electronic Structure: Basic Theory and Practical Methods*, Cambridge University Press, 2004. 9, 16, 19

[55] R. A. Evarestov, *Quantum Chemistry of Solids. The LCAO First Principles Treatment of Crystals*, volume 153, Springer-Verlag, 2007. 9, 19, 31, 35, 61

[56] V. Fock, Zeitschrift für Physik **61**, 126 (1930). 14

[57] C. C. J. Roothaan, Reviews of Modern Physics **23**, 69 (1951). 14

[58] G. G. Hall, Proceedings of the Royal Society of London Series A-Mathematical and Physical Sciences **205**, 541 (1951). 14

[59] M. I. Petrashen and E. D. Trifonov, *Applications of Group Theory in Quantum Mechanics*, The MIT Press, 1969. 15

[60] M. I. Petrashen and E. D. Trifonov, *Applications of Group Theory in Quantum Mechanics (in russian)*, Moscow, Editorial URSS, 3rd edition, 2000. 15, 26, 27

[61] C. Pisani, R. Dovesi, and C. Roetti, *Hartree-Fock ab-initio of crystalline systems, Lecture Notes in Chemistry*, volume 48, Spinger Verlag, Heidelberg, 1988. 15

[62] *R. Dovesi, V. R. Saunders, C. Roetti, R. Orlando, C. M. Zicovich-Wilson, F. Pascale, B. Civalerri, K. Doll, N. M. Harrison, I. J. Bush, Ph. D'Arco , M. Llunell, CRYSTAL-2006 User's Manual, University of Torino, Torino, 2006.* 15, 28, 40

[63] R. A. Evarestov and V. P. Smirnov, *Site Symmetry in Crystals*, volume 108 of *Springer Series in Solid State Sciences*, Springer, Berlin, Heidelberg, 1993. 16, 17

[64] W. Kohn and L. J. Sham, Physical Review **140**, 1133 (1965). 18

[65] A. D. Becke, Journal of Chemical Physics **98**, 5648 (1993). 19, 28, 40

[66] F. Cora et al., Principles and Applications of Density in Inorganic Chemistry **113**, 171 (2004). 19

[67] J. Paier, R. Hirschl, M. Marsman, and G. Kresse, Journal of Chemical Physics **122**, 234102 (2005). 19

[68] *Kresse G., Furthmüller J., VASP the Guide (University of Vienna, Austria, 2005)*. 19, 30

[69] G. Kresse and J. Hafner, Physical Review B **48**, 13115 (1993). 19, 30

[70] G. Kresse and J. Hafner, Physical Review B **49**, 14251 (1994). 19, 30

[71] P. Durand and J. C. Barthelat, Theoretica Chimica Acta **38**, 283 (1975). 21

[72] P. J. Hay and W. R. Wadt, Journal of Chemical Physics **82**, 270 (1985). 21, 28

[73] D. Andrae, U. Haussermann, M. Dolg, H. Stoll, and H. Preuss, Theoretica Chimica Acta **77**, 123 (1990). 21

[74] J. M. Ziman, *Principles of the Theory of Solids*, Cambridge University Press, 2nd edition, 1972. 22

[75] D. J. Chadi and M. L. Cohen, Physical Review B **8**, 5747 (1973). 22

[76] H. J. Monkhorst and J. D. Pack, Physical Review B **13**, 5188 (1976). 22, 29, 40

[77] R. A. Evarestov and V. P. Smirnov, Physica Status Solidi B-Basic Research **119**, 9 (1983). 22

[78] G. Gilat and L. J. Raubenheimer, Physical Review **144**, 390 (1966). 23

[79] D. R. Hamann, M. Schluter, and C. Chiang, Physical Review Letters **43**, 1494 (1979). 24

[80] D. Vanderbilt, Physical Review B **41**, 7892 (1990). 24

[81] P. E. Blöchl, Physical Review B **50**, 17953 (1994). 24, 30

[82] R. A. Marcus, Journal of Chemical Physics **45**, 4493 (1966). 24

[83] R. P. Feynman and A. R. Hibbs, *Quantum Mechanics and Path Integrals*, McGraw-Hill, New York, 1965. 24

[84] G. Mills and H. Jonsson, Physical Review Letters **72**, 1124 (1994). 24

[85] G. Mills, H. Jonsson, and G. K. Schenter, Surface Science **324**, 305 (1995). 24

[86] H. A. Jahn and E. Teller, Proceedings of the Royal Society of London Series A-Mathematical and Physical Sciences **161**, 220 (1937). 26

[87] I. B. Bersuker, *The Jahn-Teller Effect*, Cambridge University Press, 2nd edition, 2006. 26, 27, 28

[88] I. Hargittai and M. Hargittai, Structural Chemistry **19**, 181 (2008). 26

[89] R. A. Evarestov, S. Piskunov, E. A. Kotomin, and G. Borstel, Physical Review B **67**, 064101 (2003). 28, 50, 52

[90] J. P. Perdew, K. Burke, and M. Ernzerhof, Physical Review Letters **77**, 3865 (1996). 28, 30, 35

[91] M. Catti, G. Valerio, and R. Dovesi, Physical Review B **51**, 7441 (1995). 29, 40

[92] F. Pascale et al., Journal of Computational Chemistry **25**, 888 (2004). 30, 44

[93] C. M. Zicovich-Wilson et al., Journal of Computational Chemistry **25**, 1873 (2004). 30, 40, 44

[94] P. K. Gallagher, J. B. MacChesney, and D. N. E. Buchanan, Journal of Chemical Physics **43**, 516 (1965). 34

[95] J. Zaanen, C. Westra, and G. A. Sawatzky, Physical Review B **33**, 8060 (1986). 34

[96] A. E. Bocquet et al., Physical Review B **45**, 1561 (1992). 34, 37

[97] M. Abbate et al., Physical Review B **65**, 165120 (2002). 34

[98] S. Tinte, M. G. Stachiotti, C. O. Rodriguez, D. L. Novikov, and N. E. Christensen, Physical Review B **58**, 11959 (1998). 35

[99] D. E. Usvyat, R. A. Evarestov, and V. P. Smirnov, International Journal of Quantum Chemistry **100**, 352 (2004). 35

[100] S. M. Jaya, R. Jagadish, R. S. Rao, and R. Asokamani, Physical Review B **43**, 13274 (1991). 35

[101] S. F. Matar, Progress in Solid State Chemistry **31**, 239 (2003). 35

[102] I. R. Shein, K. I. Shein, V. L. Kozhevnikov, and A. L. Ivanovskii, Physics of the Solid State **47**, 2082 (2005). 35, 36, 38, 57

[103] I. R. Shein, V. L. Kozhevnikov, and A. L. Ivanovskii, JETP Letters **82**, 220 (2005). 35, 37

[104] Y. A. Abramov, V. G. Tsirelson, V. E. Zavodnik, S. A. Ivanov, and I. D. Brown, Acta Crystallographica Section B-Structural Science **51**, 942 (1995). 36

[105] *Ferroelectrics and Related Substances, New Series, vol. 3, Landolt-Bornstein*, Springer Verlag, Berlin, 1969. 36

[106] D. Ricci, G. Bano, G. Pacchioni, and F. Illas, Physical Review B **68**, 224105 (2003). 36

[107] T. Takeda, Y. Yamaguch, and H. Watanabe, Journal of the Physical Society of Japan **33**, 967 (1972). 38

[108] P. M. Woodward, D. E. Cox, E. Moshopoulou, A. W. Sleight, and S. Morimoto, Physical Review B **62**, 844 (2000). 39, 41, 42, 43

[109] M. Takano, N. Nakanishi, Y. Takeda, S. Naka, and T. Takada, Materials Research Bulletin **12**, 923 (1977). 39

[110] J. B. Yang et al., Journal of Applied Physics **97**, 10A312 (2005). 40, 41, 43

[111] M. Catti, R. Dovesi, A. Pavese, and V. R. Saunders, Journal of Physics-Condensed Matter **3**, 4151 (1991). 40

[112] M. Takano, N. Nakanishi, Y. Takeda, and S. Naka, Journal de Physique Colloque **40**, C2/313 (1979). 41

[113] S. Ghosh et al., Physical Review B **71**, 245110 (2005). 46

[114] M. Vaccari and P. Fornasini, Journal of Synchrotron Radiation **13**, 321 (2006). 51, 52

[115] Z. Chao, W. Chun-Lei, L. Ji-Chao, and Y. Kun, Chinese Physical Society **16 (5)**, 1422 (2007). 53

[116] J. L. Gavartin, D. M. Ramo, A. L. Shluger, G. Bersuker, and B. H. Lee, Applied Physics Letters **89**, 082908 (2006). 60, 63

[117] S. A. Prosandeyev et al., Journal of Physics-Condensed Matter **8**, 6705 (1996). 61, 63

[118] R. A. Evarestov, A. V. Bandura, and V. E. Alexandrov, Physica Status Solidi B-Basic Solid State Physics **243**, 2756 (2006). 61, 63, 75, 76

[119] C. G. Van de Walle and J. Neugebauer, Journal of Applied Physics **95**, 3851 (2004). 64

[120] I. Denk, F. Noll, and J. Maier, Journal of the American Ceramic Society **80**, 279 (1997). 66

[121] R. Merkle and J. Maier, Physical Chemistry Chemical Physics **5**, 2297 (2003). 67

[122] M. T. Buscaglia, V. Buscaglia, M. Viviani, and P. Nanni, Journal of the American Ceramic Society **84**, 376 (2001). 68

[123] M. S. Islam, P. R. Slater, J. R. Tolchard, and T. Dinges, Dalton Transactions , 3061 (2004). 68

[124] H. Meštrić et al., Physical Review B **71**, 134109 (2005). 68

[125] H. Meštrić et al., Physical Review B **73**, 184105 (2006). 68

[126] J. W. Gibbs, *The Collected Works of J. Williard Gibbs*, New York: Longmans, 1928. 73

[127] G. L. Kellogg, Surface Science Reports **21**, 1 (1994). 74

[128] M. Mogensen, N. M. Sammes, and G. A. Tompsett, Solid State Ionics **129**, 63 (2000). 74

[129] N. Wilcox et al., Solid State Ionics **75**, 127 (1995). 74

[130] G. Horvath, J. Gerblinger, H. Meixner, and J. Giber, Sensors and Actuators B-Chemical **32**, 93 (1996). 74

[131] C. R. Stanek, M. R. Bradford, and R. W. Grimes, Journal of Physics-Condensed Matter **16**, S2699 (2004). 74

[132] J. R. Kitchin, J. K. Norskov, M. A. Barteau, and J. G. Chen, Journal of Chemical Physics **120**, 10240 (2004). 74

[133] V. Ravikumar, R. P. Rodrigues, and V. P. Dravid, Journal of the American Ceramic Society **80**, 1117 (1997). 74

[134] V. Ravikumar, R. P. Rodrigues, and V. P. Dravid, Journal of the American Ceramic Society **80**, 1131 (1997). 74

[135] W. Liu and C. A. Randall, Journal of the American Ceramic Society **91**, 3245 (2008). 74

[136] W. D. Kingery, Journal of the American Ceramic Society **57**, 74 (1974). 74

[137] M. F. Yan, R. M. Cannon, and H. K. Bowen, Journal of Applied Physics **54**, 764 (1983). 74

[138] K. Szot, W. Speier, J. Herion, and C. Freiburg, Applied Physics A-Materials Science & Processing **64**, 55 (1997). 77

[139] V. E. Henrich, G. Dresselhaus, and H. J. Zeiger, Physical Review B **17**, 4908 (1978). 77, 80

[140] S. Kimura, J. Yamauchi, M. Tsukada, and S. Watanabe, Physical Review B **51**, 11049 (1995). 77

[141] M. Q. Cai et al., Journal of Chemical Physics **124**, 174701 (2006). 77

[142] R. Astala and P. D. Bristowe, Journal of Physics-Condensed Matter **14**, 6455 (2002). 79

[143] S. Piskunov, Y. F. Zhukovskii, E. A. Kotomin, E. Heifets, and D. E. Ellis, Combinatorial Methods and Informatics in Materials Science **894**, 295 (2006). 80, 81, 83

[144] E. A. Kotomin, Y. A. Mastrikov, E. Heifets, and J. Maier, Physical Chemistry Chemical Physics **10**, 4644 (2008). 84, 85

[145] Y. Wang, D. Pillay, and G. S. Hwang, Physical Review B **70**, 193410 (2004). 84

[146] A. D. Yoffe, Advances in Physics **51**, 799 (2002). 87

[147] G. D. Scholes and G. Rumbles, Nature Materials **5**, 683 (2006). 87

[148] D. D. Fong et al., Science **304**, 1650 (2004). 87, 88

[149] B. Meyer and D. Vanderbilt, Physical Review B **63**, 205426 (2001). 88

[150] A. G. Zembilgotov, N. A. Pertsev, H. Kohlstedt, and R. Waser, Journal of Applied Physics **91**, 2247 (2002). 88

[151] C. J. Först, C. R. Ashman, K. Schwarz, and P. E. Blöchl, Nature **427**, 53 (2004). 88

[152] A. Brinkman et al., Nature Materials **6**, 493 (2007). 88

[153] K. P. Wang, Y. C. Ma, and K. Betzler, Physical Review B **76**, 144431 (2007). 88

[154] D. S. Kan et al., Nature Materials **4**, 816 (2005). 88

Vitaly Alexandrov, Curriculum Vitae

BIRTH DATE   15 June 1982

BIRTH PLACE   Inta, Russia

EDUCATION   Ph.D. student at the department of Prof. J. Maier (since 09.2006)
Max-Planck Institute for Solid State Research, Stuttgart

M.Sc., Quantum Chemistry (with honors)
St. Petersburg State University (06.2004 - 06.2006), adviser: Prof. R.A. Evarestov

Diploma, Physical Chemistry (with honors)
St. Petersburg State University (06.1999 - 06.2004), adviser: Prof. V.V. Malev

Inta Academical Gymnasium 1 (1996-1999), Inta
Inta School 9 (1989-1996), Inta

PUBLICATIONS

1. Alexandrov V.E., Kotomin E.A., Maier J., and Evarestov R.A., *The Journal of Chemical Physics* 129, 214704 (2008)

2. Alexandrov V.E., Evarestov R.A., Kotomin E.A., and Maier J., *Journal of Physics: Conference Series* 117, 012001 (1-6) (2008)

3. Alexandrov V.E., Maier J., Evarestov R.A., *Physical Review B* 77, 075111 (2008)

4. Evarestov R.A., Bandura A.V., Alexandrov V.E., *Surface Science* 601, 1844 (2007)

5. Evarestov R.A., Bandura A.V., Alexandrov V.E., *Physica Status Solidi (b)*, 243, 2756 (2006)

6. Evarestov R.A., Tupitsyn I.I., Bandura A.V., Alexandrov V.E., *International Journal of Quantum Chemistry*, 106, 2191 (2006)

7. Evarestov R.A., Bandura A.V., Alexandrov V.E., *Physics of the Solid State*, 47 (12), 2248 (2005)

8. Evarestov R.A., Bandura A.V., Alexandrov V.E., and Kotomin E.A., *Physica Status Solidi (b)*, 242 (2), R11-R13 (2005)